INDUCED TRANSPARENCY AND PULSE DELAY PLUS INDUCED ABSORPTION AND PULSE ADVANCEMENT USING THE ORTHOGONALLY POLARIZED WHISPERING GALLERY MODES OF A SINGLE MICRORESONATOR

By

KHOA VIET BUI

Bachelor of Science in Engineering Physics
Hanoi University of Science and Technology
Hanoi, Vietnam
2003

Submitted to the Faculty of the
Graduate College of the
Oklahoma State University
in partial fulfillment of
the requirements for
the Degree of
DOCTOR OF PHILOSOPHY
July, 2016

INDUCED TRANSPARENCY AND PULSE DELAY PLUS INDUCED ABSORPTION AND PULSE ADVANCEMENT USING THE ORTHOGONALLY POLARIZED WHISPERING GALLERY MODES OF A SINGLE MICRORESONATOR

Dissertation Approved:

Dr. Albert T. Rosenberger

Dissertation Adviser

Dr. Bruce J. Ackerson

Dr. Donna K. Bandy

Dr. Gil Summy

Dr. James West

ACKNOWLEDGEMENTS

Firstly, I would like to thank my family for their encouragement and support during the time I study here. Without any advice of my parents and help from my sister, I could not complete this dissertation easily.

Secondly, I want to express my gratefulness to my advisor Dr. Albert Thomas Rosenberger for his instruction since the time I started joining in his Optical Physics lab. His expert and whole-hearted guidance has led me to the right thing on the way to discover the scientific world.

Thirdly, I would like to thank many teachers in the Department of Physics, Oklahoma State University like Dr. Robert J. Hauenstein, Dr. James P. Wicksted, Dr. John W. Mintmire, Dr. Donna K. Bandy, and Dr. Jacques H H. Perk for their supports since the time I came to the US, and particularly thank to the office and technician personnel such as Susan, Danielle, Tamra, Sandra, Alisha, Mike Lucas, and Charles for their aids. Many of my TA and experimental work would have been finished longer if there was no help from them.

Finally, I would like to thank all my colleagues like Dr. Stoian, Erik Gonzales, Dr. Dale and Gregorio Martinez for their help, hard work and friendship. Many of the results in my dissertation come from their work before. With me, the time studying and working besides you is memorable and I will never forget in my whole life.

Name: KHOA VIET BUI

Date of Degree: JULY, 2016

Title of Study: INDUCED TRANSPARENCY AND PULSE DELAY PLUS INDUCED ABSORPTION AND PULSE ADVANCEMENT USING THE ORTHOGONALLY POLARIZED WHISPERING GALLERY MODES OF A SINGLE MICRORESONATOR

Major Field: PHOTONICS

Abstract:

In this dissertation, the major research is to produce induced transparency and pulse delay or induced absorption and pulse advancement using orthogonally polarized whispering gallery TE and TM modes of a single microresonator (either microsphere or hollow bottle resonator).

For background, we introduce the three-level atomic Λ system, interacting with a probe field and a much stronger coupling field, in which destructive interference between the direct and indirect absorption paths between the ground and excited levels of the system produces the induced transparency feature in the probe transmission (EIT). Autler-Townes splitting (ATS) of the transmitted power occurs when the coupling field is strong. Constructive interference caused by the transfer of coherence and transfer of population between the hyperfine sublevels of the ground and excited states of the system can produce an induced absorption feature (EIA). These EIT/ATS and EIA effects enable slow and fast light.

Next, we describe the coupled resonator induced transparency and absorption effects (CRIT, and CRIA). Due to the evanescent coupling between the coresonant whispering-gallery modes of the same polarization from two microspheres, the net throughput power in the coupled resonator system has features analogous to the EIT and EIA phenomena described previously.

Then, we introduce two new methods to produce the EIT/EIA-like features of throughput power. The first method relies on the intracavity coupling between two orthogonally polarized TE and TM modes of very different quality factor *Q* when one mode (either TE or TM) is driven, and the second method uses the superposition of the orthogonal throughputs (in the absence of intracavity cross polarization mode coupling) when the two modes are simultaneously driven. In both cases, the throughput has the same polarization as the input. We refer to the behavior observed using the first method as coupled mode induced transparency and absorption (CMIT, CMIA) and the behavior of the second method as coresonant polarization induced transparency and absorption (CPIT, CPIA). Some predictions of the scattering model of these processes are presented here. In addition, the experiment-fitting by using both scattering and rotational models for CMIT/ATS with pulse delay and CMIA with both pulse delay and pulse advancement when using with microsphere and hollow bottle resonator are presented.

TABLE OF CONTENTS

Chapter **Page**

Chapter **Page**

LIST OF TABLES

Table **Page**

LIST OF FIGURES

Figure **Page**

Figure **Page**

CHAPTER I

INTRODUCTION

Nowadays, development of telecommunication systems requires that information needs to flow faster with minimum loss. Especially, at the receiver where they have the $N \times N$ router [1], any of the input ports can be switched to any of the output ports. This can lead to collisions between data packets and the loss of information when they arrive simultaneously at the router. A solution to this problem is to build an optical buffer, which places one of these data packets on hold while the other clears the switch.

Slow light, slowed down information carrying light pulse, which has been investigated for many years, can resolve this problem. For example, if both pulses arrive at the same time or too close to each other, the router will only be able to accommodate one of them because of the switch time required to perform the operations. By activating the slow light medium in one of the branches, one of the pulses is delayed. As a result, no collision occurs and the flow of information is sped up. Furthermore, in an optical communication system, due to environmental effects and optical sources of noise, individual pulses might become displaced from the centers of their time windows. By using the slow light and fast light methods [1], this problem can be addressed easily.

In addition to the application for centering the pulses in their time windows, fast light (sped up information carrying light pulse) can be used to produce anomalous dispersion in a resonator based optical gyroscope. Anomalous dispersion increases the frequency separation between the resonant frequencies of the clockwise and counterclockwise propagating light when the gyroscope is rotating [2,3]. This effect leads to the enhancement of the sensitivity of rotation sensing.

Another aspect of slow light is the application in sensing based on the change of the shape of the induced transparency throughput power spectrum when the resonator is used as a sensor. By monitoring the shift of resonant wavelengths or measuring the change of light intensity from the output at a fixed wavelength [4,5] or monitoring the mode splitting separation of the throughput signal [6], the change in effective refractive index of the resonator mode is determined, and this allows us to calculate the concentration of the analyte attached to the surface of the sensor.

The variation of the throughput shape has not only applications in sensing, but it also has applications in optical switching. Based on the change of the transmission coefficient from high level to low level in a narrow frequency range, we can achieve the on/off contrast ratio in an optical system [7,8,9].

In this work, we introduce research topics developed in the Optical Physics Lab at Oklahoma State University, namely Induced Transparency and Pulse Delay plus Induced Absorption and Pulse Advancement with a single microresonator (either silica microsphere or silica hollow bottle resonator). These produce Electromagnetically Induced Transparency or Absorption (EIT or EIA) -like features of the throughput signal,

which enable slow or fast light (the delay or advancement of incident resonant pulses), by two new experimental processes.

The first process relies on the intracavity cross polarization coupling (CPC) between two orthogonally polarized whispering gallery modes (TE, TM) of a single microresonator when only one mode is driven at the input. We refer to behavior observed in the first method as coupled mode induced transparency and absorption (CMIT, CMIA) [10]. The second process uses the superposition of orthogonal throughputs (in the absence of intracavity cross polarization mode coupling) when two modes are simultaneously driven at the input and we refer to behavior observed in the second method as coresonant polarization induced transparency and absorption (CPIT, CPIA) [10].

The dissertation is distributed among six chapters. The second chapter introduces general concepts of EIT [11] and EIA [12], and discusses the coupling between two coresonant whispering gallery modes from two microspheres leading to coupled resonator induced transparency and absorption (CRIT and CRIA) [13,14]. An overview of the coupling and superposition between two orthogonally polarized whispering gallery TE and TM modes inside a single microresonator is also presented. The third chapter presents our computer model in which CPC is treated as a scattering process, and the throughput spectrum, dispersion, and the shape and position of the resonant throughput pulse relative to the input pulse can be calculated if the input parameters like quality factors *Q*, dip depths *M*, and coupling regimes of the working modes are known. Following Elijah Dale's discovery of cross polarization coupling [15], we develop the fourth chapter towards the production procedure for CMIT/CMIA plus pulse response

experiments based on the coupling between two coresonant orthogonally polarized TE and TM modes inside a single microsphere to produce the EIT or EIA-like feature of the throughput power. This chapter includes the creation and alignment of the Gaussian pulses, advantages of hollow bottle resonator over microsphere, the resonant pulse response of the resonator, and fitting the experimental data for throughput power and pulse response to computer model. The fifth chapter talks about the production procedure and fitting with computer model for CPIT/CPIA plus pulse response experiments based on the superposition between two coresonant orthogonally polarized TE and TM throughput modes when the input is linearly polarized at 45^{o} with respect to the TE-TM basis of the resonator, and the throughput has the same polarization as the input. The sixth chapter shows an experiment-fitting comparison between the scattering model and the rotational model, an alternate model in which CPC is treated as an intracavity polarization rotation process. The seventh chapter, also the final chapter of this dissertation, summarizes all of the findings and future development of this work.

CHAPTER II

INDUCED TRANSPARENCY AND INDUCED ABSORPTION

In this chapter, fundamental concepts of electromagnetically induced transparency [11], Autler-Townes splitting [16,17] and electromagnetically induced absorption [12] will be introduced. The development of EIT/EIA to coupled resonator induced transparency and absorption (CRIT/CRIA) by using two resonators is mentioned. The coupling and superposition between two orthogonally polarized whispering gallery modes of a single microresonator to produce the EIT/EIA-like features of the throughput power are also discussed.

II.1. Electromagnetically induced transparency and absorption

The idea of eliminating the absorption while making use of resonant nonlinearity has long been proposed and conducted both theoretically and experimentally. One way involves electromagnetically induced transparency (EIT), a phenomenon based on the coupling of two highly coherent optical fields such as lasers, which are tuned to interact with a three-level Λ quantum mechanical system such as an atom. The "probe" field of frequency ω_p is tuned near resonance between two of the states and measures the absorption spectrum of the transition. A much stronger "coupling" field of frequency ω_c is tuned near resonance at a different transition. As seen in the following Fig. 1, the probe field drives the transition between atomic states $|1\rangle$ and $|2\rangle$, and the coupling field drives the transition between atomic states $|2\rangle$ and $|3\rangle$. Ideally, the transition between atomic states $|3\rangle$ and $|1\rangle$ is dipole forbidden and the decay rate $\gamma_{31} = 0$.

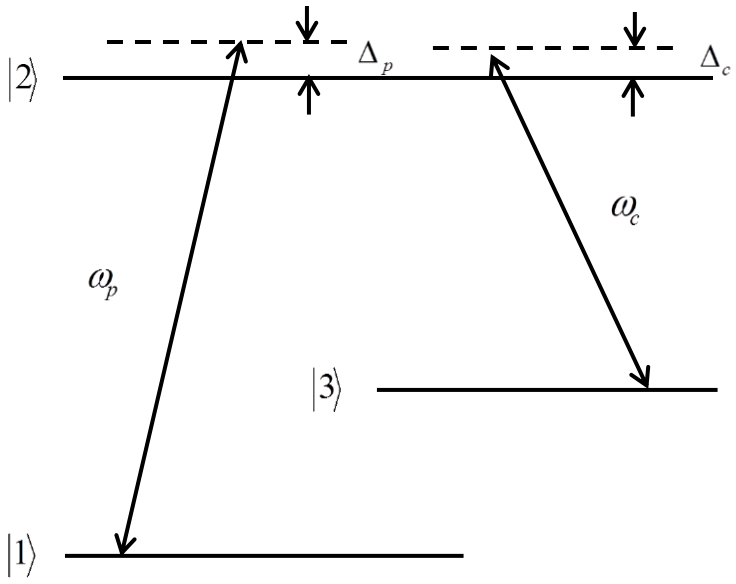

Figure 1. Three-level Λ system.

When the coupling field is turned off, with Rabi frequency $\Omega_c = \frac{\mu_{23} E_c}{\hbar} = 0$, where E_c is the amplitude of the coupling field and μ_{23} is the off-diagonal element of the dipole moment operator of the system, the probe absorption α has its maximum value when the probe frequency ω_p is equal to the transition frequency ω_{21} between atomic states $|1\rangle$ and $|2\rangle$ or probe detuning $\Delta_p = \omega_p - \omega_{21} = 0$. This corresponds to the black dashed curve shown in Fig. 2; the absorption linewidth is $2\gamma_{21}$. When the coupling field is turned on and still less than a threshold value ($\Omega_c \neq 0$ and $\Omega_c \leq \Omega_{th}$), on resonance ($\Delta_p = 0$), the destructive interference between two optical transition paths produces a reduction in the center of the probe absorption; this phenomenon is called EIT. When the coupling field is greater than the threshold value ($\Omega_c \geq \Omega_{th}$), mode splitting occurs and EIT gradually switches into Autler-Townes splitting (ATS). More details of this phenomenon will be discussed later in Chapter III. The splitting between the two

absorption peaks is directly proportional to the strength of the coupling field Ω_c. The decay rate γ_{31} between atomic states $|3\rangle$ and $|1\rangle$ plays an important role in determining the absorption coefficient α of the system; $\alpha(0)$ goes to zero as γ_{31} goes to zero. When $\Delta_c = \omega_c - \omega_{23} = 0$, where Δ_c is the coupling detuning, ω_c is the frequency of the coupling field, and ω_{23} is the transition frequency between atomic states $|2\rangle$ and $|3\rangle$, there is a transparency dip in the center of the absorption spectrum. This is manifested by the black solid curve of Fig. 2.

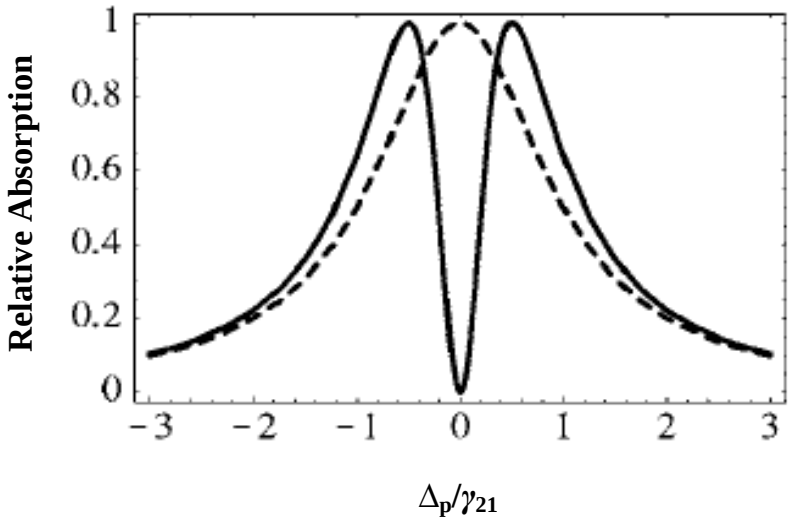

Figure 2. EIT spectrum [11].

This phenomenon can be explained as follows: when the interaction of the coupling field with the atom is weak, supermodes with the same resonant frequency but different linewidths are formed. The destructive interference between two optical transition paths cancels the probe absorption and the EIT feature of the throughput power is produced. When the interaction of the coupling field with the atom is large enough, the

superposition of atomic states $|2\rangle$ and $|3\rangle$ splits atomic state $|2\rangle$ into two dressed states $|+2\rangle$ and $|-2\rangle$. On resonance ($\Delta_p = 0$), the probe field E_p will see no upper atomic state to make the transition from the lower atomic level $|1\rangle$, therefore the atom will become transparent to the probe field and the supermodes are split into two modes with different frequencies but the same linewidth. This phenomenon is referred to as Autler-Townes splitting (ATS). Here, the energy difference between two dressed states $|+2\rangle$ and $|-2\rangle$ is proportional to the frequency separation between the supermodes.

Accompanying the variation of probe absorption coefficient is the rapid change of refractive index of the atomic medium with increasing frequency over a narrow spectral range. The steep positive slope of refractive index vs. frequency (normal dispersion) in the center of the transparency window gives rise to slow light [18]. It means that a light pulse with group velocity v_g (here $v_g = \frac{d\omega}{dk}$, $k = \frac{n(\omega)\omega}{c}$, ω is the angular frequency of the light pulse, $n(\omega)$ is the effective refractive index of the medium, c is the speed of light in vacuum), passing through the system, travels slower than the speed of light in the atomic medium ($v_g < \frac{c}{n(\omega)}$). This strong normal dispersion is seen near resonance in the solid black curve of Fig. 3. As in Fig. 2, the dashed curve shows the dispersion when the coupling field is off and the solid curve is the dispersion when the coupling field is on.

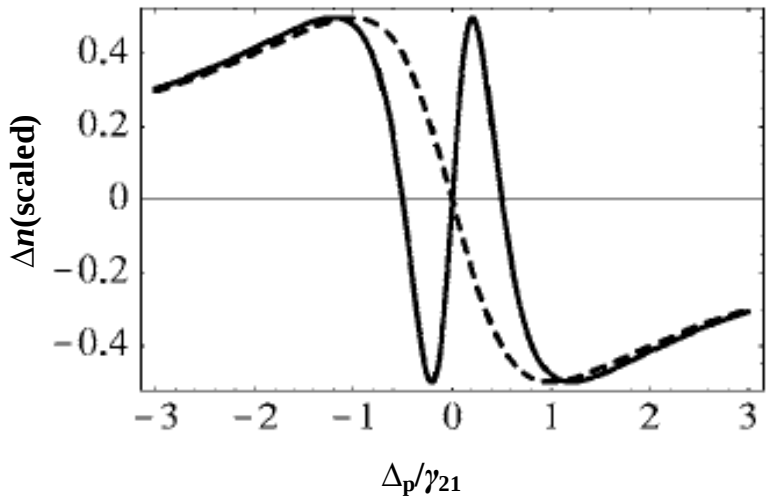

Figure 3. Positive dispersion slope [11].

In contrast to EIT, electromagnetically induced absorption (EIA) happens when there is an increase in the absorption coefficient due to the constructive interference between the transfer of population and transfer of coherence between two hyperfine ground and excited states of an atomic system, in which $F_g \rightarrow F_e = F_g + 1$ with $F_g > 0$ [12,19,20,21]. The difference in the absorption cross sections between two sublevels of the excited and ground hyperfine states results in the major difference in population between the ground and excited states, leading to an increase in the probe absorption on resonance [19,20,21,22]. This phenomenon is illustrated by the solid red curve of Fig. 4. This figure pertains to an analog metamaterial system, not to an actual atomic system.

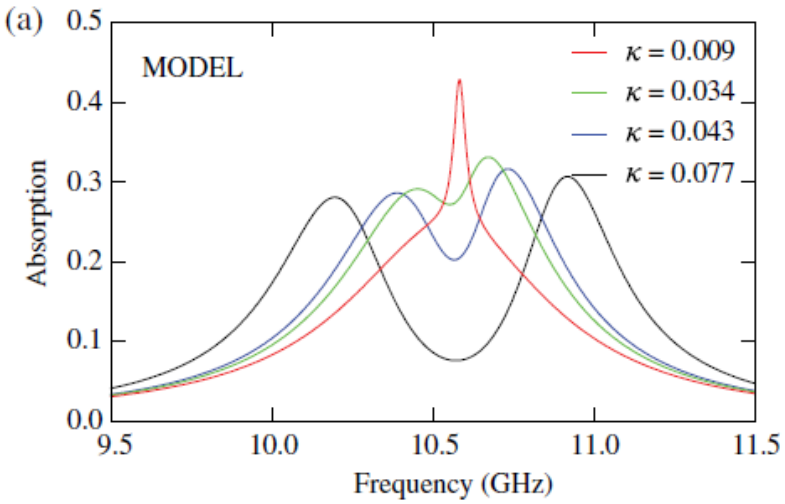

Figure 4. EIA spectrum [23]. κ is a normalized coupling strength.

In this case, the steep negative slope of refractive index vs. frequency (anomalous dispersion) on resonance gives rise to fast light [18], i.e. a light pulse with group velocity v_g passing through the system travels faster than the speed of light in the atomic medium ($v_g > \frac{c}{n(\omega)}$). This is seen in the solid blue curve of Fig. 5, which is for another analog system, where ϕ is the phase shift of the output relative to the input.

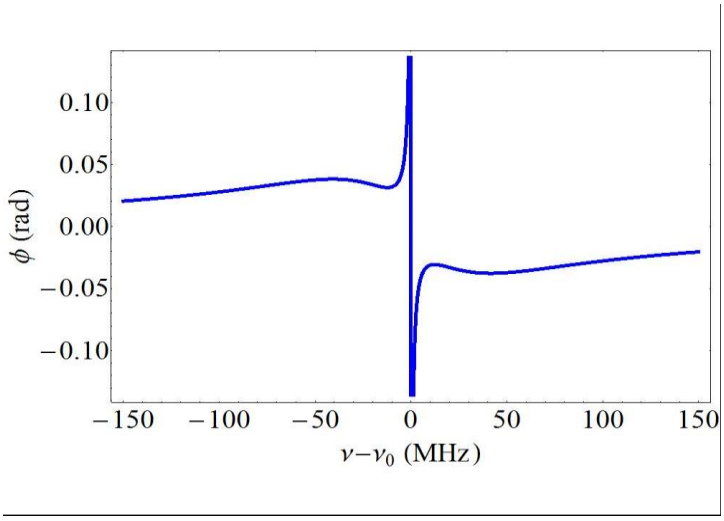

Figure 5. Negative dispersion slope.

II.2. Coupled resonator induced transparency and absorption

Induced transparency is not a quantum phenomenon, but something more universal; e.g., it can be observed in a system of two oscillators with equal natural frequencies but different damping rates that are coupled to each other [24]. Instead of fabricating multiple coupled photonic crystal cavities [25] or using parallel waveguides to indirectly connect the resonators [26,27], in our lab we studied coupled microresonators as a research tool for induced transparency and absorption by using two directly coupled microspheres.

Our resonator is made by melting the tip of an optical fiber with a hydrogen/oxygen mini torch. The surface tension of the molten glass pulls the fiber into a spherical ball whose diameter can be regulated to a sub-millimeter range, normally from 300 to 600 μm, thus it is termed microresonator. In order to work with the microresonator, light must be coupled into and out of the sphere with minimum

perturbation to the system. Our method is to use a single mode optical fiber, which is adiabatically tapered to a diameter on the order of a wavelength, usually something in the vicinity of 1550 nm. The tapered region exposes the evanescent portion of the fiber field. Bringing this fiber into contact with the microresonator in its equatorial plane allows us to couple the light into the microsphere and back out to the fiber through the tapered region and finally have the throughput light fall on a detector.

When the light is coupled into the microresonator, it is confined within the cavity and circulates around the circumference of the sphere by total internal reflection. When the effective optical path length is equal to an integral number of wavelengths, resonance is achieved. These resonances are called whispering gallery modes (WGMs). At each reflection, certain field components remain continuous across the boundary at which the radial propagation constant simultaneously goes imaginary, providing the resonator with an evanescent field. Scanning the laser in frequency exposes the modes of a resonator as Lorentzian dips in the detected throughput. The fractional dip depth M of a whispering gallery resonance can be expressed in terms of the loss ratio $x = \frac{T}{\alpha L}$ as $M = \frac{4x}{(1+x)^2}$, while the dip width (WGM linewidth $\Delta\nu$) is proportional to the total round-trip loss $T + \alpha L$. Here, T is the effective mirror transmittance describing the fiber coupling loss, and the microresonator intrinsic round-trip loss is given by αL, where α is the effective loss coefficient and L is the microresonator circumference. The dip depth reaches its maximum value $M = 1$ at critical coupling ($x = 1$), and $M < 1$ when the mode is either undercoupled ($x < 1$) or overcoupled ($x > 1$). The quality factor Q of a WGM is given by $Q = \frac{\nu}{\Delta\nu}$, where ν is the frequency of the incoming light.

An important feature of a microresonator is the occurrence of transverse electric (TE) and transverse magnetic (TM) mode families that result from the boundary conditions applied to the wave equation. Each mode has its own field configuration and they are polarized orthogonally to each other; TE modes are tangentially polarized while TM modes are radially polarized with respect to the resonator surface. For the microsphere, in the radial direction, higher order whispering gallery modes are distributed increasingly from the resonator surface toward the center of the sphere, and in the axial direction, higher order modes are distributed increasingly on both sides of the equator [28]. For the hollow bottle resonator, the mode distribution is almost the same as in the microsphere, except that in the radial direction the modes are confined by both external and internal surfaces of the wall, and in the axial direction [29] the mode profile is somewhat like the wave function of the simple harmonic oscillator. All the details of the whispering gallery mode distributions are given in Chapter IV.

In the coupled resonator experiment, two spheres are brought nearly into contact by using a precise actuator to control their separation. Due to the evanescent coupling between the coresonant whispering-gallery modes of the two microspheres, the net throughput power in the coupled resonator system has features analogous to the EIT and EIA phenomena described previously. This is accounted for by the destructive or constructive interference between the coresonant WGMs of the two microresonators, which either reduces or enhances light losses in the system, resulting in coupled resonator induced transparency (CRIT) or coupled resonator induced absorption (CRIA) effects. By controlling the separation *d* between the two microspheres as in Fig. 6, the intersphere evanescent coupling can be varied.

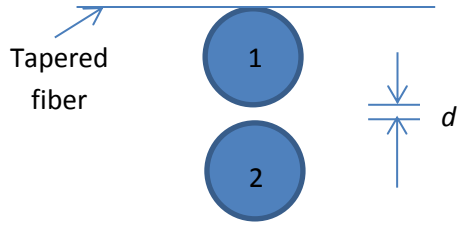

Figure 6. Coupled microspheres.

The intersphere evanescent coupling only occurs between two individual WGMs of the same polarization from two resonators. When the WGMs are coresonant, the CRIT splitting in the throughput will be frequency-symmetric about resonance, otherwise, what we will see is asymmetric. There are many combinations between the coupling regimes of two microspheres to produce the EIT or EIA-like throughput power. Here, I introduce only the case where the second resonator is undercoupled (the one farther from the coupling tapered fiber that has coupling loss less than the intrinsic loss). On resonance, the effective reflectivity of resonator 2 will be reduced. This reduction leads to a decrease in the outcoupled intracavity field of resonator 1, which is out of phase with the uncoupled part of the throughput. The net throughput of resonator 1 depends on its coupling regime with respect to the tapered fiber. If it is undercoupled, the net throughput power of the coupled resonator system will increase. What we will see is a narrow spike at the center of the resonant dip, thus it is called CRIT. If the first resonator is overcoupled and the second resonator is strongly undercoupled (coupling loss much less than the intrinsic loss), the reduction of the outcoupled intracavity field of resonator 1 will make the throughput power of the system decrease a little. What we will see is a narrow dip at the center of the resonant dip, thus it is called CRIA. However, if the first resonator is overcoupled and the second resonator is weakly undercoupled (near

critical coupling), the throughput power of the system is quite different. When the outcoupled intracavity field gets reduced, we still have CRIA. But, when it is reduced below a critical value, what we will see is CRIT instead.

II.3. Induced transparency and absorption in a single microresonator

It has been shown that the EIT- like feature of the throughput power which was thought to require coupled resonators now can be done with a single microresonator as in Fig 7. The destructive interference between two whispering gallery modes inside a microresonator (microsphere or microtoroid) can be done by using the temperature tuning [30], controlling the fiber-cavity coupling strength and the polarization of incident light [31,32], using the integrated microdisk resonator coupled with two buses [33], or relying on the intermodal coupling between counterpropagating modes (clockwise and counterclockwise) [34]. For a single microbubble, the coupling between two whispering gallery modes of the same polarization but with different radial orders is performed by using the precise pressure tuning method [35]. Recently, a new method, namely modal coupling between different types of modes (TE and TM) inside a ring resonator, has been tried in order to produce the mode splitting of the throughput signal [36].

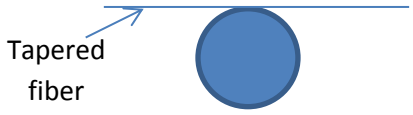

Figure 7. Single microresonator (microsphere or hollow bottle resonator).

Our new method is based on the cross polarization coupling (CPC) effect between coresonant TE and TM modes inside a whispering gallery microresonator to produce the induced transparency feature of the throughput power. When one mode (either TE or TM) is driven at the input of a microresonator system, in addition to the throughput signal of the same polarization, a significant throughput power can be found in the orthogonal polarization [15]. The two throughput polarizations TE and TM are separated by a polarizing beam splitter (PBS) and they go to two detectors 1 and 2 as in Fig. 8; the detail of this procedure is given in Chapter IV.

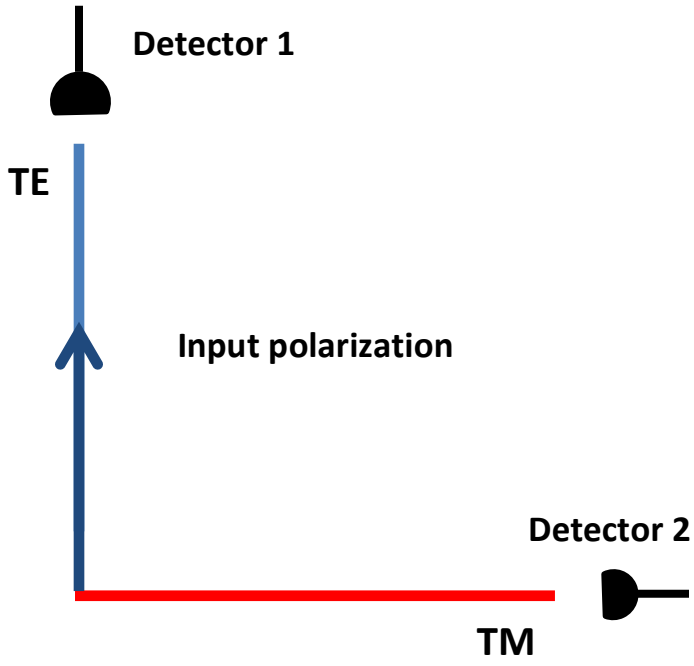

Figure 8. CMIT diagram when TE mode is driven at the input (blue).

In Fig. 8, the microresonator basis is given with TE axis (vertical light blue) and TM axis (horizontal red). When a TE mode (dark blue arrow) is driven, in addition to the TE throughput captured by detector 1, a significant power of the orthogonally polarized

TM mode can be found in detector 2. Examples of experimental throughput traces due to the cross polarization coupling effect are given in Fig. 9 for TE (blue) and TM (yellow).

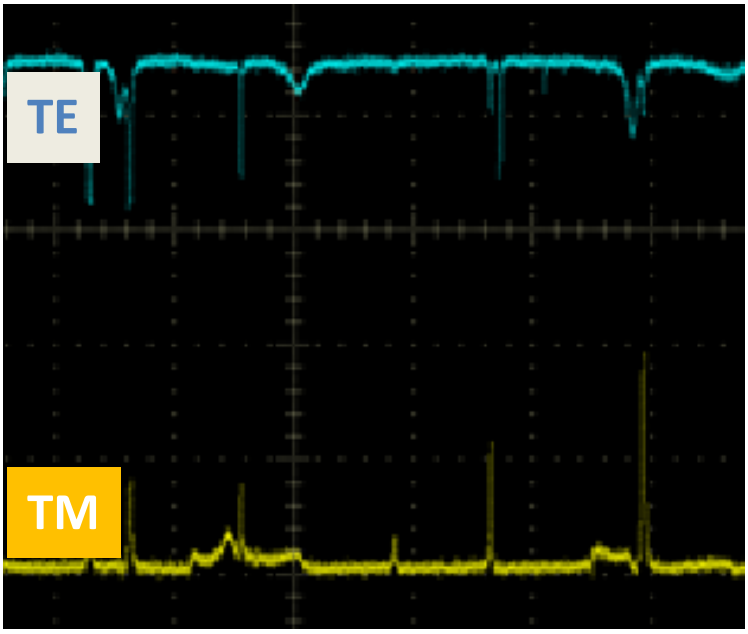

Figure 9. Cross polarization coupling throughput with TE input: TE throughput (blue) and TM throughput (yellow).

The coresonance between TE and TM modes can be obtained coincidentally or by strain tuning the microresonator by means of using a piezoelectric transducer (PZT) [37]. Strain tunes TE and TM modes at different rates and can bring two orthogonal TE and TM modes into frequency coresonance and this has been shown to be a prerequisite for CPC to be observed [38]. If the two modes are not degenerate in frequency, power in the orthogonal mode cannot build up in the cavity and the cross-coupled orthogonal polarization is too weak to observe.

When circulating within the microresonator under total internal reflection, the condition in which one mode can be cross-coupled from the other orthogonally polarized mode is probably polarization rotation due to asymmetry of the resonator about the equator, but because it is a relatively weak effect, it can be modeled as a cross polarization scattering at one point on the circumference.

When the quality factors of two modes are very different and the cross-coupling probability T_s (the probability per round trip that polarization of a circulating photon will flip to the orthogonal state) is smaller than the critical value $T_{critical}$, destructive interference between the direct and indirect excitation paths of TE modes produces the induced transparency feature in the throughput power. This behavior is referred to as coupled-mode induced transparency (CMIT). When the cross-coupling probability T_s is greater than the critical value $T_{critical}$, mode splitting occurs [39]. This behavior is referred to as Autler-Townes splitting (ATS), and the frequency splitting is proportional to the coupling strength [16]. This phenomenon is analogous to classical coupled oscillators or level splitting in the quantum double square well. In the limit of large splitting, the split modes of lower and higher frequencies are symmetric and antisymmetric (respectively) combinations of TE and TM. All the theoretical and experimental procedures will be discussed in more detail in Chapters III and IV.

Figure 10 exhibits the EIT/ATS-like feature of the throughput signal due to mode splitting for the case of TE input. The TE throughput is split (blue trace); the TM detector in this experiment is turned off (yellow trace). The selected WGM has the laser

scanning in the direction of decreasing frequency from left to right, and it is also possible to observe coupled-mode induced absorption (CMIA).

From Fig. 10 we can easily realize that the blue trace of throughput signal looks like the inverted EIT. This can be explained as follows: the throughput of the propagating light is the complement of the net power loss profile of the material. When this net loss is reduced to zero, the throughput will reach its maximum value.

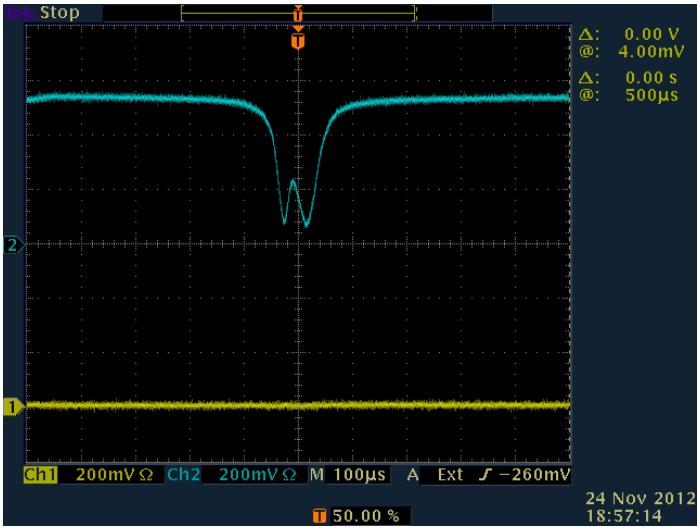

Figure 10. CMIT: EIT/ATS-like feature due to mode splitting induced by CPC. Blue upper trace: TE; yellow lower trace: TM.

Recently, our group has tried a new method for producing the EIT-like feature of the throughput power, in which instead of exciting only one mode family as in the case of CMIT/CMIA, the two orthogonal coresonant polarizations are simultaneously driven by having the input light linearly polarized at an angle of 45^{o} with respect to the TE – TM basis of the microresonator [10]. The input and observed throughput have the same polarization and are the superposition of two orthogonal components (TE and TM

polarizations). This superposition of two coresonant TE and TM modes is not created by mode coupling, but nevertheless produces effects which can be referred to as coresonant polarization induced transparency and absorption (CPIT, CPIA). These effects lead to slow light and fast light respectively. For this kind of experiment, mode coupling between TE and TM is not needed and the CPC phenomenon can be eliminated.

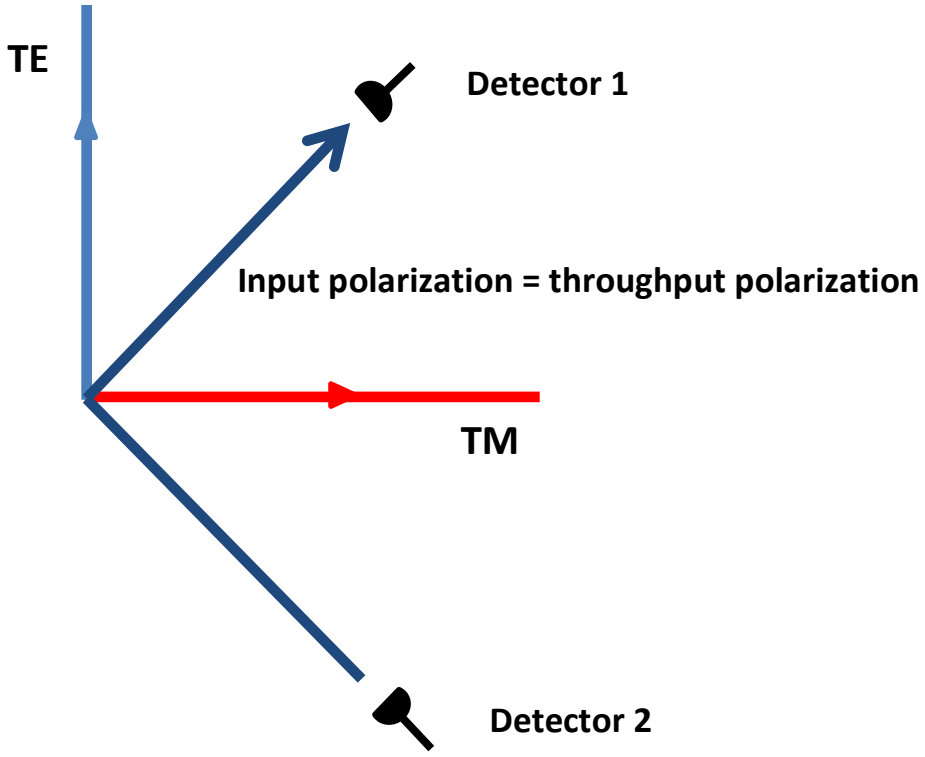

Figure 11. CPIT diagram when both TE mode (blue) and TM mode (red) are driven at the input.

In Fig. 11, the microresonator basis is given with TE axis (vertical light blue) and TM axis (horizontal red). When input light (dark blue arrow) is driven at an angle of 45^{o} with respect to the resonator basis, both TE (blue) and TM (red) are driven equally

simultaneously at the input of a microresonator system. The throughput polarization analyzer including the polarizing beam splitter (not shown) and two detectors 1 and 2 is rotated 45^{o} with respect to the microresonator's TE-TM basis. The parallel detector 1 detects the symmetric superposition of the throughput TE and TM modes, and the perpendicular detector 2 detects the antisymmetric superposition of TE and TM.

CHAPTER III

MODEL

In this chapter, we use the numerical model written in Mathematica to simulate the CMIT/CMIA and ATS features of the throughput power spectrum for coupled mode experiments and the CPIT/CPIA features of the throughput power spectrum for coresonant polarization experiments. Also, the dispersion, namely the frequency dependence of the relative phase of the throughput signal with respect to the input signal is calculated. Moreover, the throughput response of the resonator with respect to an incident resonant Gaussian pulse is also included.

III.1. Introduction to CMIT model

A ring-cavity model has been developed for simulating the CMIT/CMIA, ATS and CPIT/CPIA effects. The input field of any polarization (of unit amplitude, for convenience) is represented by two orthogonal components E_{f1} and E_{f2} with input polarization angle θ from the TE axis and arbitrary relative phase φ between components correspondingly:

$$E_{f1} = \cos\theta, \tag{1}$$

$$E_{f2} = e^{i\varphi} \sin\theta. \tag{2}$$

For simplification, in the ring-cavity diagram of Fig. 12, the input and throughput field polarization bases are assumed to be lined up perfectly with the resonator's TE – TM basis. With $\varphi = 0$ for linear input polarization, if we turn E_{f1} on and E_{f2} off by setting $\theta = 0^o$, only the TE mode is driven at the input. The cross polarization coupling becomes evident when a significant amount of TM mode is produced at the output when only the TE mode is driven at the input, and vice versa. Since the actual TE and TM modes inside the microresonator that are being simulated have different spatial profiles in general, each mode is given its own reflection and transmission coefficients at the input/output mirror. The reflection coefficients r_1 and r_2 are chosen to have real values whereas the transmission coefficients it_1 and it_2 are imaginary for energy conservation conditions ($r_j^2 + t_j^2 = 1$, j = 1, 2, *s*, etc.). Similarly, at the cross polarization coupler (CPC), the cross coupling amplitude for scattering into the mode of orthogonal polarization is it_s and the non-scattering amplitude is r_s. The effective intrinsic loss

coefficients of the TE and TM modes are α_1 and α_2, and L is the round-trip cavity length; δ_1 and δ_2 are the TE and TM round-trip phases (modulo 2π), proportional to the detunings of the input light from the TE and TM resonances, respectively.

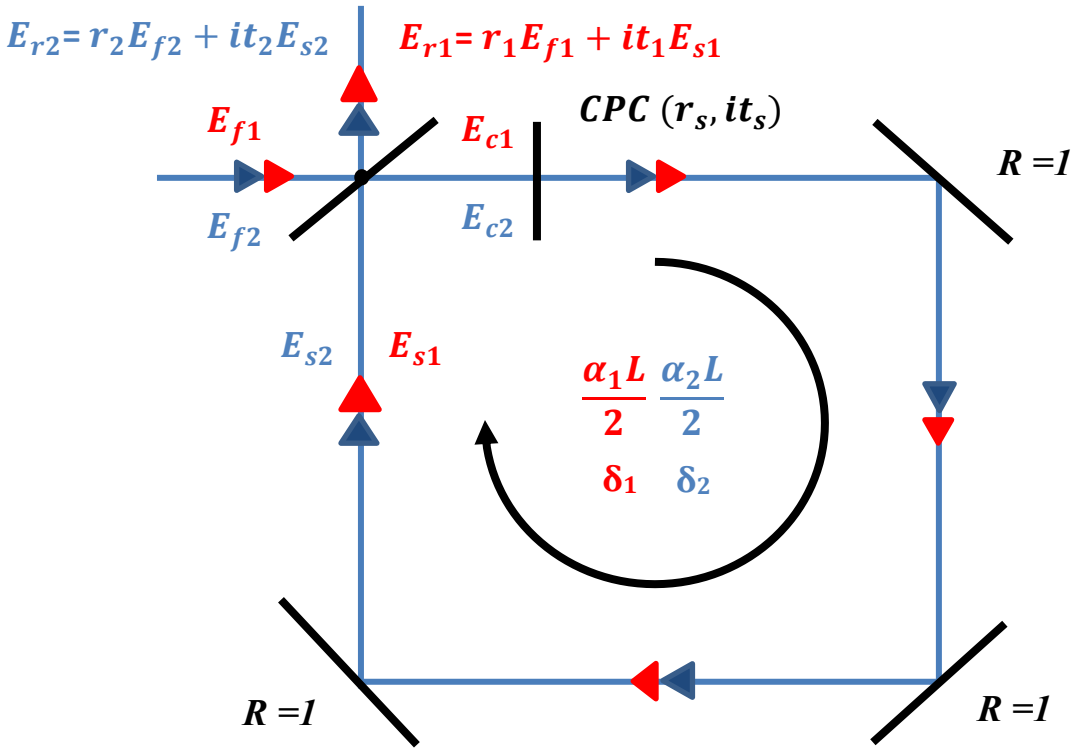

Figure 12. Ring cavity model. Red: mode 1; blue: mode 2.

Let's examine the ring-cavity model in full generality, with the input TE and TM components given by Eqs. (1) and (2), respectively. The fields just before the CPC are:

$$E_{c1} = it_1E_{f1} + r_1E_{s1}, \tag{3}$$

$$E_{c2} = it_2E_{f2} + r_2E_{s2}, \tag{4}$$

where E_{s1} and E_{s2} are the intracavity fields just before the input/output coupler; in the scattering model, they are calculated according to the two below equations:

$$E_{s1} = \exp\{-\frac{\alpha_1 L}{2} + i\delta_1\}(r_s E_{c1} + it_s E_{c2}), \tag{5}$$

$$E_{s2} = \exp\{-\frac{\alpha_2 L}{2} + i\delta_2\}(r_s E_{c2} + it_s E_{c1}), \tag{6}$$

After a simple analysis based on Fig. 12, we end up with the intracavity TE and TM fields:

$$E_{s1} = \frac{1}{D}[it_1 \exp\{-\frac{\alpha_1 L}{2} + i\delta_1\}(r_s - r_2 \exp\{-\frac{\alpha_2 L}{2} + i\delta_2\})E_{f1} \tag{7}$$
$$- t_2 t_s \exp\{-\frac{\alpha_1}{2} L + i\delta_1\}E_{f2}],$$

$$E_{s2} = \frac{1}{D}[it_2 \exp\{-\frac{\alpha_2 L}{2} + i\delta_2\}(r_s - r_1 \exp\{-\frac{\alpha_1 L}{2} + i\delta_1\})E_{f2} \tag{8}$$
$$- t_1 t_s \exp\{-\frac{\alpha_2}{2} L + i\delta_2\}E_{f1}].$$

Where

$$D = 1 - r_1 r_s \exp\{-\frac{\alpha_1 L}{2} + i\delta_1\} - r_2 r_s \exp\{-\frac{\alpha_2 L}{2} + i\delta_2\} \tag{9}$$
$$+ r_1 r_2 \exp\{-\frac{\alpha_1 + \alpha_2}{2} L + i(\delta_1 + \delta_2)\}.$$

In the rotational model, as the polarization rotates clockwise in the TE-TM basis, it_s in Eq. (6) is replaced by t_s, and it_s in Eq. (5) is replaced by $-t_s$. The full detail of this second model is shown in Chapter VI; the scattering model will be used throughout the present chapter.

The throughput TE and TM fields are given by

$$E_{r1} = r_1 E_{f1} + it_1 E_{s1}, \tag{10}$$

$$E_{r2} = r_2 E_{f2} + it_2 E_{s2}, \tag{11}$$

and if the throughput detection analyzer basis makes an angle ψ with the TE – TM basis, the detected field components are

$$E_{a1} = E_{r1}\cos\psi + E_{r2}\sin\psi, \tag{12}$$

$$E_{a2} = -E_{r1}\sin\psi + E_{r2}\cos\psi. \tag{13}$$

For modeling the CMIT/CMIA experiment, for example, both θ and ψ are set to be equal to 0^o. In general, for all experimental conditions described in this dissertation, the square moduli of E_{a1} and E_{a2} are proportional to the throughput powers and they can be used to compare with the experimental results. The model throughput powers are plotted as a function of input frequency relative to the resonant frequency of the TE mode, so that the physical parameters of the system such as quality factors, dip depths, and coupling regimes can be input and the cross coupling probability and offset of the TM mode from the TE mode can be adjusted to fit the experimental data. For the Gaussian pulse response to be detailed later, the experimental pulse width is input and the pulse center frequency detuning (from mode 1) is adjusted to agree with the experiment. The fitting of experimental results thus involves one free parameter (the CPC probability) and two semi-free parameters (the frequency offset of mode 2 from mode 1 and the pulse detuning).

III.2. CMIT and ATS

One important parameter that can be used to determine whether the system is in the CMIT or the ATS regime is the cross coupling probability T_s ($=t_s^{\,2}$). When T_s is less than a critical value $T_{critical}$, we have the CMIT throughput spectrum and in contrast, when T_s is greater than the critical value $T_{critical}$, what we see is ATS. The derivation for the critical condition can be taken as follows.

If we set:

$$e_1 = \exp\{-\frac{\alpha_1 L}{2} + i\delta_1\},$$

$$e_2 = \exp\{-\frac{\alpha_2 L}{2} + i\delta_2\}.$$

If e_1 and e_2 represent a roundtrip with round trip time $\tau_{rtj} = \frac{n_j L}{c}$, where n_j is the effective index of refraction of mode *j*, E_{sj} at a time *t* is given in terms of E'_{c1} and E'_{c2} (where the prime means at $t - \tau_{rtj}$) as follows:

$$E_{s1} = e_1(r_s E'_{c1} + it_s E'_{c2}), \tag{14}$$

$$E_{s2} = e_2(r_s E'_{c2} + it_s E'_{c1}), \tag{15}$$

where E'_{c1} and E'_{c2} are given by:

$$E'_{c1} = it_1 E'_{f1} + r_1 E'_{s1}, \tag{16}$$

$$E'_{c2} = it_2 E'_{f2} + r_2 E'_{s2}. \tag{17}$$

Thus, E_{s1} and E_{s2} can be rewritten as:

$$E_{s1} = a_1 E'_{f1} + b_1 E'_{f2} + c_1 E'_{s1} + d_1 E'_{s2}, \tag{18}$$

$$E_{s2} = a_2 E'_{f2} + b_2 E'_{f1} + c_2 E'_{s2} + d_2 E'_{s1}. \tag{19}$$

Where: $a_1 = it_1 r_s e_1$, $b_1 = -t_2 t_s e_1$, $c_1 = r_1 r_s e_1$, $d_1 = ir_2 t_s e_1$, $a_2 = it_2 r_s e_2$, $b_2 = -t_1 t_s e_2$, $c_2 = r_2 r_s e_2$, $d_2 = ir_1 t_s e_2$.

To get differential equations describing the time evolution of the intracavity fields, we assume that changes in a round trip are small, so that $\dot{E}_{sj} = \dfrac{E_{sj} - E'_{sj}}{\tau_{rtj}}$ and the primes can be dropped on the right hand side of the equations below:

$$E_{s1} - E'_{s1} = (c_1 - 1)E_{s1} + d_1 E_{s2} + a_1 E_{f1} + b_1 E_{f2}, \tag{20}$$

$$E_{s2} - E'_{s2} = (c_2 - 1)E_{s2} + d_2 E_{s1} + a_2 E_{f2} + b_2 E_{f1}. \tag{21}$$

The differential equations for E_{s1} and E_{s2} are thus:

$$\dot{E}_{s1} = -\frac{1-c_1}{\tau_{rt1}} E_{s1} + \frac{d_1}{\tau_{rt1}} E_{s2} + \frac{a_1}{\tau_{rt1}} E_{f1} + \frac{b_1}{\tau_{rt1}} E_{f2}, \tag{22}$$

$$\dot{E}_{s2} = -\frac{1-c_2}{\tau_{rt2}} E_{s2} + \frac{d_2}{\tau_{rt2}} E_{s1} + \frac{a_2}{\tau_{rt2}} E_{f2} + \frac{b_2}{\tau_{rt2}} E_{f1}. \tag{23}$$

Where, $\dfrac{1-c_j}{\tau_{rtj}} = \dfrac{1-r_j e_j r_s}{\tau_{rtj}} = \dfrac{T_j + \alpha_j L}{2\tau_{rtj}} - i\dfrac{\delta_j}{\tau_{rtj}} + \dfrac{T_s}{2\tau_{rtj}} = \kappa_j(1 + i\theta_j) + \dfrac{T_s}{2\tau_{rtj}} \equiv \gamma_j$.

$T_j = \left|it_j\right|^2$ is the coupling loss,

$\kappa_j = \dfrac{T_j + \alpha_j L}{2\tau_{rtj}} = \dfrac{1}{2\tau_j}$ is the field decay rate of mode *j*,

τ_j is the photon lifetime of mode *j*,

$\theta_j = \dfrac{\nu - \nu_o}{\Delta\nu/2}$ is the cavity detuning of the input field from resonance in units of half of the WGM linewidth $\Delta\nu$,

γ_j is the total loss rate for the intracavity field E_{sj}.

For the last three terms in these two above differential equations; r_j, r_s, and e_j can be replaced by 1 since they are approximately equal to $1-\varepsilon$, with $\varepsilon \approx 10^{-4}$. So we get:

$$\dot{E}_{s1} = -\gamma_1 E_{s1} + \frac{it_s}{\tau_{rt1}} E_{s2} + \frac{it_1}{\tau_{rt1}} E_{f1} - \frac{t_2 t_s}{\tau_{rt1}} E_{f2}, \tag{24}$$

$$\dot{E}_{s2} = -\gamma_2 E_{s2} + \frac{it_s}{\tau_{rt2}} E_{s1} + \frac{it_2}{\tau_{rt2}} E_{f2} - \frac{t_1 t_s}{\tau_{rt2}} E_{f1}. \tag{25}$$

From Eqs. (10) and (11), we have the first order differential equations for the throughput fields:

$$\dot{E}_{r1} = \dot{E}_{f1} - \gamma_1 (E_{r1} - r_1 E_{f1}) + \frac{it_s t_1}{t_2 \tau_{rt1}} (E_{r2} - r_2 E_{f2}) - \frac{t_1^2}{\tau_{rt1}} E_{f1} - \frac{it_1 t_2 t_s}{\tau_{rt1}} E_{f2}, \tag{26}$$

$$\dot{E}_{r2} = \dot{E}_{f2} - \gamma_2 (E_{r2} - r_2 E_{f2}) + \frac{it_s t_2}{t_1 \tau_{rt2}} (E_{r1} - r_1 E_{f1}) - \frac{t_2^2}{\tau_{rt2}} E_{f2} - \frac{it_1 t_2 t_s}{\tau_{rt2}} E_{f1}. \tag{27}$$

For constant E_{fj}, $\ddot{E}_{rj} = it_j \ddot{E}_{sj}$, so from Eq. (24) we have:

$$\ddot{E}_{s1} = -\gamma_1 \dot{E}_{s1} + \frac{it_s}{\tau_{rt1}} \dot{E}_{s2}. \tag{28}$$

From Eqs. (24) and (25), we have:

$$\ddot{E}_{s1} = -\gamma_1 \dot{E}_{s1} + \frac{it_s}{\tau_{rt1}} \left\{ -\gamma_2 E_{s2} + \frac{it_s}{\tau_{rt2}} E_{s1} + \frac{it_2}{\tau_{rt2}} E_{f2} - \frac{t_1 t_s}{\tau_{rt2}} E_{f1} \right\}. \tag{29}$$

So,

$$\ddot{E}_{s1} = -\gamma_1 \dot{E}_{s1} + \frac{it_s}{\tau_{rt1}} \left\{ \begin{array}{l} -\gamma_2 \dfrac{\left(\dot{E}_{s1} + \gamma_1 E_{s1} - \dfrac{it_1}{\tau_{rt1}} E_{f1} + \dfrac{t_2 t_s}{\tau_{rt1}} E_{f2} \right)}{\dfrac{it_s}{\tau_{rt1}}} \\ + \dfrac{it_s}{\tau_{rt2}} E_{s1} + \dfrac{it_2}{\tau_{rt2}} E_{f2} - \dfrac{t_1 t_s}{\tau_{rt2}} E_{f1} \end{array} \right\}. \tag{30}$$

Or,

$$\begin{aligned} \ddot{E}_{s1} = &-(\gamma_1 + \gamma_2)\dot{E}_{s1} - \left(\frac{T_s}{\tau_{rt1}\tau_{rt2}} + \gamma_1 \gamma_2 \right) E_{s1} + \left(\frac{it_1 \gamma_2}{\tau_{rt1}} - \frac{it_1 T_s}{\tau_{rt1}\tau_{rt2}} \right) E_{f1} \\ &- \left(\frac{t_2 t_s}{\tau_{rt1}\tau_{rt2}} + \frac{\gamma_2 t_2 t_s}{\tau_{rt2}} \right) E_{f2}. \end{aligned} \tag{31}$$

Finally, neglecting the small factors multiplying the input fields, we have:

$$\ddot{E}_{s1} + (\gamma_1 + \gamma_2)\dot{E}_{s1} + \left(\frac{T_s}{\tau_{rt1}\tau_{rt2}} + \gamma_1 \gamma_2 \right) E_{s1} = \frac{it_1 \gamma_2}{\tau_{rt1}} E_{f1} - \frac{t_2 t_s}{\tau_{rt1}\tau_{rt2}} E_{f2}. \tag{32}$$

This equation has the form of a driven damped oscillator; with $E_{s1} \propto e^{\lambda t}$ and $E_{f1} = E_{f2} = 0$, we have:

$$\lambda^2 + (\gamma_1 + \gamma_2)\lambda + \left(\gamma_1\gamma_2 + \frac{T_s}{\tau_{rt1}\tau_{rt2}}\right) = 0. \tag{33}$$

This characteristic equation has the roots:

$$\lambda_{1,2} = -\frac{\gamma_1 + \gamma_2}{2} \pm \sqrt{\left(\frac{\gamma_1 + \gamma_2}{2}\right)^2 - \gamma_1\gamma_2 - \frac{T_s}{\tau_{rt1}\tau_{rt2}}}. \tag{34}$$

Or,

$$\lambda_{1,2} = -\frac{\gamma_1 + \gamma_2}{2} \pm \sqrt{\left(\frac{\gamma_1 - \gamma_2}{2}\right)^2 - \frac{T_s}{\tau_{rt1}\tau_{rt2}}}. \tag{35}$$

On resonance, we have $\gamma_j \approx \frac{T_j + \alpha_j L}{2\tau_{rtj}} = \frac{\Delta\delta_j}{2\tau_{rtj}}$, where $\Delta\delta_j$ is the linewidth in phase of the WGM of mode *j*. If $\tau_{rt1} \approx \tau_{rt2}$, the radicand of Eq. (35) can be rewritten as:

$$\left(\frac{\gamma_1 - \gamma_2}{2}\right)^2 - \frac{T_s}{\tau_{rt1}\tau_{rt2}} = \left(\frac{\Delta\delta_1 - \Delta\delta_2}{4\tau_{rt}}\right)^2 - \frac{T_s}{\tau_{rt}^2}.$$

When $T_s < \left(\frac{\Delta\delta_1 - \Delta\delta_2}{4}\right)^2 = T_{critical}$, the radicand is positive, and Eq. (35) has two real values for λ_1 and λ_2. The destructive interference between the direct and indirect excitation paths of the intracavity TE mode produces the induced transparency (CMIT) feature of the throughput power. In contrast, when $T_s > T_{critical}$, the radicand is negative,

and Eq. (35) has two complex values for λ_1 and λ_2. The throughput now is split on both sides from the center of the feature due to the coupling between the intracavity TE and TM modes, and this phenomenon is referred to as ATS.

Another feature of our model is to calculate the response of the resonator to an input field of the same specified polarization, but in the form of a Gaussian pulse whose field envelope is given by: $G[\Delta t_o, t] = e^{-2(\ln[2])(\frac{t}{\Delta t_o})^2}$, where Δt_o is the pulse width or full width at half maximum (FWHM) of the intensity envelope, when the Gaussian envelope is imposed on the input field amplitude. The set of coupled differential equations, Eqs. (26) and (27), can then be solved to find the pulse response. Since we want the entire bandwidth of the pulse to experience the same steep dispersion for delay or advancement without distortion, and the frequency range of the strongly dispersive region is approximately equal to the linewidth of the higher-*Q* WGM, the input pulse width is chosen to be at least $\Delta t_o = \frac{0.441}{\Delta \nu_{\min}}$, so that the pulse bandwidth is equal to or less than the linewidth $\Delta \nu_{\min}$ of the higher-*Q* mode (TE or TM). The center frequency of the pulse can also be tuned away from the frequency of the lower-*Q* WGM in order to better coincide with the induced transparency/absorption feature in the throughput spectrum.

III.3. Relationship between CMIT and slow light

Some typical results of the model are presented here. In all cases, the parameter values chosen are experimentally realistic. Among all of the results reported here, TE and TM modes are assumed to be coresonant, $Q_1 << Q_2$, the wavelength is taken to be 1550 nm, and the resonator radius is assumed to be 300 μm. The cross polarization

coupling probability $T_s\,(=t_s{}^2)$ is calculated to be 5×10^{-8}, which can be considered the condition of strong cross polarization coupling between TE and TM modes. In the following three figures, the input light is linearly polarized at 0^o, the detected throughput light has the same polarization as the input, Q_1 = 5×10^6, Q_2 = 1×10^8, M_1 = 0.8, M_2 = 0.7, T_s = 5×10^{-8}, both modes are undercoupled, the offset $\nu_2-\nu_1$ = 0, and the pulse width is set to 230 ns, which makes its bandwidth equal to the full width at half maximum (FWHM) of the (higher-*Q*) TM mode. Figure 13 is the throughput spectrum of the input polarization component. Since $T_s < T_{critical}$, the throughput has the CMIT feature. Fig. 14 is the dispersion, i.e., the relative phase shift of the throughput with respect to the input, and Fig. 15 shows the input pulse and the throughput pulse. Both pulses are actually throughput pulses; the "input" is the throughput pulse when the center frequency of the input is far off resonance, and the "throughput" is the throughput pulse when the center frequency of the input is on resonance.

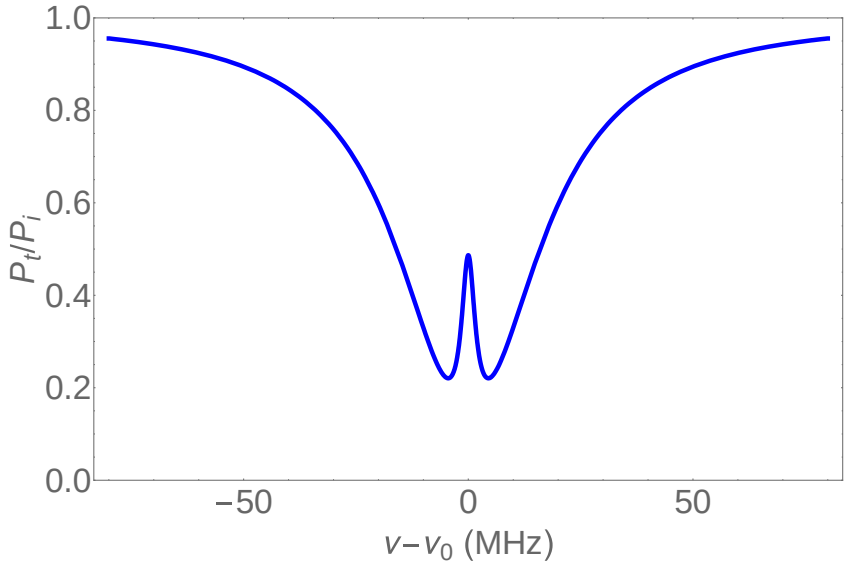

Figure 13. Modeled CMIT throughput spectrum.

From Fig. 13, we realize that the width of the transparency feature $\Delta\delta_{IT} = \frac{4T_s}{T_1 + \alpha_1 L}$ [40] is somewhat greater than the width of mode 2 in this case. Group delay, the delay experienced by a resonant pulse with sufficiently narrow bandwidth, can be calculated based on the dispersion slope of Fig. 14 as follows: $\tau_d = \frac{d\phi}{2\pi d\nu}$, where τ_d is the group delay, and $\frac{d\phi}{d\nu}$ is the rate of change of the relative phase of the throughput with respect to the input frequency, evaluated on resonance. After converting frequency ν into round trip phase δ according to the formula $\Delta\delta = \frac{4\pi^2 na}{c}\Delta\nu$ (where a is the microresonator radius, n is the effective index; when the difference in refractive indices of two modes is small, we take them to have the same effective n), the group delay evaluated on resonance for the case in which both WGMs are strongly overcoupled is determined according to the formula below [40]:

$$\left.\frac{d\phi}{d\delta}\right|_{\delta=0} = \frac{T_1 T_s - \frac{T_1 T_2^2}{4}}{T_s^2 - \left(\frac{T_1 T_2}{4}\right)^2}. \tag{36}$$

The cross polarization coupling strength T_s plays an important role in determining the delay or advancement of a resonant Gaussian pulse. From Eq. (36) we have: when $\frac{T_2^2}{4} < T_s < \frac{T_1 T_2}{4}$, the group delay will be negative, and there will be pulse advancement [40]. For other values of T_s, there will be pulse delay [40]. For this case, although both

modes are undercoupled but the conditions $T_s > \frac{T_1 T_2}{4}$ and $\frac{T_1 T_2}{4} > \frac{T_2^2}{4}$ hold, the dispersion slope will be positive as in Fig. 14 and there will be pulse delay as in Fig. 15.

From Fig. 15, we have the pulse delay or positive position shift of the throughput pulse versus input pulse when the input pulse is centered at the resonant frequency. By measuring the pulse delay τ_d and multiplying it by the pulse bandwidth (ideally, the linewidth $\Delta\nu_{\min}$ of the higher-Q mode), we can determine the delay-bandwidth product value (DBP), which is a fundamental parameter of an optical buffer [41].

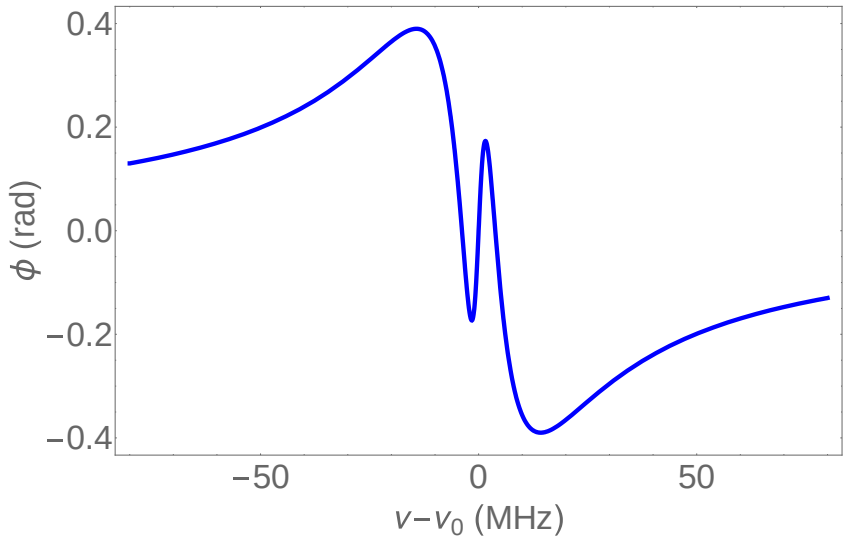

Figure 14. Modeled phase shift of the throughput field relative to the input field for CMIT.

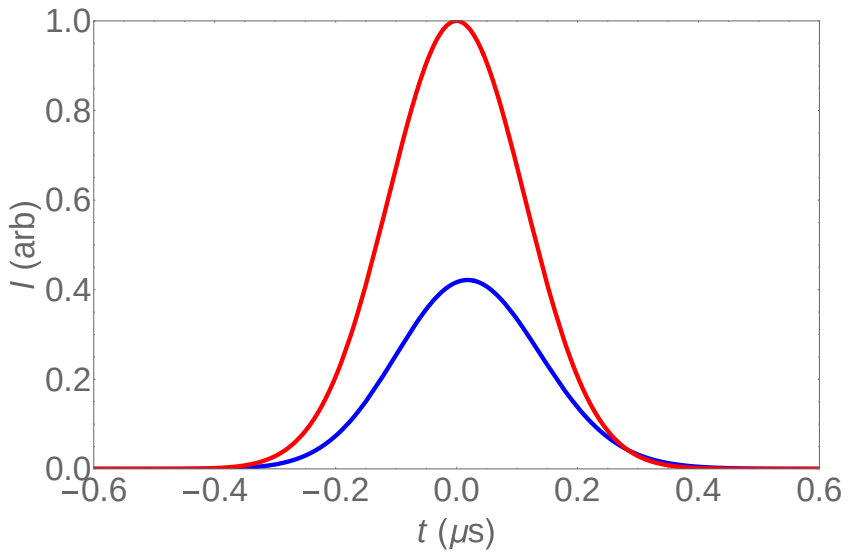

Figure 15. Modeled input Gaussian pulse: red; and throughput pulse: blue for CMIT.

When the two whispering gallery modes are close in quality factor and the cross coupling strength T_s is greater than the critical value, there will be a splitting in the center of the throughput spectrum, so the throughput has the ATS feature as in Fig. 16 rather than CMIT as in Fig. 13. In the next three figures, the input light is linearly polarized at 0^o, the detected throughput light has the same polarization as the input, Q_1 = 2×10^7, Q_2 = 1×10^8, M_1 = 0.8, M_2 = 0.7, T_s = 5×10^{-8}, both modes are undercoupled, the offset $\nu_2 - \nu_1$ = 0, and the pulse width is set to 230 ns. Note that the only difference between this case and the one of Figs. 13-15 is that Q_1 is now larger, so $\Delta\delta_1$ is smaller and thus so is $T_{critical}$; see p. 32.

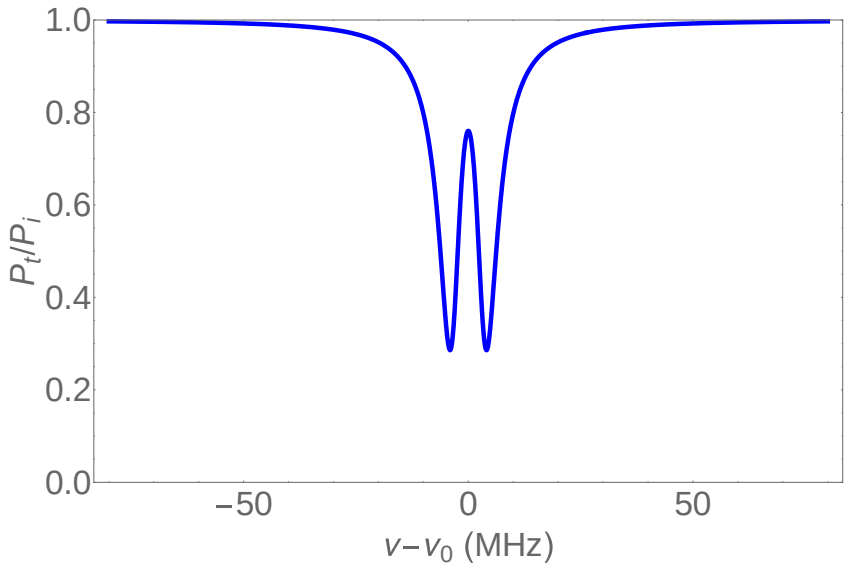

Figure 16. Modeled ATS throughput spectrum.

For this case, although both modes are undercoupled but the conditions $T_s > \frac{T_1 T_2}{4}$ and $\frac{T_1 T_2}{4} > \frac{T_2^2}{4}$ hold, the dispersion slope will be positive as in Fig. 17 and there will be pulse delay as in Fig. 18.

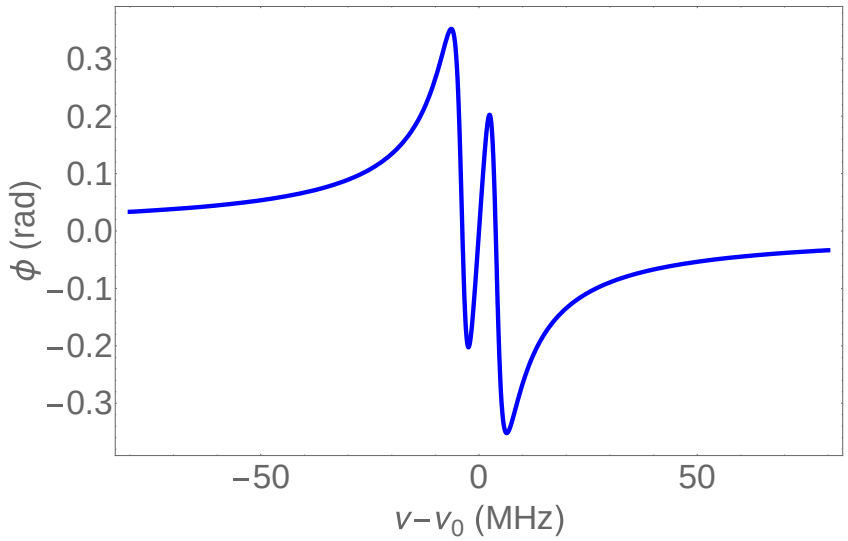

Figure 17. Modeled phase shift of the throughput field relative to the input field for ATS.

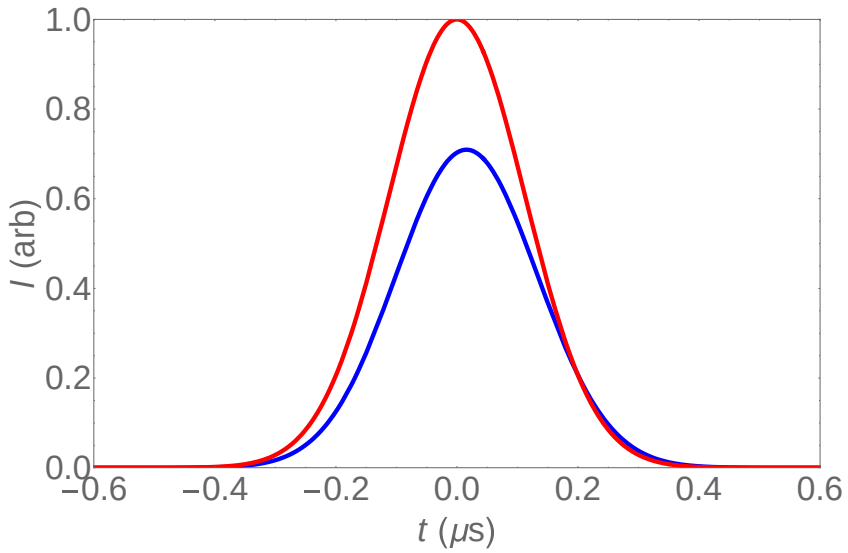

Figure 18. Modeled input Gaussian pulse: red; and throughput pulse: blue for ATS.

For other combinations of the input parameters, the throughput can have the shape of a deep dip, which is referred to as coupled mode induced absorption (CMIA) as in Fig.

19. In the three figures below, the input light is linearly polarized at 0^o, the detected throughput light has the same polarization as the input, Q_1 = 5×10^6, Q_2 = 1×10^8, M_1 = 0.5, M_2 = 0.9, T_s = 1.6×10^{-8}, both modes are overcoupled, the offset $\nu_2 - \nu_1$ = 0, and the pulse width is set to 230 ns.

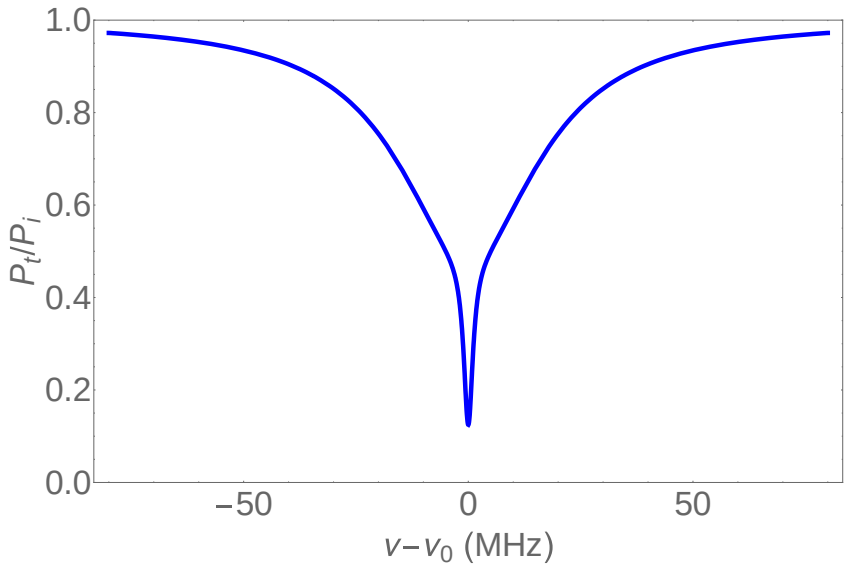

Figure 19. Modeled CMIA throughput spectrum.

For this case, although both modes are not strongly overcoupled but the condition $\frac{T_2^2}{4} < T_s < \frac{T_1 T_2}{4}$ holds, the dispersion slope will be negative as in Fig. 20 and there will be pulse advancement as in Fig. 21.

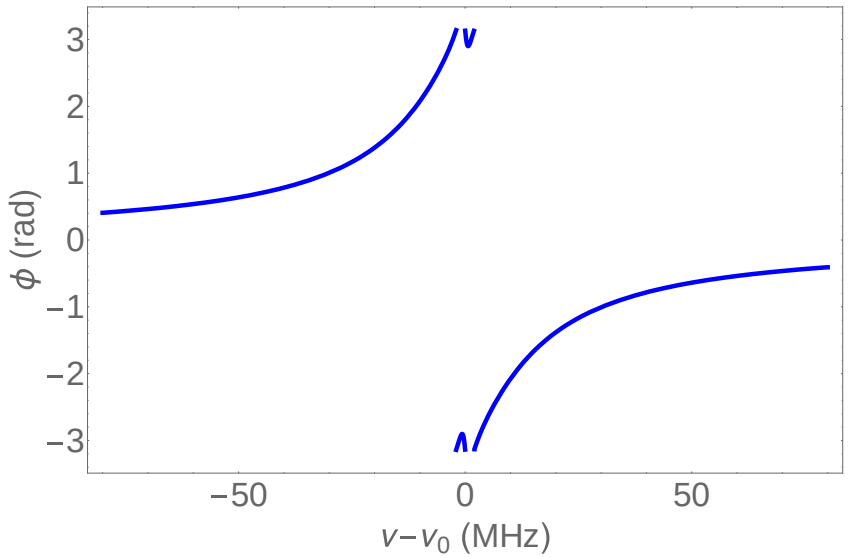

Figure 20. Modeled phase shift of the throughput field relative to the input field for CMIA.

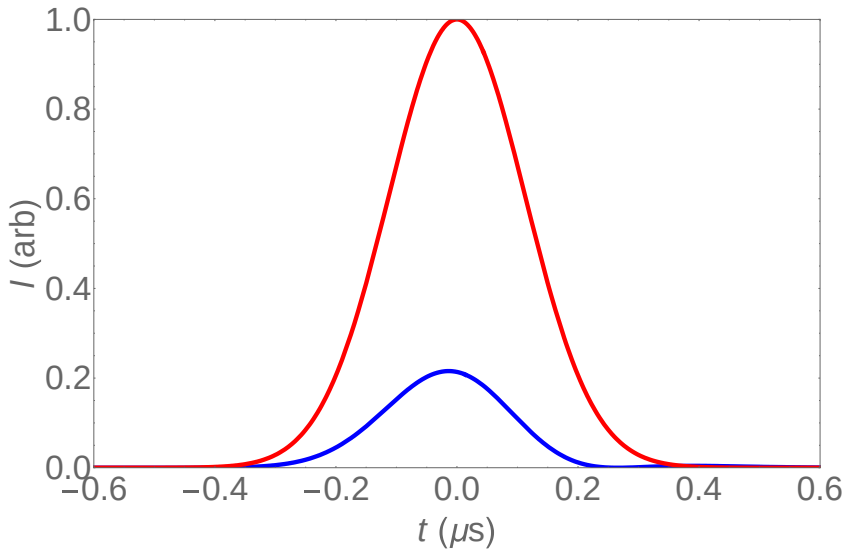

Figure 21. Modeled input Gaussian pulse: red; and throughput pulse: blue for CMIA.

Pulse delay, which seems to be created only by CMIT, can now also be produced by CMIA. Keeping the same input parameters as the above CMIA plus pulse advancement picture and reducing the cross polarization coupling strength to the value T_s = 1.26×10^{-9}, we can have the CMIA plus pulse delay picture. The throughput signal is shown in Fig. 22.

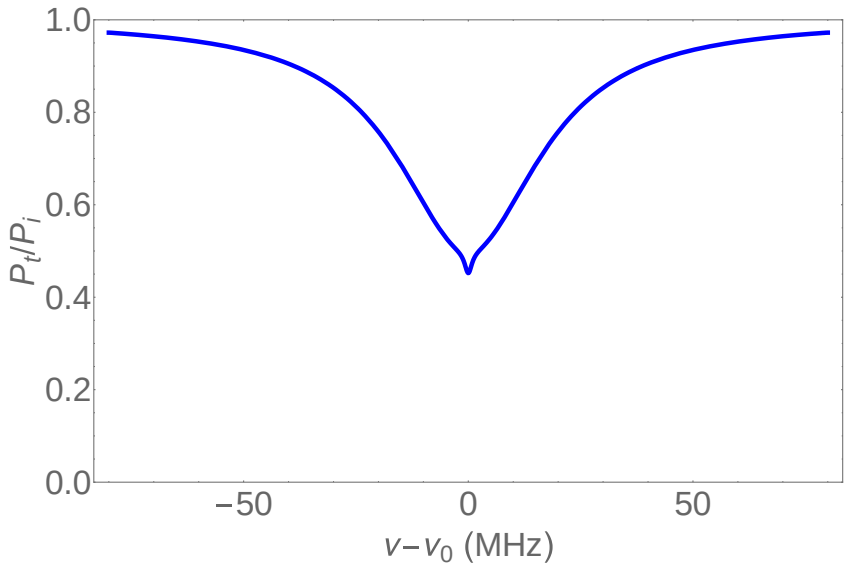

Figure 22. Modeled CMIA throughput spectrum.

For this case, although both modes are not strongly overcoupled but the conditions $T_s < \frac{T_2^2}{4}$ and $\frac{T_2^2}{4} < \frac{T_1 T_2}{4}$ hold, the dispersion slope will be positive as in Fig. 23 and there will be pulse delay as in Fig. 24.

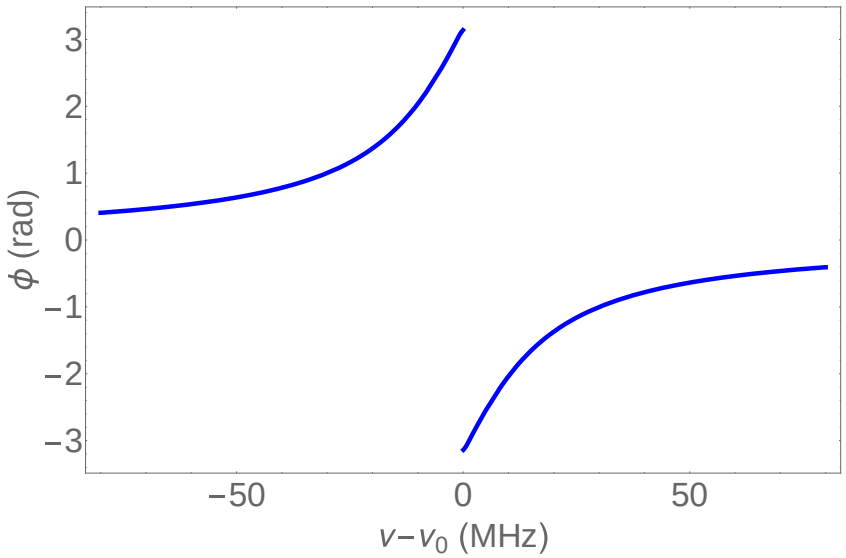

Figure 23. Modeled phase shift of the throughput field relative to the input field for CMIA.

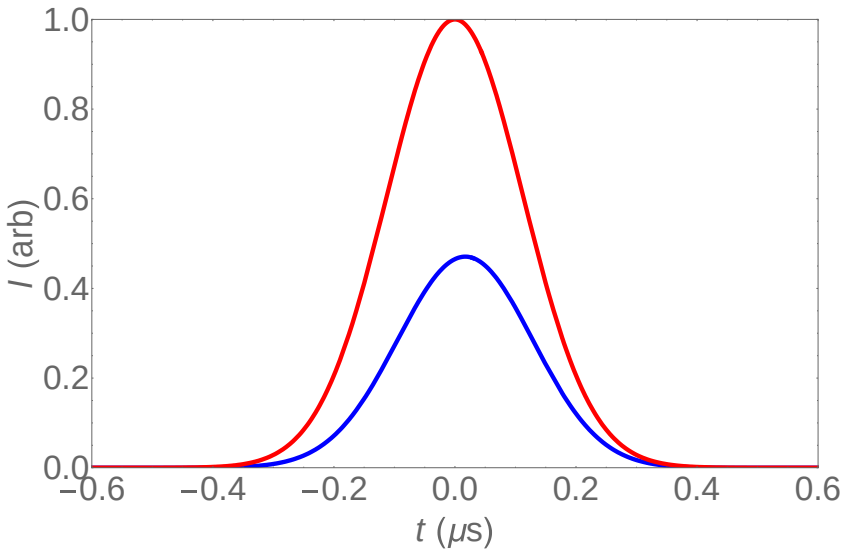

Figure 24. Modeled input Gaussian pulse: red; and throughput pulse: blue for CMIA.

III.4. Introduction to CPIT model

The model for the CPIT/CPIA experiment is almost the same as the one used for the CMIT/CMIA experiment except both θ and ψ are set to be equal to 45^o and T_s is minimized to the value 5×10^{-16}. This can be considered the condition of negligible cross polarization coupling between the coresonant orthogonally polarized TE and TM modes. When the input light is linearly polarized at 45^o with respect to the TE – TM basis of the microresonator, the input field is $E_i = (E_{f1} + E_{f2})/\sqrt{2}$ with E_{f1} and E_{f2} taken to be equal, and the throughput field is $E_r = E_{a1} = (E_{r1} + E_{r2})/\sqrt{2}$.

III.5. Relationship between CPIT and slow light

Some typical results of the model are presented here. Among all of the results reported here, TE and TM modes are assumed to be coresonant, $Q_1 << Q_2$, the cross polarization coupling probability T_s is minimized to the value of 5×10^{-16}, which can be considered the condition of no cross polarization coupling between TE and TM modes, the wavelength is taken to be 1550 nm, and the resonator radius is assumed to be 300 μm. In the following three figures for CPIT, the input light is linearly polarized at 45^o, the detected throughput light has the same polarization as the input, Q_1 = 5×10^6, Q_2 = 1×10^8, M_1 = M_2 = 0.05, both modes are overcoupled, the offset $\nu_2 - \nu_1$ = 0, and the pulse width is set to 230 ns. Figure 25 is the throughput spectrum of the input polarization component, Fig. 26 is the dispersion, and Fig. 27 shows the input pulse and the resonant throughput pulse.

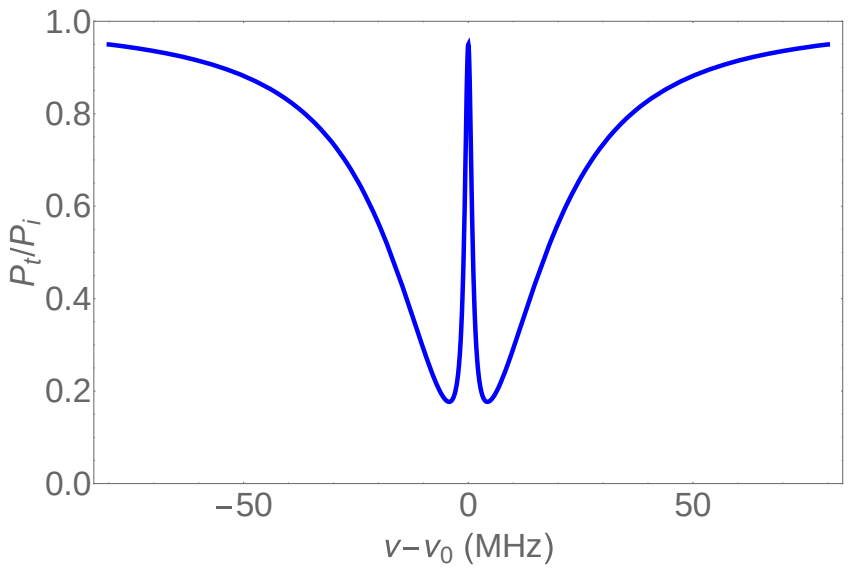

Figure 25. Modeled CPIT throughput spectrum [10].

From Fig. 25, we realize that under optimal experimental conditions, the throughput at the center of the transparency feature can approach 100%. The dispersion in the case of CPIT/CPIA, determined with no assumptions as to the input/output coupling regimes or *Q* values of the two WGMs, is given by [40]:

$$\left.\frac{d\phi}{d\delta}\right|_{\delta=0} = 2\frac{\frac{x_1^2}{T_1}(x_2+1)^2+\frac{x_2^2}{T_2}(x_1+1)^2}{(x_1+1)(x_2+1)(x_1x_2-1)} \tag{37}$$

This formula is correct for any combination of the input coupling regimes of the two modes. For the case of the CPIT thoughput spectrum seen in Fig. 25, the dispersion is positive and it is shown in Fig. 26.

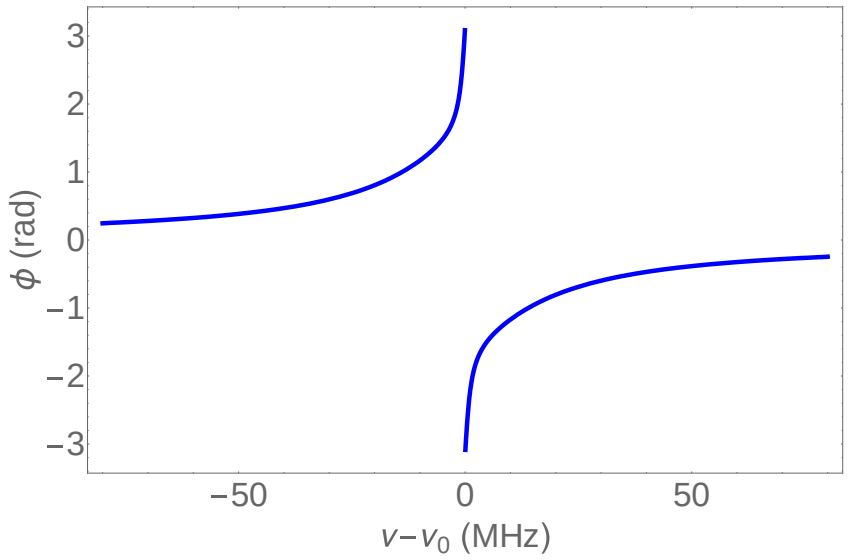

Figure 26. Modeled phase shift of the throughput field relative to the input field for CPIT [10].

The formula (37) leads to the fact that; when $x_1 x_2 > 1$, the dispersion is positive, there will be pulse delay [40], and when $x_1 x_2 < 1$, the dispersion is negative, there will be pulse advancement [40]. The fact that both WGMs are overcoupled for the case of CPIT above corresponds to the condition $x_1 x_2 > 1$, and the corresponding delay pulse picture is illustrated in Fig. 27.

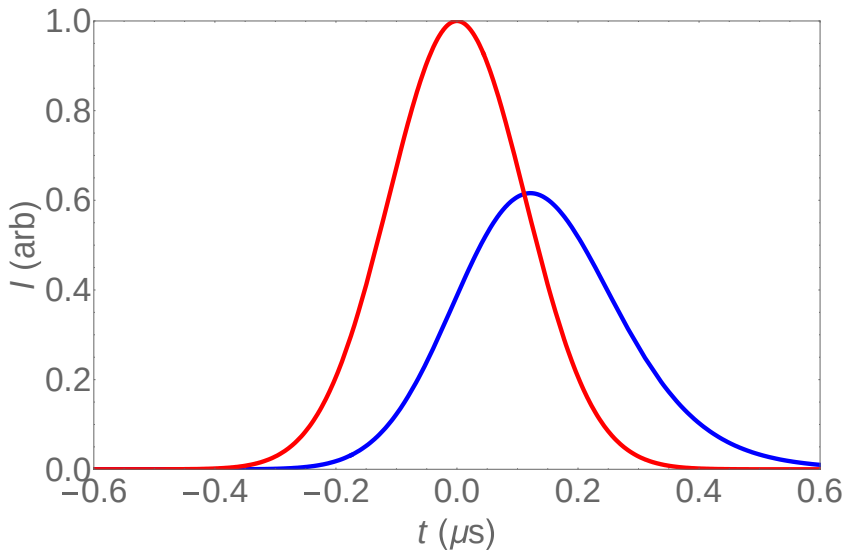

Figure 27. Modeled input Gaussian pulse: red; and throughput pulse: blue for CPIT [10].

For other combinations of the input parameters, the throughput can have the shape of a deep dip, which is referred to as coresonant polarization induced absorption (CPIA), and an example of such a CPIA throughput spectrum is shown in Fig. 28. In the three figures below, the input light is linearly polarized at 45^{o}, the detected throughput light has the same polarization as the input, Q_1 = 5×10^{6}, Q_2 = 1×10^{8}, M_1 = 0.65, M_2 = 0.65, T_s = 5×10^{-16}, both modes are undercoupled, the offset $\nu_2 - \nu_1$ = 0, and the pulse width is set to 230 ns.

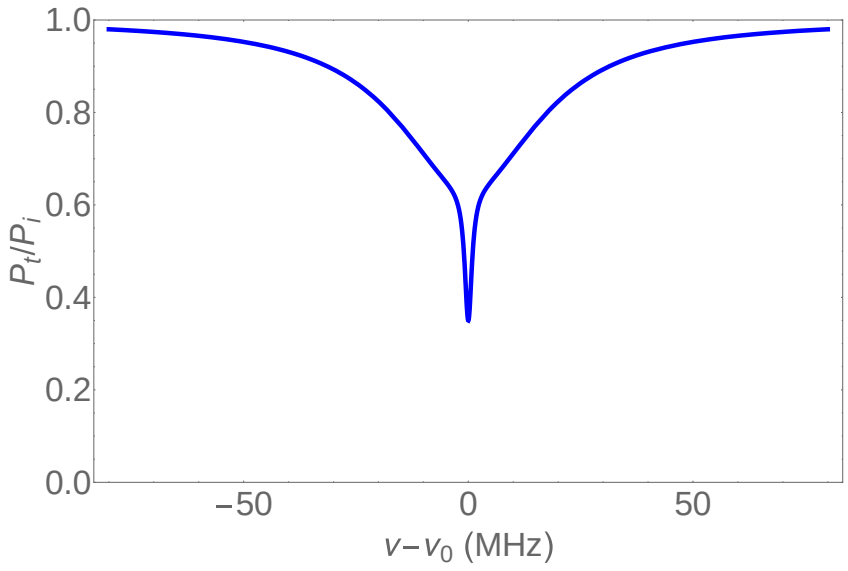

Figure 28. Modeled CPIA throughput spectrum.

For this case, $x_1 x_2 < 1$, so the dispersion slope will be negative as in Fig. 29 and there will be pulse advancement as in Fig. 30.

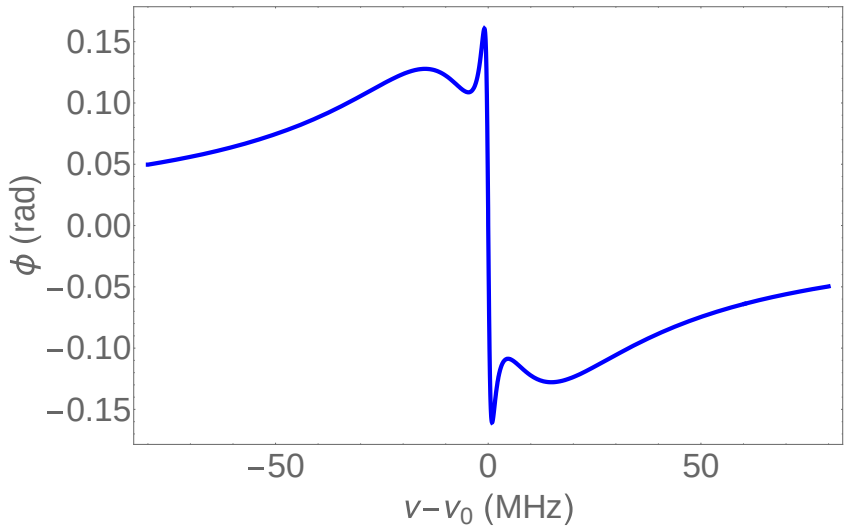

Figure 29. Modeled phase shift of the throughput field relative to the input field for CPIA.

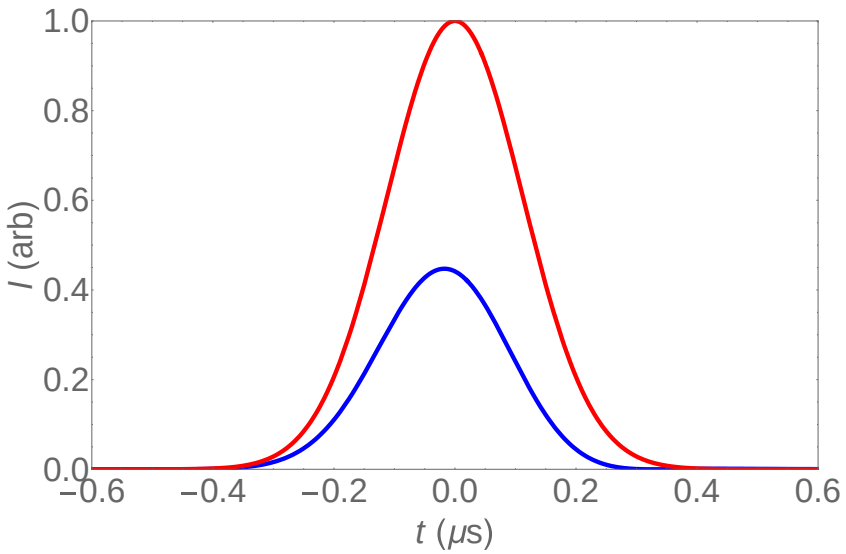

Figure 30. Modeled input Gaussian pulse: red; and throughput pulse: blue for CPIA.

Analogous to CMIA, CPIA can also produce pulse delay. By changing the input parameters, we can have the CPIA plus pulse delay picture. In the following three figures, the input light is linearly polarized at 45°, the detected throughput light has the same polarization as the input, $Q_1 = 5\times10^6$, $Q_2 = 1\times10^8$, $M_1 = 0.992$, $M_2 = 0.126$, $T_s = 5\times10^{-16}$, TE mode is undercoupled and TM mode is overcoupled, the offset $\nu_2 - \nu_1 = 0$, and the pulse width is set to 230 ns; the throughput signal is shown in Fig. 31.

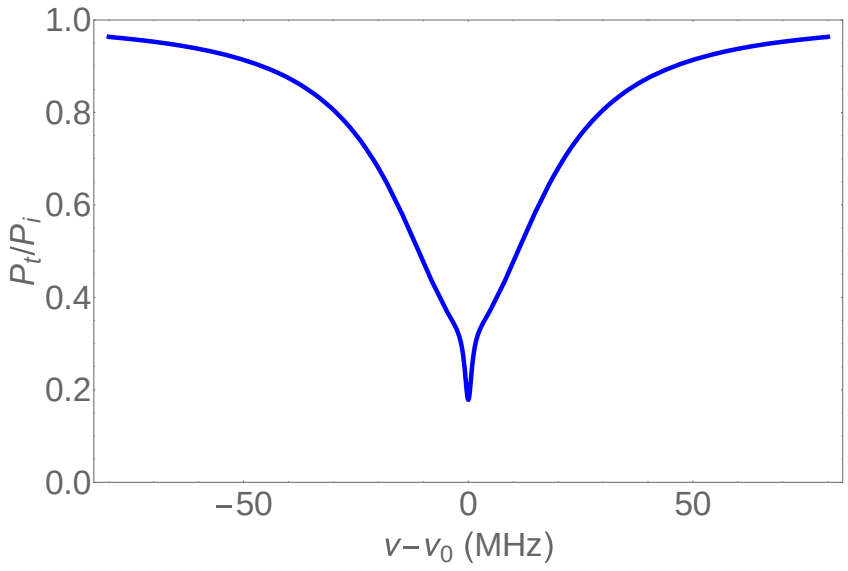

Figure 31. Modeled CPIA throughput spectrum.

For this case, $x_1 x_2 > 1$, so the dispersion slope will be positive as in Fig. 32 and there will be pulse delay as in Fig. 33.

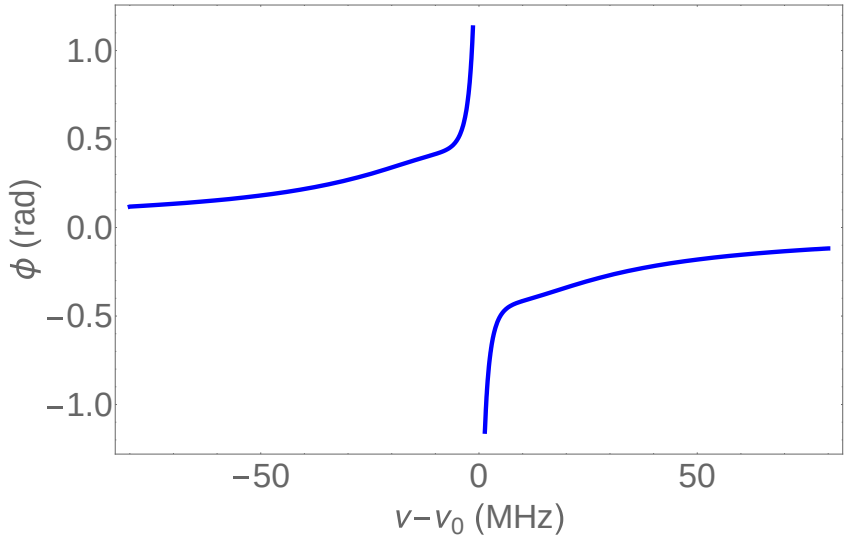

Figure 32. Modeled phase shift of the throughput field relative to the input field for CPIA.

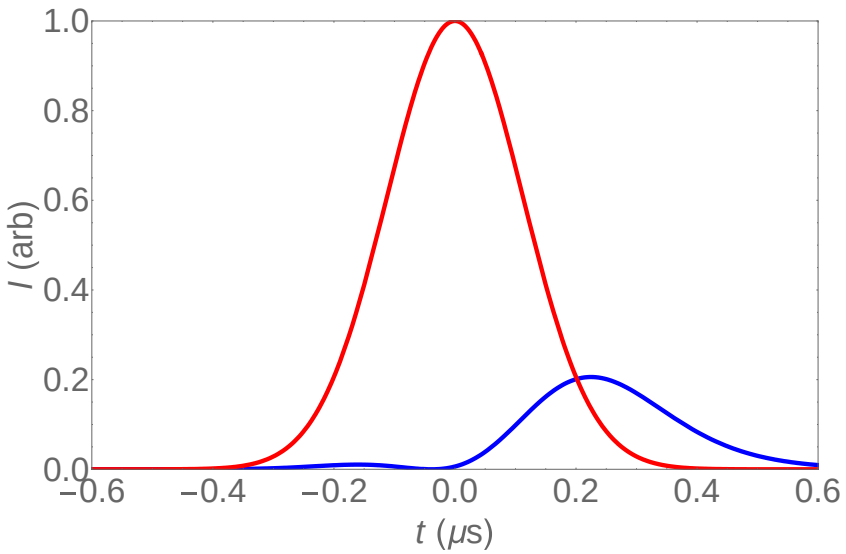

Figure 33. Modeled input Gaussian pulse: red; and throughput pulse: blue for CPIA.

CHAPTER IV

COUPLED MODE INDUCED TRANSPARENCY AND ABSORPTION

In this chapter, all the experimental procedures for producing the CMIT throughput signal plus pulse delay and CMIA throughput signal plus pulse delay and pulse advancement with both microsphere and hollow bottle resonator are presented. The Gaussian pulse creation and alignment as well as the advantages of hollow bottle resonators over microspheres are also mentioned. Experimental results for a number of cases, fitted with our model, are presented and discussed.

IV.1. Experimental setup

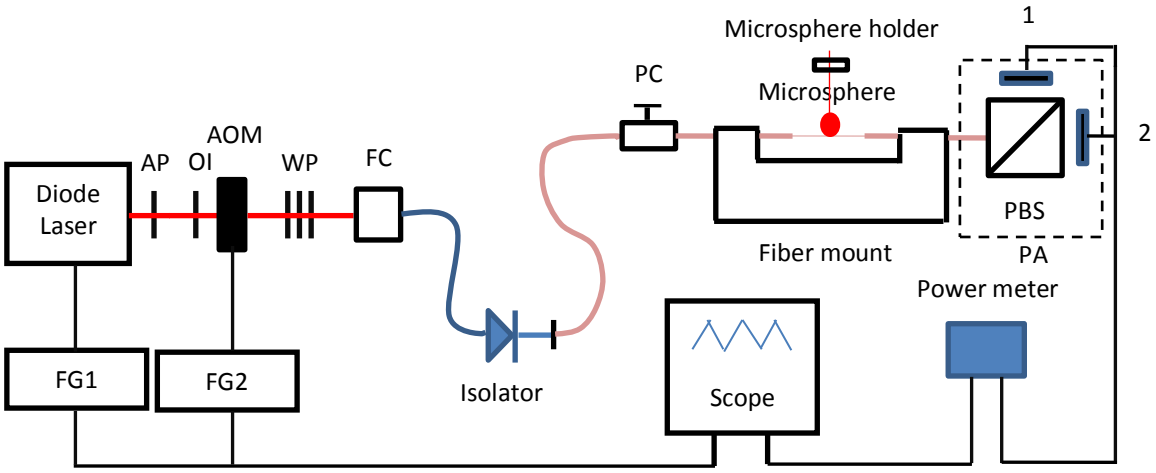

Figure 34. Experimental setup [42].

Figure 34 shows the experimental setup. The light source is a tunable diode laser (New Focus, model number: 6328) operating in the spectral range from 1508 nm to 1580 nm and scanned in frequency by function generator FG1 (Wavetek, model 395). After leaving the laser head, the light beam passes through the anamorphic prism (AP), which is used to convert the elliptical Gaussian beam into a circular Gaussian beam. The light then passes through an optical isolator (OI) to prevent any backreflected light from destabilizing the laser. An acousto-optic modulator (AOM) (Isomet, model 1250C), connected to an AOM driver (Isomet, model number: 235A-1) controlled by function generator FG2 (Wavetek, model 395), is then used to split the incoming beam into two outgoing parts: the zeroth-order undeflected beam of higher intensity with the same frequency and direction, and the first-order deflected beam of lower intensity with different frequency and direction from the incoming beam. In order to work with the pulse, we use the deflected beam. Depending on the experiment, whether getting the

throughput spectrum or measuring the pulse delay, the AOM driver is set to cw or Gaussian pulse light input regime for the microresonator. Before going to the fiber coupler (FC), the deflected light beam passes through a set of wave plates (WP) which are used to control the input polarization. Usually, the wave plates are adjusted to provide linearly polarized light. It is common in the lab to adjust the polarization angle with respect to the resonator's basis. This allows us to excite pure TE/TM modes or simultaneously the two. The fiber coupler FC launches the light into a single mode fiber. The fiber isolator, acting as an optical diode, is used to prevent any backward-propagating light from reflecting from the fiber input face and giving rise to Fabry-Pérot fringes in the throughput. The single mode fiber is also mounted in a compression based polarization controller, PC, for further regulation of the input light. The fiber is made adiabatically bi-tapered and brought into contact with the microresonator in its equatorial plane using a 3D translation stage. The microresonator is held by an apparatus for strain tuning. Depending on the resonator shape, either sphere or HBR, this tuner can be a compressor or a stretcher, respectively. In all cases, the resonator is kept inside an acrylic box to minimize the temperature fluctuations and other effects of air movement. The output signal is sent to a fiber coupled polarization analyzer (PA) which includes the polarizing beam splitter (PBS) and two detectors, 1 (Newport, model 818-IR) or fast detector (Thorlabs, model SIR5-FC), and 2 (Newport, model 818-IR) as in Fig. 34 to form a detector array. The entire detector array can be rotated about the incoming fiber axis to change the detection basis so that detector 1 can measure $|E_{r1}|^2$ or $|E_{a1}|^2$, and detector 2 can measure $|E_{r2}|^2$ or $|E_{a2}|^2$, respectively. The detector signals are then

captured with the power meter (Newport, model 2832-C) and sent to the oscilloscope which is further connected to a laptop computer (not shown) for additional data analysis.

IV.2. Gaussian pulse introduction

IV.2.1. Gaussian pulse creation

IV.2.1.1. Measurement of the beam diameter

Measurement of the beam diameter ($2w_0$) is necessary before using an acousto-optic modulator. If the beam diameter is smaller than the active aperture of the AOM, we can couple the light directly from the laser to the AOM, otherwise, we must focus the beam. In order to measure the beam radius w_0, we pass a 50-μm-diameter pinhole through the beam by mounting it on a rotating chopper blade, and detect the transmitted power in the form of the Gaussian pulse of Fig. 35. By blowing up the Gaussian pulse picture as in Fig. 35, we can measure τ_0, where $2\tau_0$ is the width of the pulse at the position that the pulse power P is equal to e^{-2} of its maximum value P_0. From Fig. 35, τ_0 is measured to be approximately 0.608 ms. The beam radius, w_0, is determined by using the equation: $w_0 = v\tau_0 = \frac{2\pi R\tau_0}{T}$, where v is the tangential velocity of the rotating chopper blade, R is the distance from the pinhole to the center of the blade, in this case R = 29 mm, T is the pulse period (the time spacing between two consecutive Gaussian pulses), in this case, T = 500 ms. And, the beam radius is calculated to be equal to 0.22 mm. So, the beam diameter, $2w_0$, is equal to 0.44 mm. However, due to the finite size of the pinhole, the beam diameter is somewhat smaller than that value and is approximately 0.4 mm. This value is smaller than the 0.75 mm active aperture of the

AOM, so that we can couple the light directly from the laser head to the AOM without using any lens.

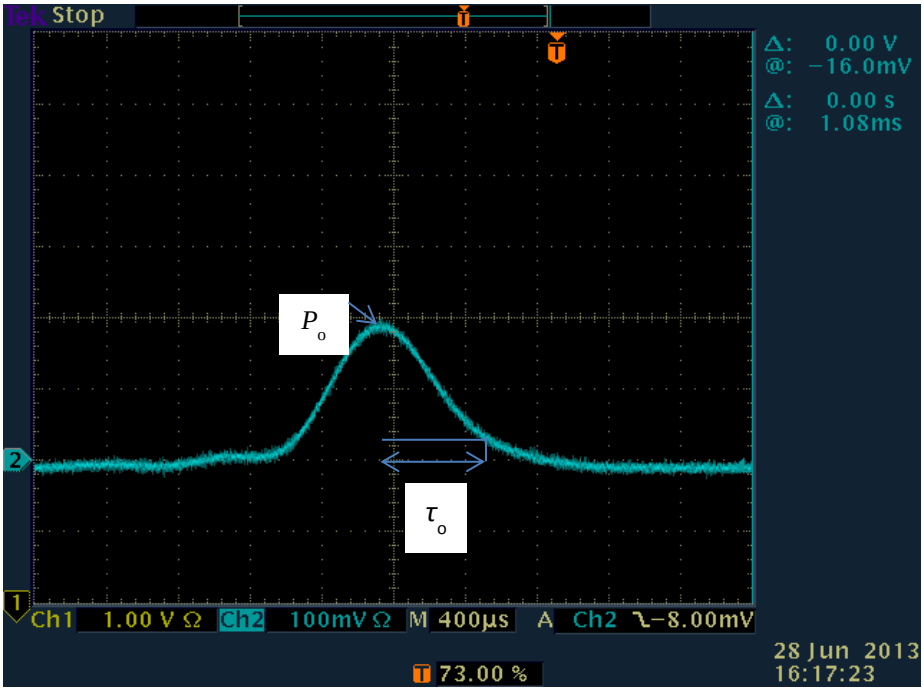

Figure 35. Gaussian pulse created by the pinhole attached to the chopper blade.

IV.2.1.2. Positioning the AOM

For the AOM used in this experiment as in Fig. 36 (Isomet, model 1250C), the nominal angle between the undeflected and deflected beams is 2θ, where $\theta = 2.45^o$.

The diffraction efficiency is measured to be approximately 8% at maximum deflected beam power, which is lower than the nominal value of 10% because of the power lost due to the imperfect antireflection coating of the modulator, angular misalignment, or tighter focusing (spot size smaller than the active aperture of the modulator) that increases the beam divergence.

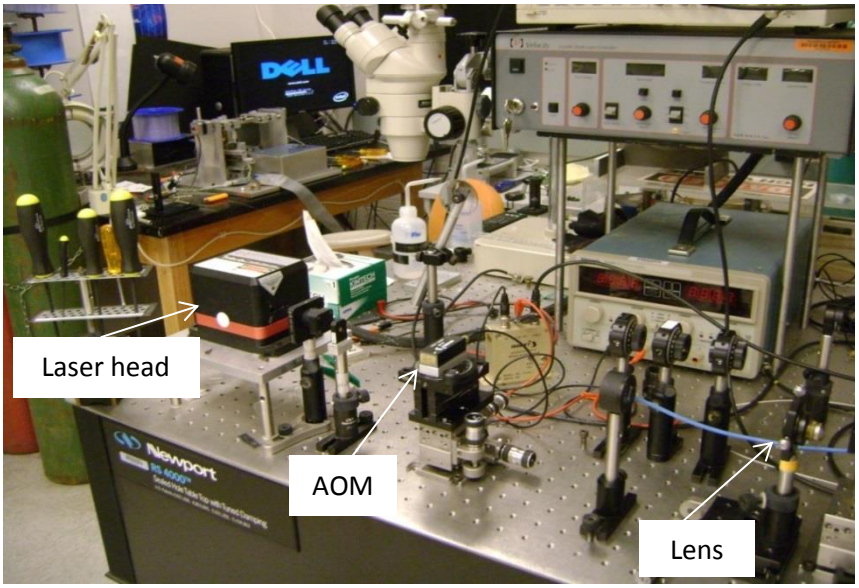

Figure 36. AOM positioning.

IV.2.1.3. Gaussian pulse creation

The function generator used to drive the AOM to create pulses (FG2 in Fig. 34) is an arbitrary waveform generator that can be programmed to create a truncated Gaussian pulse given by the formula $P = P_0(e^{\frac{-t^2}{\tau^2}} - \zeta)$, where P_0 is the maximum power, τ is the value of time t at which power $P = \frac{P_0}{e}$, and ζ = 0.01, which is used to ensure that the power P drops to zero at a finite time (making a pulse with compact support). In our experiment, the bandwidth of the Gaussian pulse is approximately equal to the linewidth $\Delta\nu_{\min}$ of the higher-Q mode, so its minimum temporal width (FWHM) is given by $\Delta t_o = \frac{0.441}{\Delta\nu_{\min}} = \frac{0.441Q\lambda}{c}$. For example, with Q = 10^8, λ = 1550 nm, c = 3×10^8 m/s, $\Delta t_o \approx$ 230 ns. The time constant τ is thus determined to be equal to 138 ns. The

Gaussian pulse waveform is constructed by using Mathematica to create discrete values and the **Sequence** program of the FG2 to connect them successively. For the **Sequence** setup regime, the sequence consists of two parts whose names are Seg1 and Seg2. In the Seg1 part; the waveform is chosen to be **trial** (a handmade 54 point Gaussian waveform with FWHM of 230 ns), advance is chosen to be **count,** and count is chosen to be **1**. In the Seg2 part; the waveform is chosen to be **line** (a 12 point handmade straight line), advance is chosen to be **count**, and count is chosen to be **5**. The period of the **trial** waveform is set to 540 ns and the period of the **line** waveform is set to 120 ns (in order to align the throughput optical Gaussian pulse from the fast detector with the electrical Gaussian pulse obtained directly from the second function generator FG2) as in section IV.2.2. Finally, an electrical pulse of Gaussian shape (shown in yellow) as in Fig. 37 was produced.

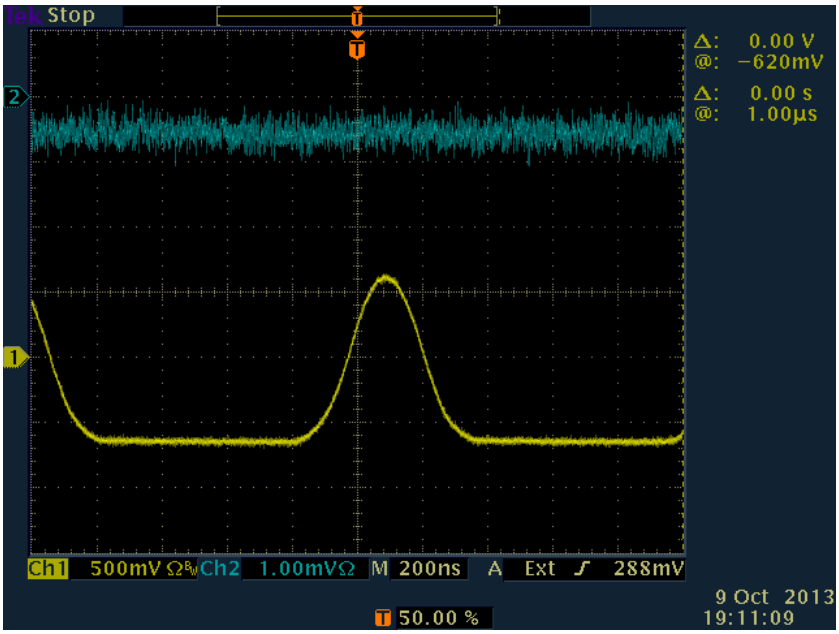

Figure 37. Electrical Gaussian pulse; yellow lower trace.

Since the AOM has a finite response time, the actual width of the created optical Gaussian pulse is somewhat wider than the FWHM of the electrical Gaussian pulse. The transit time of the acoustic wave τ_{AOM} (generated by the AOM) across the Gaussian laser beam is approximately 100 ns. If we treat the time response of the AOM to a delta-function electrical pulse as Gaussian, the actual width of the optical Gaussian pulse is roughly: $\Delta t \approx \sqrt{\Delta t_o^2 + \tau_{AOM}^2} \approx 250$ ns.

IV.2.2. Alignment of the pulse

When working with the Gaussian pulse, the AOM driver input must be switched from **dc**. Experimental data showed that the pulse seen by the fast detector (detector 1) is delayed by approximately 1140 ns with respect to the pulse produced by the function generator FG2.

Thus, the pulse period was adjusted to be 1.14 μs so that the n^{th} throughput pulse from the fast detector will be aligned with $(n+1)^{st}$ pulse from function generator FG2. In the following figures, Fig. 38 shows the delay time between two square pulses when the pulse period has not been adjusted: the blue square pulse is the fast detector signal and the yellow square pulse is the FG2 output; Fig. 39 is the alignment of two square pulses after adjusting the pulse period to 1.14 μs.

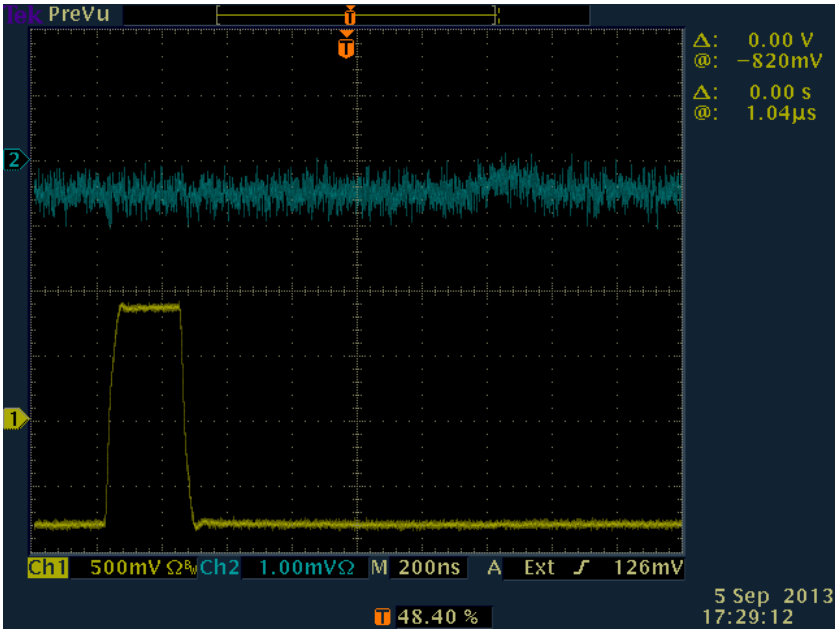

Figure 38. Pulse delay between FG square pulse (yellow trace) and fast detector pulse (blue trace).

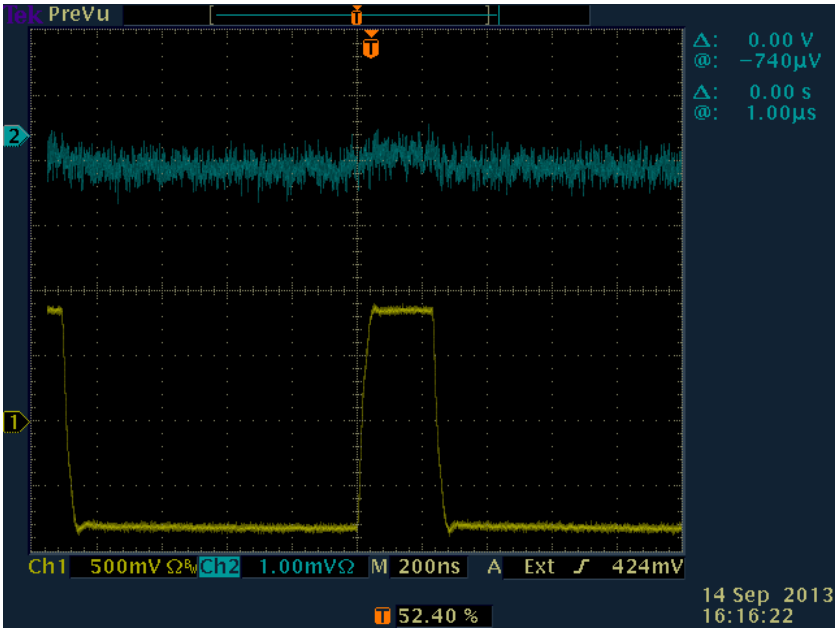

Figure 39. Pulse alignment between FG square pulse (yellow trace) and fast detector pulse (blue trace).

After the alignment of the square pulse, the Gaussian pulse with narrower bandwith has been used instead for all experiments. Fig. 40 shows the throughput spectrum when the laser is unmodulated, and Fig. 41 shows the throughput spectrum when the laser is modulated by the Gaussian pulse train. The delay or advancement of the Gaussian pulse is determined by comparing the actual position of the resonant throughput pulse with respect to the off resonant throughput pulse. Here, "resonant" means that the pulse center frequency coincides with the local extremum in the throughput, such as the peak within the left dip in the blue upper trace in Fig. 41, even though this may not be strictly resonant with the lower-*Q* WGM. In order to have a good feeling for the delay or advancement of the resonant throughput pulse, during the experiment process, we use the electrical Gaussian pulse as a reference. The example for the case of off resonant throughput pulse is shown in Fig. 42, and the example for the case of resonant throughput pulse is shown in Fig. 43, respectively.

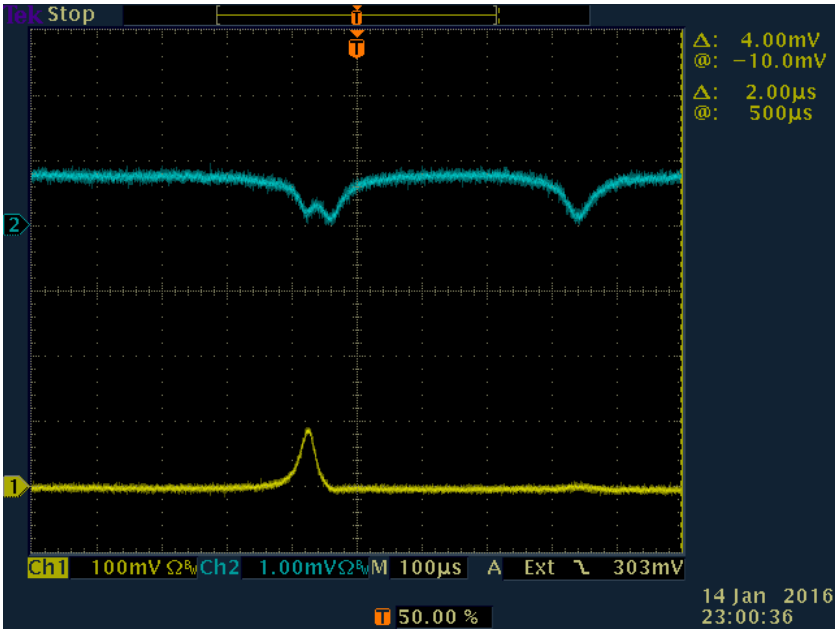

Figure 40. Throughput spectrum without fast detector pulse (blue trace).

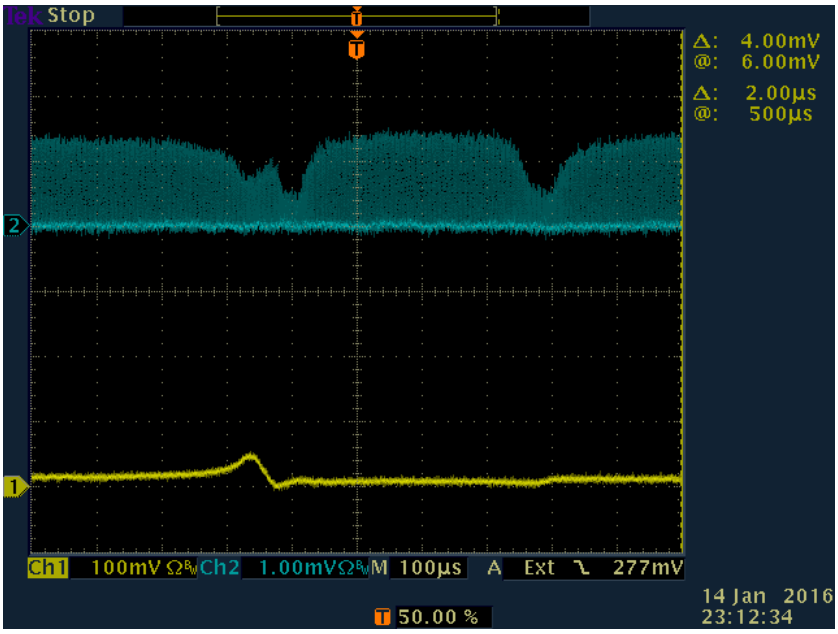

Figure 41. Throughput spectrum with fast detector pulse (blue trace).

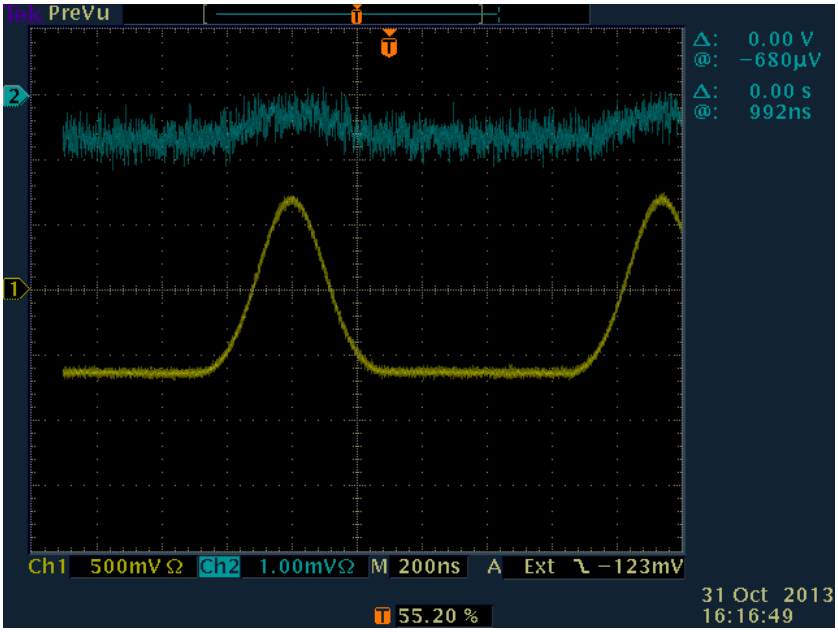

Figure 42. Off- resonance coincidence between the input Gaussian pulse (yellow trace) and throughput Gaussian pulse (blue trace).

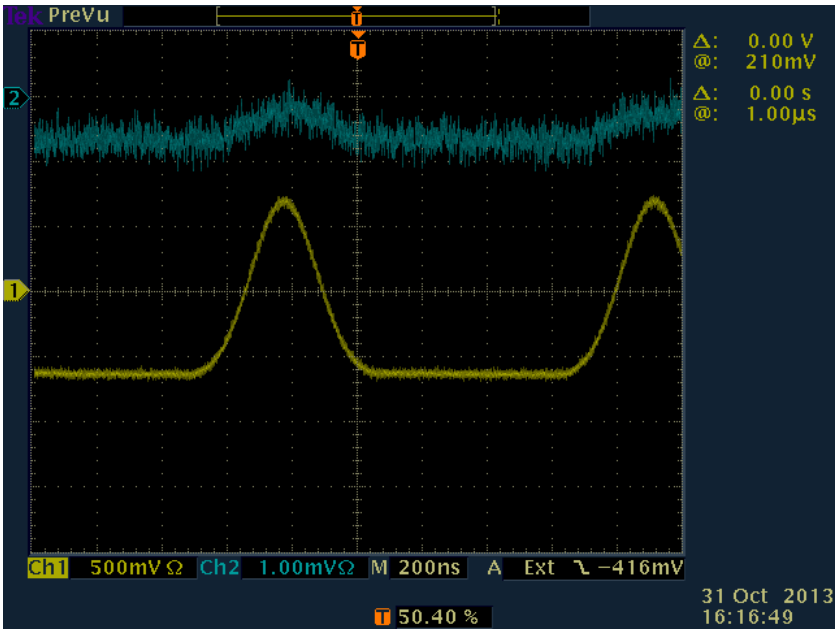

Figure 43. On- resonance pulse delay between the input Gaussian pulse (yellow trace) and throughput Gaussian pulse (blue trace).

IV.3. Whispering gallery microspheres

Dielectric materials have long been used as waveguides and optical resonators. The whispering gallery mode structure of a dielectric sphere is an example in classical electromagnetism, but it has newly realized practical relevance. The excellent transparency of modern fused silica allows the fabrication of microspheres whose WGMs have extremely low losses, allowing such spheres to be used as microresonators with very high quality factor *Q*.

A high-*Q* microsphere is fabricated from an optical fiber by melting the end with a hydrogen-oxygen minitorch; surface tension then produces a remarkably smooth and nearly perfect sphere, which is left attached to a stem for manipulation as in Fig. 44. A WGM is essentially the limiting case of propagation, by total internal reflection, around a

great circle of a microsphere, as the number of internal reflections becomes very large and the circumference equals an integral number of wavelengths of the light. A portion of the mode is evanescent, extending a small distance outside the microsphere. This permits excitation of these modes by evanescent wave coupling and allows the light to interact with matter on or near the sphere's surface.

Two different polarizations are possible for WGMs; the TE modes are essentially tangentially polarized while the TM modes are essentially radially polarized. The WGM field is described in terms of spherical Bessel functions and spherical harmonics. Three numbers, *q*, *l*, and *m*, characterize a WGM: the mode number *l* is the angular momentum quantum number of the circulating light, the mode order *q* is the number of radial maxima of the mode's intensity distribution, *m* is the number of wavelengths around the circumference, and $l-|m|+1$ gives the number of axial intensity lobes [28].

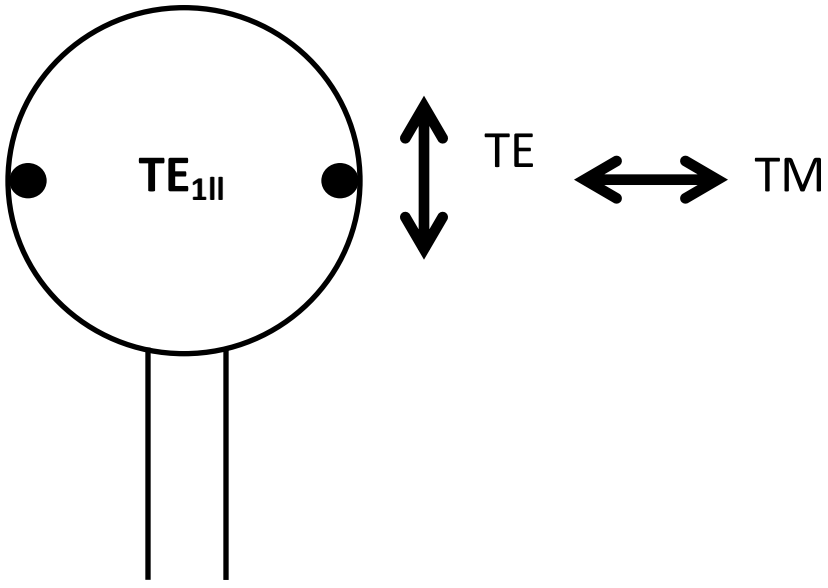

Figure 44. Silica microsphere and the fundamental whispering gallery mode structure TE_{1ll} [28].

The most useful WGMs are restricted to the vicinity of the sphere's equator and have $|m| \cong l$, with the fundamental WGM having $q = 1$ and $|m| = l$. The external, or evanescent, field decays approximately exponentially with distance from the surface with a decay length somewhat less than the wavelength. Slightly different confinement of the two polarizations, deriving from the polarization dependence of the total internal reflection phase shift, causes the effective refractive index to depend on polarization, so TE and TM modes with the same *q*, *l*, and *m* have different frequencies. For most applications, it is desirable that light be coupled into and out of a low order WGM with high efficiency and evanescent wave coupling can be accomplished by using tapered fibers.

IV.4. Production of CMIT with microspheres

For this experiment, one function generator (FG1; Wavetek, model 395) is connected to the laser controller (New Focus, model number: 6300) as in Fig. 45 in order to scan the laser in frequency, where the peak-to-peak voltage V_{pp} is set to 600 mV. This reading actually produces a voltage V_o which is twice as large. The disagreement between the voltage V from the FG1 readout and the true value of the delivered voltage V_o can be explained as follows. The function generator FG1, whose circuit is given in the rectangular dashed box with output impedance $R1$ shown in Fig. 45, is connected to the laser controller, whose input impedance is $R2$. The readout voltage V is calculated internally assuming that $R2 = R1 = 50\ \Omega$; however, $R2$ is actually 5 kΩ, so the voltage delivered is nearly V_o, which is twice as large as the readout. Thus V_{pp} is actually equal to 1.2 V, and the peak voltage V_p = 600 mV.

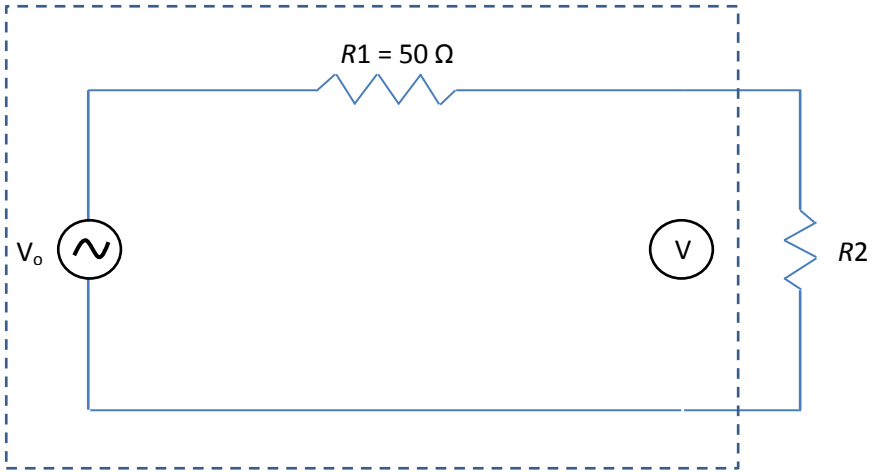

Figure 45. Function generator FG1 circuit (rectangular dashed box) connected with the laser controller *R2*.

The scan range (the range over which the laser frequency is shifted) produced by the function generator FG1 (Wavetek, model 395) is given approximately by the formula:

$$\text{scan range} = 5V_p + 2V_p^2, \tag{38}$$

where the scan range is in GHz if V_p is in volts. When V_p = 600 mV, scan range = 3.7 GHz, as seen in Fig. 46. To scan the laser, we use a 12.5-Hz triangle wave with zero voltage offset, as shown in Fig. 47. The laser frequency-scans 3.7 GHz in one direction during the first half-cycle (40 ms) and then returns in the second half-cycle.

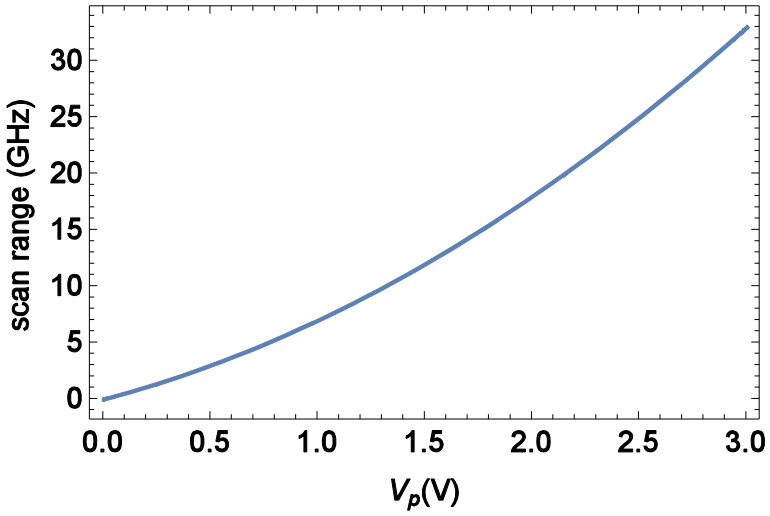

Figure 46. Scan range for laser with the limit 3V peak voltage.

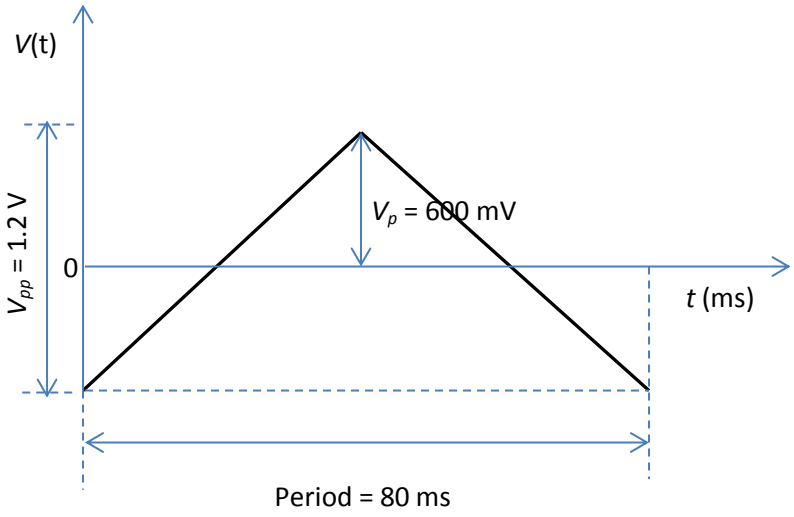

Figure 47. Scanning triangle wave for one cycle.

Another function generator (FG2; Wavetek, model 395) is connected to the Video input jack of the AOM driver (Isomet, Model number: 235A-1). The RF output jack of the driver is connected to the AOM (Isomet, model 1250C) in order to drive the modulator. On this second generator, the waveform is chosen to be **dc** or **Sequence** (Gaussian) depending on the specific experiment.

The laser power is increased to the value of 9.5 mW, and the wavelength is selected at 1548 nm by adjusting the knobs on the laser controller. The impedance is set to 50 Ω for both channels of the oscilloscope, the vertical offset for the slow detector channel is set to 0 V, and the vertical offset for the fast detector channel is set to -720 μV in order to align the oscilloscope trace with the baseline of that channel. The voltage scale for the fast detector channel is set to 1 mV/div, and for the slow detector channel it is set to 100 mV/div or 1V/div (depending on the CMIT or pulse experiment, respectively). The time scales are chosen to be 2 ms/div or 400 ns/div (depending on the CMIT or pulse experiment, respectively). The laser frequency-scanning triangle wave from FG1 is used as the external trigger source, with the trigger point at midscreen. Triggering on negative slope means that the laser frequency will be increasing from left to right on the oscilloscope screen. Since the screen width of 20 ms represents only half of the 3.7-GHz scan range, in order to observe the WGMs over the whole scan range, we have to adjust the trigger level. The sensitivity range is set to 5 (110 kHz response limit) for channel A (measuring TM output power) of the power meter, which is then connected to one channel (slow detector channel) of the oscilloscope. The TE output power is detected via the fast detector, which is then connected directly to the other channel of the oscilloscope.

In order to do the CMIT and pulse delay experiment, firstly we choose the waveform to be **dc** and later place the tapered fiber of 2 μm diameter in contact with the microsphere (approximately 600 μm in diameter) at one point on the equator by using a 3D translation stage. The light generated from the laser head will be coupled from the tapered fiber into the microsphere and circulate around the circumference of the sphere

via total internal reflection. After that it will be coupled back out to the tapered fiber on the opposite side and finally fall on the fiber coupled polarization analyzer (PA). By recording the power drop, we can select the WGMs.

To start the experiment, firstly the analyzer is rotated 45^o with respect to the vertical (~TE) axis. In this orientation, each detector (fast detector and slow detector) will display dips corresponding to both TE and TM modes. By rotating the polarization controller (PC) to make one type of mode disappear, the remaining type of mode can be determined after the analyzer is rotated back to its initial position. If the throughput power is rising on the fast detector channel and lowering on the slow detector channel on the oscilloscope screen, the excited modes are TE and on the contrary if the throughput power is lowering on the fast detector channel and rising on the slow detector channel, the excited modes are TM. For the case of excitation of modes of TE polarization, the 0^o position (corresponding to alignment of the analyzer basis with the microsphere basis) of the polarization analyzer is determined when the resonant throughput power measured from the fast detector is maximized and the resonant throughput power measured from the slow detector is minimized. The CMIT feature of the throughput power is seen by the fast detector when the input light is linearly polarized at 0^o (and excites TE modes) and it is recorded by the slow detector via rotating the polarization analyzer 90^o with respect to the microsphere basis about the incoming fiber axis.

To measure the relevant parameters of the CMIT coupling modes, the input polarization is changed to linear at 45^o by using the half-wave plate. At this point the throughput powers measured from the fast detector and the slow detector are equal, and the coresonant TE and TM pair of modes with very different quality factors are

determined. During the CMIT experiment, CPC can happen and change the true values of the mode parameters like quality factors, dip depths, and coupling regimes of the coresonant TE and TM modes. So in order to determine the mode parameters correctly, detuning the coresonant TE and TM modes is necessary. Since it is hard to compress the microsphere by using the PZT, we have to select the detuned modes accidentally. The widths and dip depths of the detuned modes can be measured directly by using the slow detector. The coupling regimes of the two detuned modes are determined by putting a segment of another tapered fiber in contact with the microsphere on the opposite side of the working tapered fiber. If the depth of the resonant dip becomes deeper, we have an overcoupled mode and if the depth of the resonant dip becomes shallower, we have an undercoupled mode. For this experiment, in order to get correct results, the quality factor *Q*, coupling regime and dip depth *M* of a mode (TM) were measured when the PA is at 0^o and that of the other mode (TE) are measured when the PA is rotated 90^o with respect to the vertical (TE) axis in order to ensure that both TE and TM mode parameters are measured by the slow detector.

To do the pulse experiment, we bring the detuned TE and TM modes back into the coresonant state and change the input light back to linear at 0^o by rotating the half wave plate. At this time the CMIT throughput shape is restored. The connector from channel A of the power meter to the oscilloscope is unplugged and a BNC cable is then used instead to connect the oscilloscope with the second function generator FG2 in order to display the reference electrical Gaussian pulse directly from FG2. By switching the waveform to **Sequence** (as shown in Fig. 41) and varying the time scale down to 400 ns/div, the pulse picture of CMIT can be recorded for both resonance and off resonance

cases. The FWHM of the electrical Gaussian pulses can be adjusted from FG2 according to the linewidth of the higher-*Q* mode (230 ns in this case). In order to have the correct comparison between the theoretical calculation and the experimental data for the pulses, the width of the input pulse in the model has been chosen to be equal to the FWHM of the off resonant throughput optical Gaussian pulse (approximately 250 ns). Since the throughput optical pulses are noisy, we have to do a Gaussian fit for both off resonant and resonant throughput optical Gaussian pulses in order to determine the pulse width and delay exactly. By comparing the relative positions of the optical resonant Gaussian pulse with respect to the optical off resonant Gaussian pulse on the fast detector channel, the experimental delay time is determined (8 ns in the first example shown below in Fig. 48). During this CMIT experiment process, the laser frequency is increasing from left to right on the oscilloscope screen as well as in Fig. 48 and all following throughput spectrum plots. The TE mode has dip depth M_1 = 0.79 and quality factor Q_1 = 6.5×10^6, and the TM mode has dip depth M_2 = 0.9 and quality factor Q_2 = 8.7×10^7. Both TE and TM modes are undercoupled. The CMIT experimental and numerical results presented here are plotted together. The experimental throughput is the normalized detector response, where the horizontal axis of the oscilloscope trace has been converted to frequency based on the laser scan range and speed. For some of the analytical comparisons, it is helpful to have an expression for the coupling loss T_j and total loss $\Delta\delta = T_j + \alpha_j L$, which can be found from the measured values of Q_j and M_j by using the following expressions, provided that the coupling regime is known [42]:

$$T_j = \frac{4\pi^2 na}{\lambda Q_j (1 + x_j^{-1})}, \tag{39}$$

$$M_j = \frac{4x_j}{(1+x_j)^2}. \tag{40}$$

In order to do the computer model fitting with the experimental throughput, the measured quality factors, dip depths, coupling regimes and microsphere radius are used as the input. The CPC strength T_s, the frequency offset of the higher-Q WGM from the lower-Q WQM $\nu_2 - \nu_1$, and the detuning of the pulse center frequency from ν_1 are used as the fitting parameters. The offset and pulse detuning are known approximately from the experimental results, and their values are refined by the fitting process; T_s is a completely free parameter. After getting a good fit, the values of T_s, offset, and pulse detuning are determined from the computer model. Imperfect numerical fit is most likely due to overlapping WGMs that can affect measurements, as described in more detail in Section IV.5.

Figure 48 below shows the fitting for both throughput spectrum and pulse response of a CMIT experiment using the scattering model. For this experiment, the microsphere radius is measured to be equal to 280 μm, and this value of microsphere radius is again used in the computer model for calculation. The uncertainty in $\log(T_s)$ is about 0.1 for all fitting in this dissertation, so T_s has an uncertainty of about 25%. The uncertainty in experimental pulse delay/advancement is about 5 ns throughout. This value is estimated as the uncertainty in evaluating the separation of the peaks of the two Gaussians that fit the experimental pulses. Larger delay/advancement errors can occur if the measured input and throughput pulses are not fully off resonance and at the central extremum, respectively.

IV.4.1. CMIT and pulse delay with microsphere

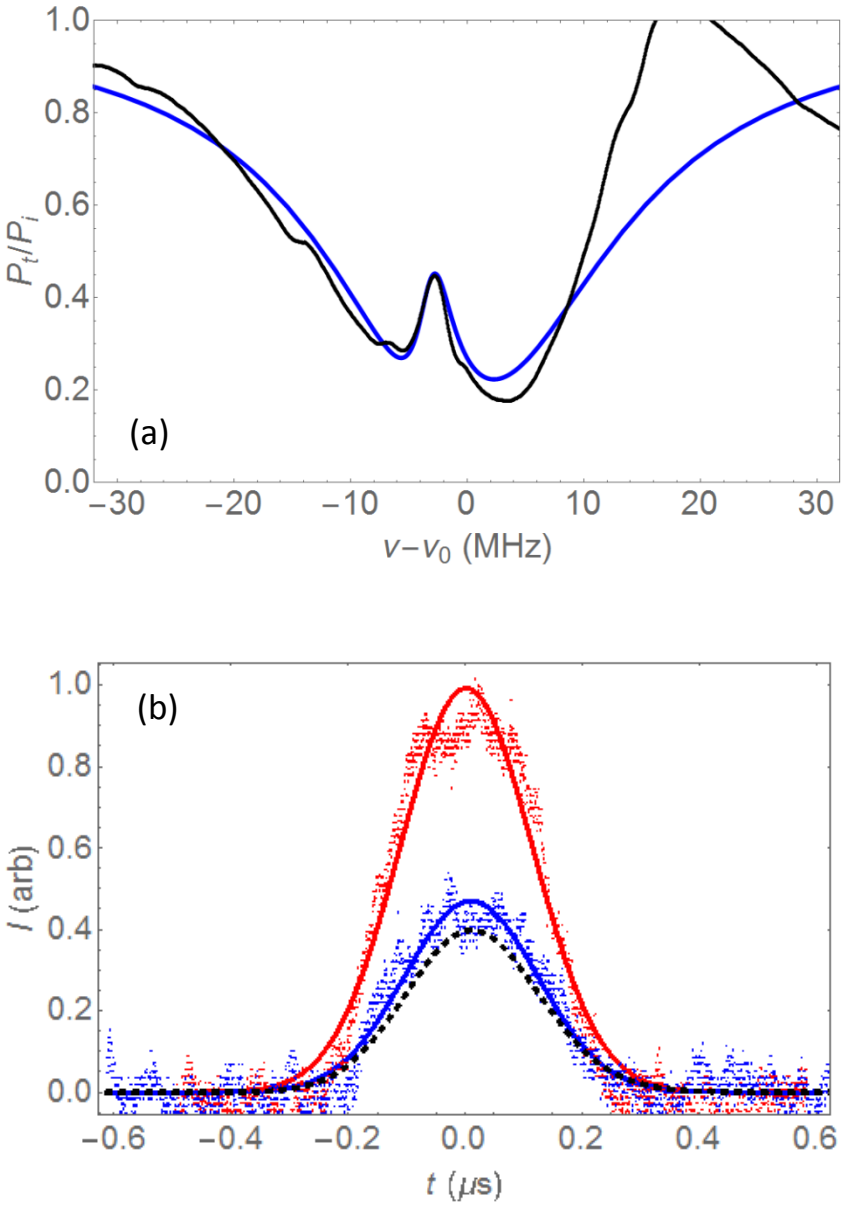

Figure 48. CMIT with 280-μm-radius microsphere. (a) Experimental (black) and model (blue) throughput spectra. (b) Experimental input (red) and throughput (blue) pulses, with an input pulse width of 255 ns and a delay of 8 ns, and model throughput pulse (dashed black), with a delay of 10 ns. Parameter values: M_1 = 0.79 (undercoupled), M_2 = 0.9 (undercoupled), Q_1 = 6.5×10^6, Q_2 = 8.7×10^7; offset = -3 MHz, T_s = 2.82×10^{-8}, pulse detuning = -2.8 MHz.

In part (a) of Fig. 48, the experimental data (in black) is slightly different from the model calculation (in blue) for the throughput spectrum fitting, showing that there is some overlap of nearby modes that leads to a minor disagreement between the theoretical calculation (blue solid curve) and experimental data (black dashed curve) for the throughput pulse response in part (b). The width of the transparency window is slightly greater than the width of mode 2 in this case. That the cross polarization coupling strength $T_s < T_{critical} = 13.4 \times 10^{-8}$ indicates that the throughput signal has CMIT shape. This is accounted for by the destructive interference between the direct and indirect excitation paths of TE modes. Although both TE and TM modes are not strongly overcoupled as assumed in Eq. (36), but the conditions $T_s > \frac{T_1 T_2}{4}$ and $\frac{T_1 T_2}{4} > \frac{T_2^2}{4}$ hold, the dispersion slope is positive and there will be pulse delay. The experimental delay-bandwidth product value is calculated to be 0.014.

IV.4.2. ATS and pulse delay with microsphere

When the quality factors of two modes are comparable and the intermodal coupling between TE and TM modes is greater than the critical value, the throughput signal is split into two dips. The splitting between the mode components is proportional to the intermodal coupling strength. For this experiment, the microsphere radius is measured again to be equal to 280 μm and the scattering model is used as well.

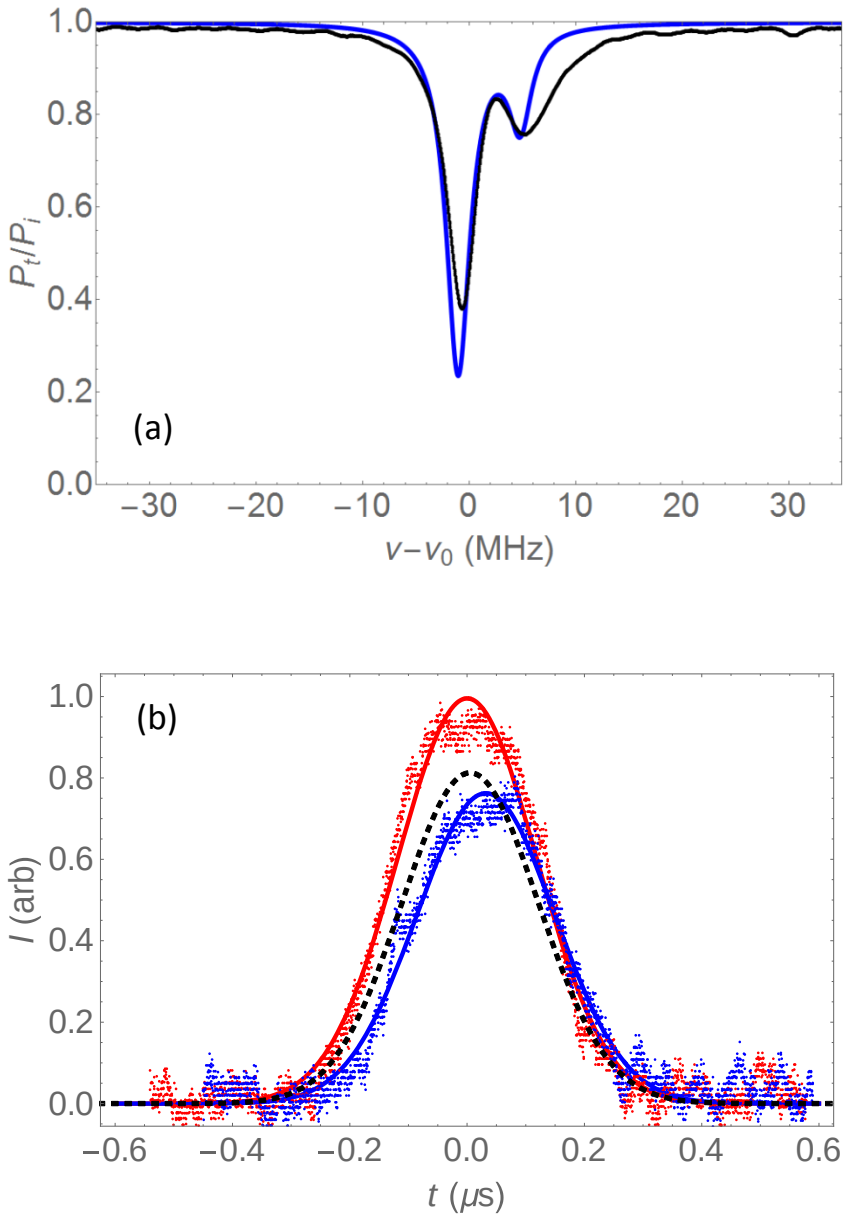

Figure 49. ATS with 280-µm-radius microsphere. (a) Experimental (black) and model (blue) throughput spectra. (b) Experimental input (red) and throughput (blue) pulses, with an input pulse width of 270 ns and a delay of 32 ns, and model throughput pulse (dashed black), with a delay of 13 ns. Parameter values: M_1 = 0.85 (undercoupled), M_2 = 0.6 (overcoupled), $Q_1 = 7\times10^7$, $Q_2 = 7.5\times10^7$; offset = 3.8 MHz, $T_s = 1.4\times10^{-8}$, pulse detuning = 3 MHz.

In part (a) of Fig. 49, the experimental data is a little different from the theoretical model for the throughput spectrum fitting showing that there is some overlap of nearby modes and as a result, there is a disagreement between the theoretical calculation and experimental data for the pulse response picture in part (b). $T_s > T_{critical} = 6.25 \times 10^{-12}$ indicates that CMIT has become ATS. In this case, although both modes are not strongly overcoupled as assumed in Eq. (36) and in fact $\frac{T_2^2}{4} > \frac{T_1 T_2}{4}$, the condition $T_s > \frac{T_1 T_2}{4}$ still holds, so the dispersion slope is positive and pulse delay is expected. The experimental delay-bandwidth product value is calculated to be 0.02.

IV.4.3. CMIA and pulse advancement with microsphere

When the coupling between TE and TM modes produces a throughput that has the form of a deep dip, we have coupled mode induced absorption (CMIA) as in Fig. 50 below. For this experiment, the rotational model was used to fit the experimental data (though, as discussed in Chapter VI, no difference from the scattering model is expected here) and the microsphere radius is measured to be equal to 285 μm.

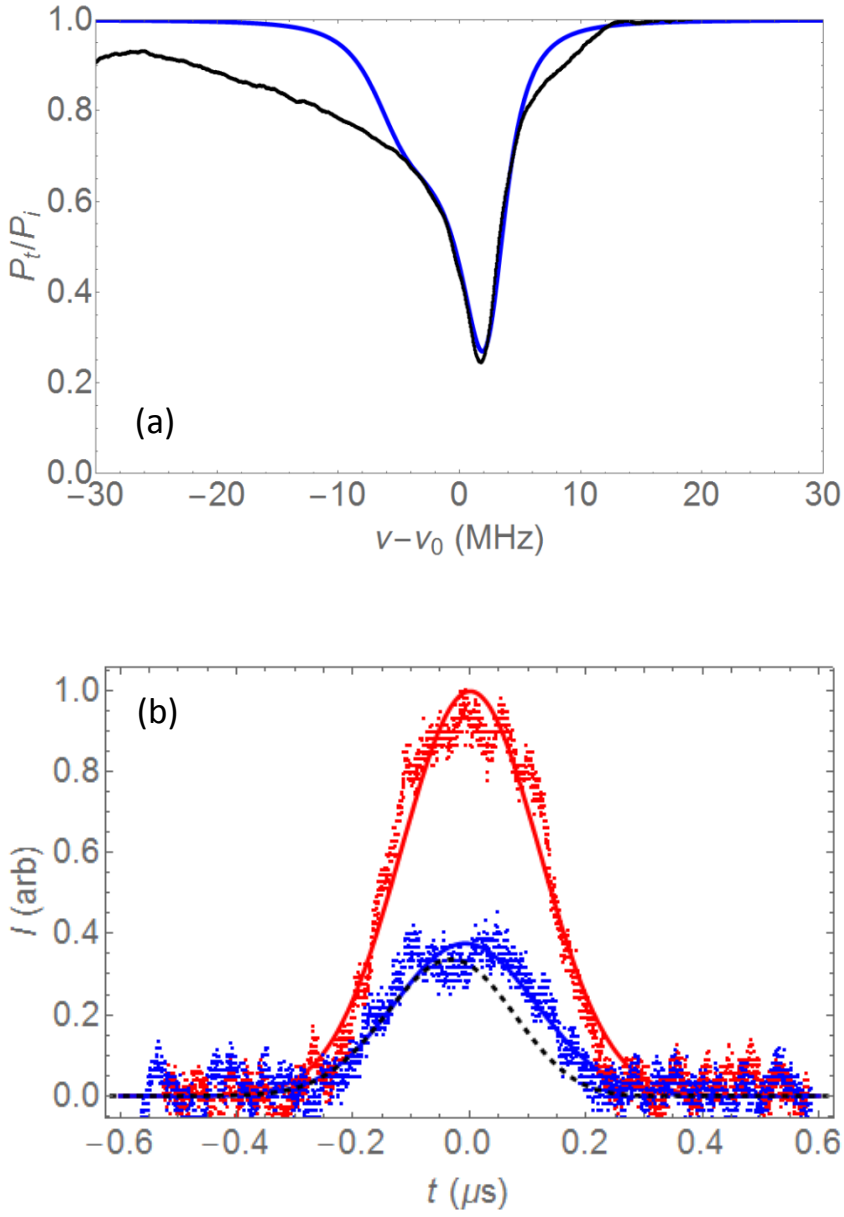

Figure 50. CMIA with 285-μm-radius microsphere. (a) Experimental (black) and model (blue) throughput spectra. (b) Experimental input (red) and throughput (blue) pulses, with an input pulse width of 275 ns and an advancement of 9 ns, and model throughput pulse (dashed black), with an advancement of 25 ns. Parameter values: M_1 = 0.86 (overcoupled), M_2 = 0.87 (overcoupled), Q_1 = 1×10^8, Q_2 = 1.8×10^7; offset = -3 MHz, T_s = 5×10^{-8}, pulse detuning = 1.8 MHz.

In Fig. 50, the throughput fitting used is reasonable. Because both modes are not strongly overcoupled, as assumed in Eq. (36), pulse advancement is still produced even though T_s is out of the negative group delay range. The predicted advancement is somewhat greater than the measured advancement, most likely because the experimental input pulse might not have been far enough off resonance. The experimental advancement-bandwidth product value is calculated to be 0.014.

IV.4.4. CMIA and pulse delay with microsphere

Pulse delay, which seems to be produced by CMIT/ATS, can also occur with CMIA as in Fig. 51 below. For this experiment, the microsphere radius is measured to be equal to 285 μm and the scattering model is used as well.

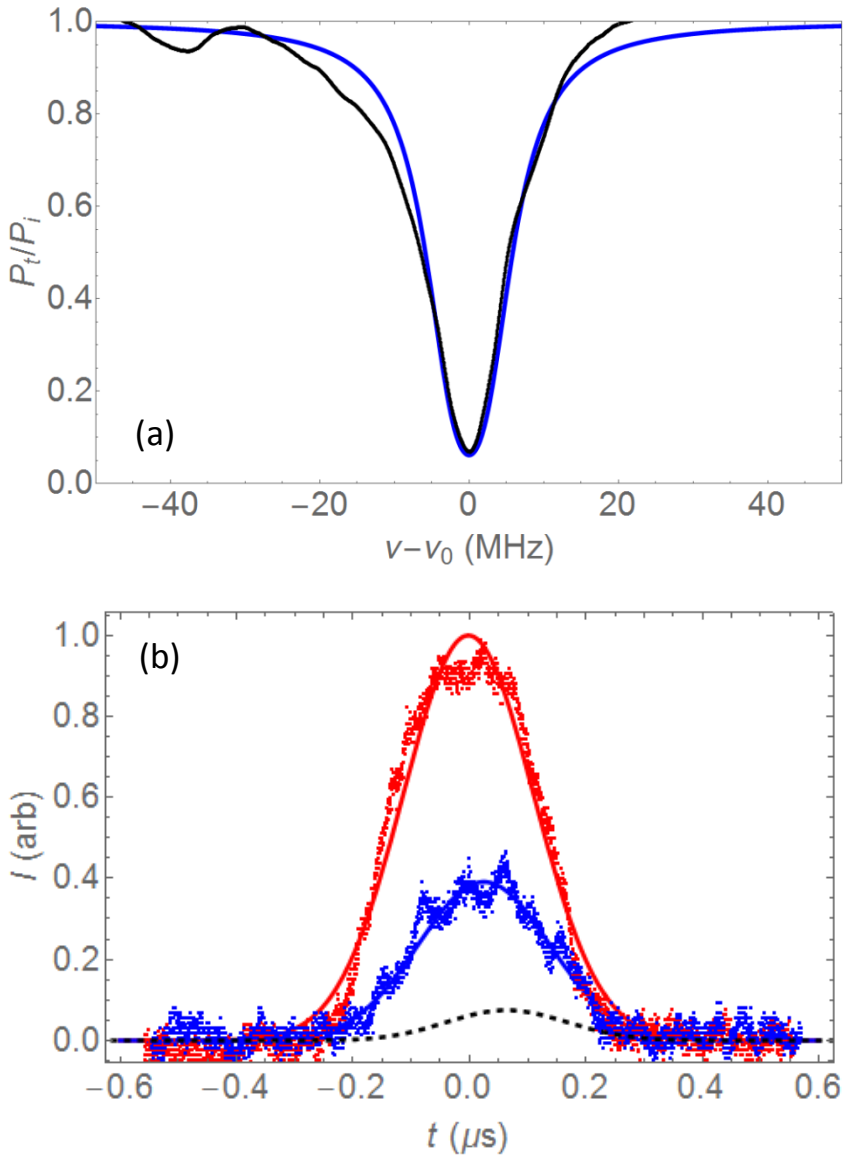

Figure 51. CMIA with 285-µm-radius-microsphere. (a) Experimental (black) and model (blue) throughput spectra. (b) Experimental input (red) and throughput (blue) pulses, with an input pulse width of 265 ns and a delay of 27 ns, and model throughput pulse (dashed black), with a delay of 60 ns. Parameter values: M_1 = 0.67 (overcoupled), M_2 = 0.88 (undercoupled), Q_1 = 1.63×10^7, Q_2 = 2.2×10^7; offset = 0 MHz, T_s = 2.0×10^{-8}, pulse detuning = 0 MHz.

In part (a) of Fig. 51, the throughput fitting is reasonable. Although both modes are not strongly overcoupled as assumed in Eq. (36), but the conditions $T_s > \frac{T_1 T_2}{4}$ and $\frac{T_1 T_2}{4} > \frac{T_2^2}{4}$ hold, the dispersion slope is positive and there will be pulse delay. In part (b) of Fig. 51, the experimental throughput pulse is higher in magnitude than the theoretical throughput pulse showing that either the resonant experimental throughput pulse is not truly resonant or the off-resonant pulse might not really be off-resonant. As a result, the experimental delay time is smaller than the theoretical calculation. The experimental delay-bandwidth product in this case is calculated to be 0.045.

IV.5. Hollow bottle resonator

When working with microspheres, there are some difficulties occurring during the experimental process. Firstly, the throughput spectrum is still messy due to the overlap of the nearby modes with respect to the mode of interest. This problem can be explained as follows: since the microsphere's surface has a strong polar (or axial) curvature, modes of various axial orders are not spread out spatially, so many of them can be simultaneously excited by tapered-fiber coupling; this behavior can result in spectral overlap of the modes. However, the axial free spectral range depends on the sphere's eccentricity [37], so the spectral mode density can vary from microsphere to microsphere. Secondly, it is hard to find one mode with very high quality factor and another mode with very low quality factor because the microsphere has only one surface contact with respect to the environment. Therefore, the modes experience not much different losses. As a result, their quality factors are not much different. Lastly, it is hard to bring the two TE

and TM modes into the frequency coresonance state by compressing the microsphere since its stem makes axial compression difficult.

The hollow bottle resonator (HBR) [43] appears as the candidate to replace the microsphere for solving those problems. As in Fig. 52, the HBR was produced from a silica capillary tubing of diameter 320 μm. Before being used to make the HBR, the capillary tubing was internally etched with hydrofluoric acid (HF) for 180 min to reduce the wall thickness [29]. Then, the middle region of the capillary was immersed in 270^{o}C sulfuric acid (H_2SO_4) for 45 min so as to remove the external jacket of the capillary. The HBR was produced by placing the middle region of the capillary under a hydrogen/oxygen mini-torch and using the internal air pressure method. The HBR shown in Fig. 52 has a maximum outer diameter of 440 μm and wall thickness of 7 μm. Normally, in our lab, the bulge diameter ranges from 335 to 350 μm in order to show the greatest possibility of having high-Q (~10^8) and overcoupled WGMs.

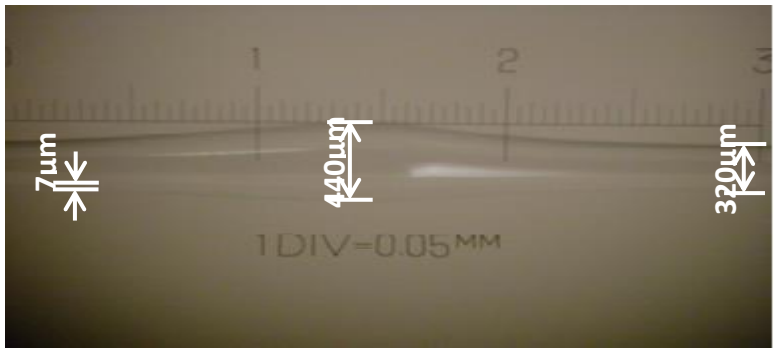

Figure 52. Hollow bottle resonator [42].

The first advantage of the HBR over the microsphere is the ease to find one very high Q mode and one very low Q mode as desired for the experiments. By thinning the wall thickness of the HBR down to 7 μm, the higher radial order WGMs will experience

more absorption or scattering through interaction with the inner surface of the HBR. More loss will result in lower *Q* modes.

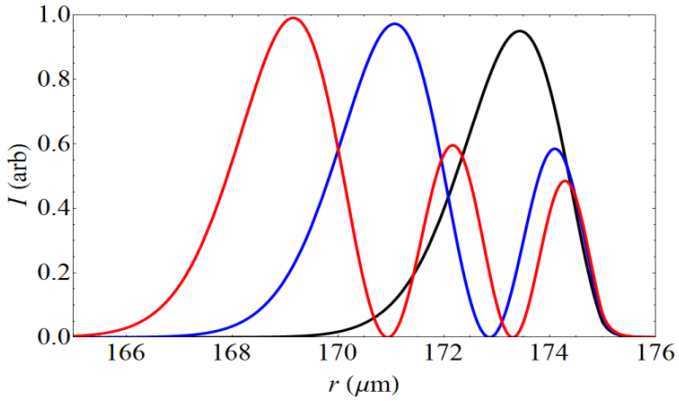

Figure 53. Radial mode intensity profile. First three radial orders for a 175-μm radius solid resonator at a wavelength of 1550 nm. First order (p = 1), black curve, one peak. Second order (p = 2), blue curve, two peaks. Third order (p = 3), red curve, three peaks.

Figure 53 shows the first three radial orders for a 175-μm radius solid resonator at a wavelength of 1550 nm. For our hollow resonator, the higher radial order modes ($p \geq 3$) are compressed between the wall surfaces. One can see that, when thinning the wall thickness of the HBR down to 7 μm, the low radial order mode intensity in black (p = 1) is confined by only the external surface and experiences less loss. This behavior of the mode allows it to keep the high quality factor. The higher radial order mode intensities in blue and red will also interact with the inner surface and experience more losses. Consequently, more losses will result in very low *Q* WGMs as in Fig. 54.

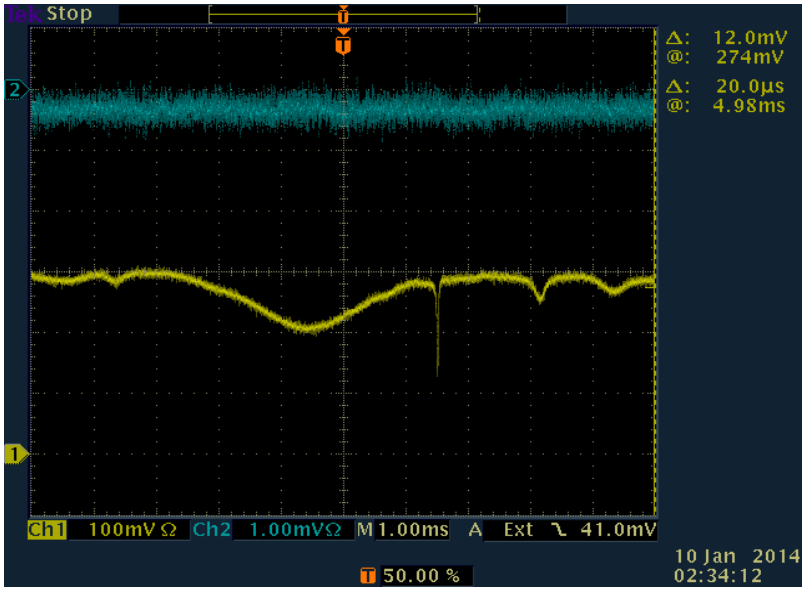

Figure 54. One very low *Q* and one very high *Q* modes (in yellow).

The second advantage of the HBR over the microsphere is the ease to bring two very different *Q* WGMs into the state of frequency coresonance by axial stretching of the HBR by means of applying a voltage to the PZT (piezoelectric transducer) as in Fig. 55 below.

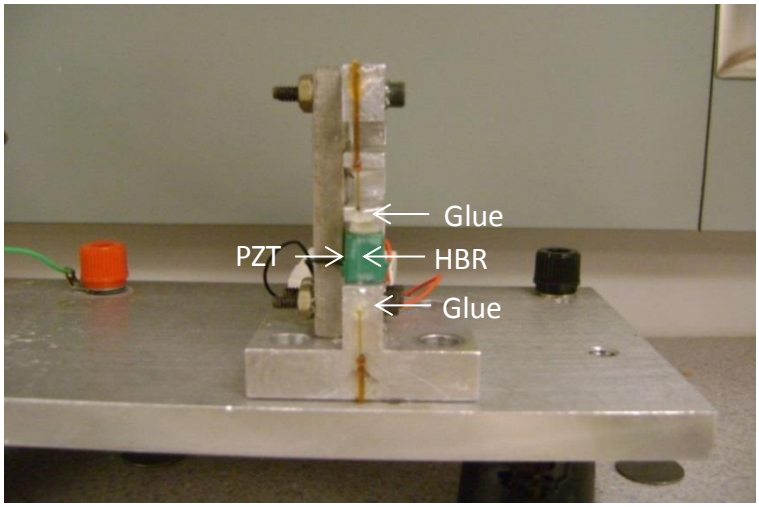

Figure 55. Axial stretching of HBR with PZT.

The HBR, (transparent part in the middle of the capillary in brown), was glued vertically on the upper and lower mounts of the PZT by using the 5 minute Epoxy (transparent dots). After 45 min, the HBR-PZT system was put in the acrylic box and the HBR was put in contact with the tapered fiber in its equatorial plane again. The PZT (in green) is then connected with the lock-in stabilizer (Lansing, Model number: 80.215) as shown in Fig. 56 in order to stretch the HBR with a voltage applied to the PZT. A voltage signal, including a bias and a modulation signal as shown in Fig. 57, that controls the HBR stretching, is sent from the lock-in stabilizer to the stretching tuner. The maximum bias signal output from the stabilizer is 1600 V. For the HBR experiment, the lock-in stabilizer voltage is set around 300-500 V. A capacitive voltage divider, whose circuit is shown in Fig. 58, is used to reduce the voltage to 150 V when the stabilizer is set at maximum bias. This reduced signal is applied to the PZT in the stretching tuner. The small voltage modulation is not used in this experiment. It has maximum 15 V_{pp} and is also reduced by the voltage divider before being sent to the PZT. When stretching the HBR, TE and TM modes will shift at different rates [37], and that condition is enough to bring TE and TM modes into the frequency coresonance state.

Figure 56. Lock-in stabilizer.

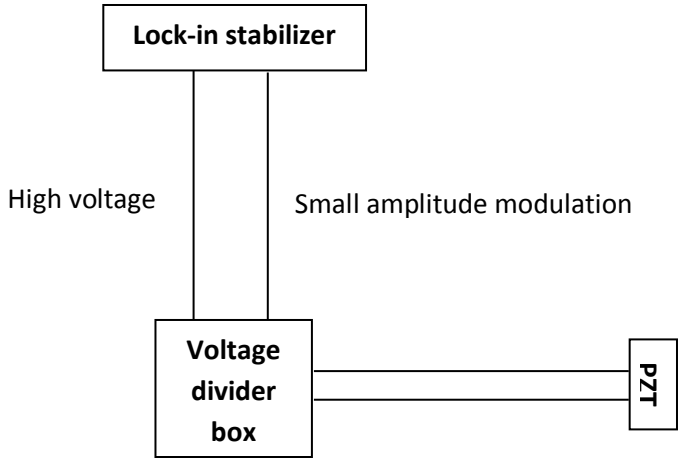

Figure 57. Capacitive voltage divider used to combine DC bias and modulation signal from the lock-in stabilizer for application to the PZT in the HBR stretcher.

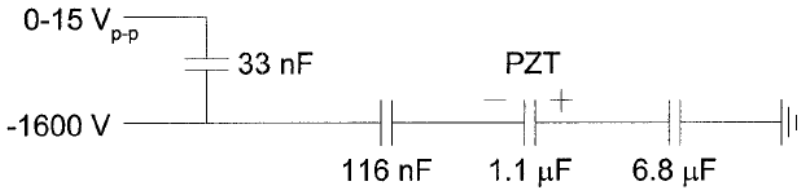

Figure 58. Capacitive voltage divider circuit [28].

The last advantage of the HBR over the microsphere is the rarer spectral mode density. Due to the gentle axial curvature of the bottle shape, the axial modes spread out along the axial direction, reducing the number of axial modes that can be simultaneously excited by tapered-fiber coupling. Furthermore, the mode spacing can be enhanced by working with the smaller diameter capillary tubing to increase the azimuthal free spectral range (FSR) of the modes since $\delta\nu = \frac{c}{2\pi na}$, where $\delta\nu$ is the FSR, n is the refractive index of the HBR medium, and a is the radius of the HBR. For CMIT/CMIA

experiments, only one polarization is driven at the input, but for CPIT/CPIA experiments, both TE and TM modes are excited simultaneously. Therefore, the spectral mode density reduction is especially important for coresonant polarization experiments. Using only one polarization, either TE or TM, for the input will reduce the spectral mode density of the throughput signal (as seen in Fig. 59), compared to the spectral mode density of the throughput power when the input has an arbitrary polarization (as seen in Fig. 60). Also, the diameter of the tapered coupling fiber and the HBR diameter are the principal determinants of the coupling regime and spectral mode density. In our experiment, the coupling tapered fiber of 2 μm in diameter and the HBRs with the diameters ranging from 330 μm to 440 μm showed the greatest possibility of having overcoupled WGMs and high quality factor ($Q \geq 10^7$).

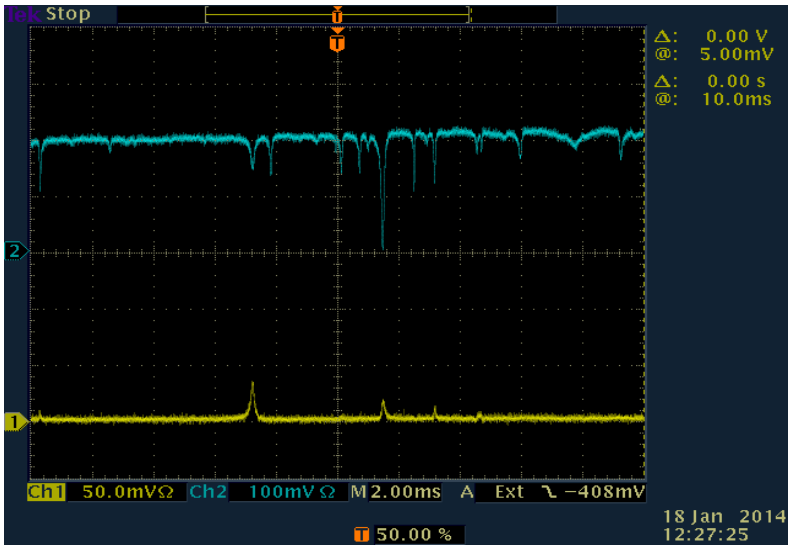

Figure 59. Throughput spectrum with a little CPC when input has TE polarization. TE throughput: blue , TM throughput: yellow.

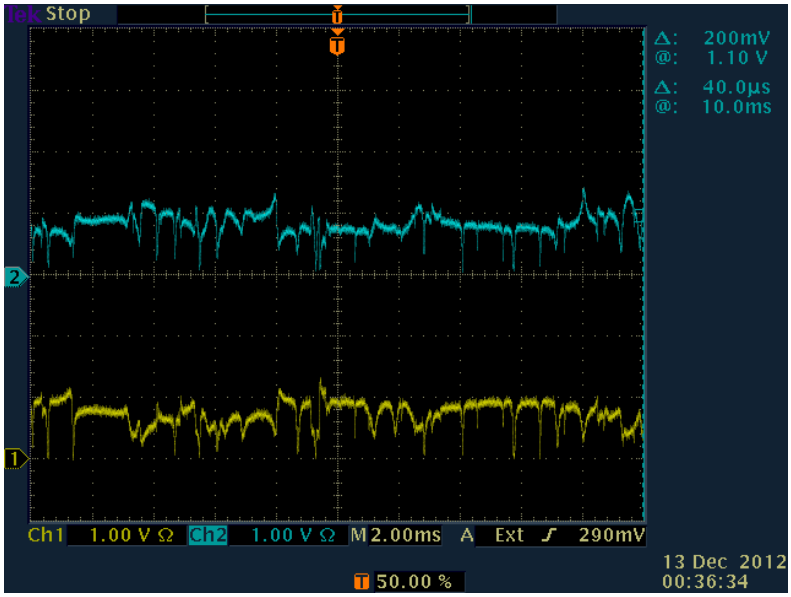

Figure 60. Throughput spectrum when the input polarization is linear at 45° and the polarization analyzer is set at 0° with respect to the HBR's basis. Dips in the blue (yellow) trace correspond to TE (TM) modes.

From the spectra shown in Figs. 59 and 60, it can be seen that the average spacing between modes of a given polarization is roughly 15 MHz. Since this is only about five times the average mode width, and the modes are essentially randomly distributed in frequency, mode overlap will not be a rare occurrence. Mode overlap can affect the experimental results and their fit to the model in a number of ways. It can change the apparent width and/or depth of a mode of interest, resulting in incorrect values of Q and/or M for that WGM. Overlap can change the IT/ATS/IA throughput shape, and result in input and throughput pulses not being measured at the correct positions, off and on resonance, respectively. All of these effects can degrade the experiment-model fit.

Each HBR WGM is characterized by three quantum numbers (m,p,q), where m (m = 1,2,..) gives the number of wavelengths around the circumference, p (p = 1,2,..) gives the number of power maxima along the radius, and q (q = 0,1,2,..) gives the number of

field nodes along the axis of the microresonator. The resonant wavelength for each (m,p,q) mode is given by [43]: $\lambda_{mpq} = 2\pi n\left[\left(\frac{U_{mp}}{R_b}\right)^2 + \left(q+\frac{1}{2}\right)\Delta E_m\right]^{-\frac{1}{2}}$, (41)

where $U_{mp} = m + \alpha_p(\frac{m}{2})^{\frac{1}{3}} \approx m$, α_p is the p^{th} root of the Airy function, $\Delta E_m = \frac{2U_{mp}\Delta k}{R_b}$, and R_b is the HBR bulge radius. The radius of the HBR as a function of axial position (as seen in Fig. 61) is given by:

$$R(z) = \frac{R_b}{\sqrt{1+(\Delta k z)^2}}, \quad (42)$$

where Δk is the inverse of the square root of the product of the effective axial radius R_p and the equatorial (bulge) radius R_b as in Fig. 61.

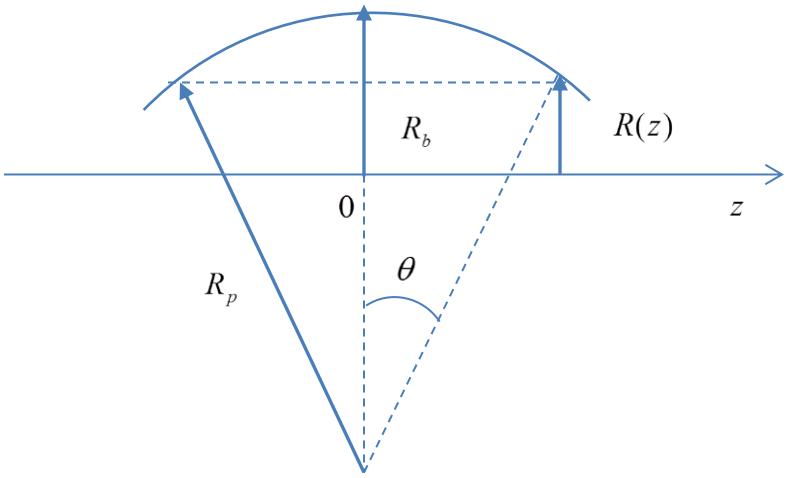

Figure 61. Radius profile of the HBR.

The axial extent of each mode is defined by the corresponding turning point, analogous to the turning point of the simple harmonic oscillator, and is given by:

$$z_c = \pm\left[\frac{4}{\Delta E_m}(q+\frac{1}{2})\right]^{-\frac{1}{2}}. \tag{43}$$

This value is measured from the bottle center; beyond this point the mode decays exponentially.

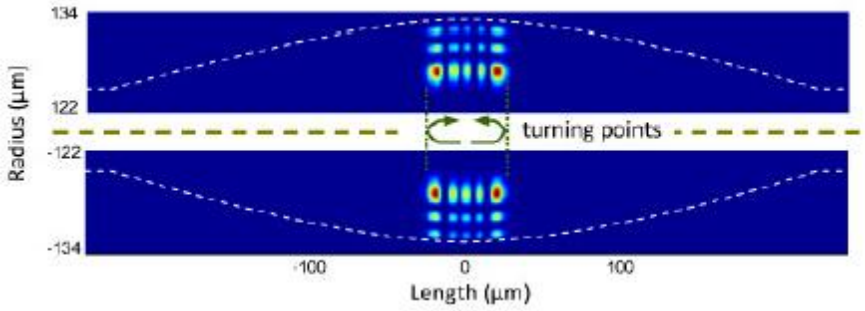

Figure 62. Intensity distribution along the length of the HBR [43].

Figure 62 exhibits the intensity distribution along the length of a HBR for a mode with p = 3 and q = 4. In the radial direction inward from the HBR surface, the mode intensity increases from the first radial peak to the third, as seen in the red curve in Fig. 53. In the axial direction, the mode peak intensity increases outward to the turning points, like the harmonic oscillator probability distribution. Beyond the turning points, the mode decays and we cannot observe the intensity [43].

Due to its bottle shape, the HBR has some advantages over the microsphere for controlling the cross polarization coupling. Offsetting the coupling fiber in the axial direction from the center of the HBR increases the chance to excite higher axial order

modes, similar to the excitation the higher order wave functions of the harmonic oscillator. By varying the position of the coupling fiber along the axial direction, we can have some control over the cross polarization coupling between TE and TM modes, through the potential variation of spatial mode overlap.

IV.5.1. CMIT and pulse delay with HBR

Given the benefits of the HBR over the microsphere, the HBR is now used for CMIT/CMIA experiments. The procedure to produce the CMIT throughput signal and the pulse picture is almost the same as the one used with the microsphere. The difference is that the diameter of the HBR is now approximately 340 μm and the alignment of the PA is now with the HBR basis. In order to measure the widths, dip depths and coupling regimes of the TE and TM modes without CPC, we detune them from coresonance by stretching the HBR. The widths and dip depths of the detuned modes can be measured directly by using the slow detector. The coupling regimes of the two detuned modes are determined by putting a segment of another tapered fiber in contact with the HBR on the opposite side of the working tapered fiber. If the depth of the resonant dip becomes deeper, we have an overcoupled mode and if the depth of the resonant dip becomes shallower, we have an undercoupled mode. For this experiment, in order to get correct results, the quality factor *Q*, coupling regime and dip depth *M* of a mode (TM) were measured when the PA is at 0^o and that of the other mode (TE) are measured when the PA is rotated 90^o with respect to the vertical (TE) axis in order to ensure that both TE and TM mode parameters are measured by the slow detector.

To do the pulse experiment, we bring the detuned TE and TM modes back into the coresonant state by unstretching the HBR and change the input light back to linear at 0^o by rotating the half wave plate. At this time the CMIT throughput shape is restored. The FWHM of the Gaussian pulses can be adjusted from FG2 according to the linewidth of the higher-*Q* mode (230 ns in the case shown below in Fig. 63). The pulse delay can be determined by comparing the relative positions of the optical resonant Gaussian pulse with respect to the optical off resonant Gaussian pulse on the fast detector channel with the help of the electrical Gaussian pulse from FG2 (approximately 42 ns in Fig. 63).

Figure 63 shows some experimental results for the CMIT and pulse delay experiment with HBR. In this experiment, the TE mode has dip depth M_1 = 0.87 and quality factor $Q_1 = 4.75\times10^6$, and the TM mode has dip depth M_2 = 0.3 and quality factor $Q_2 = 1.0\times10^8$. Both TE and TM modes are undercoupled. The HBR diameter is measured to be equal to 345 μm and the scattering model is used to fit the experimental data in this case.

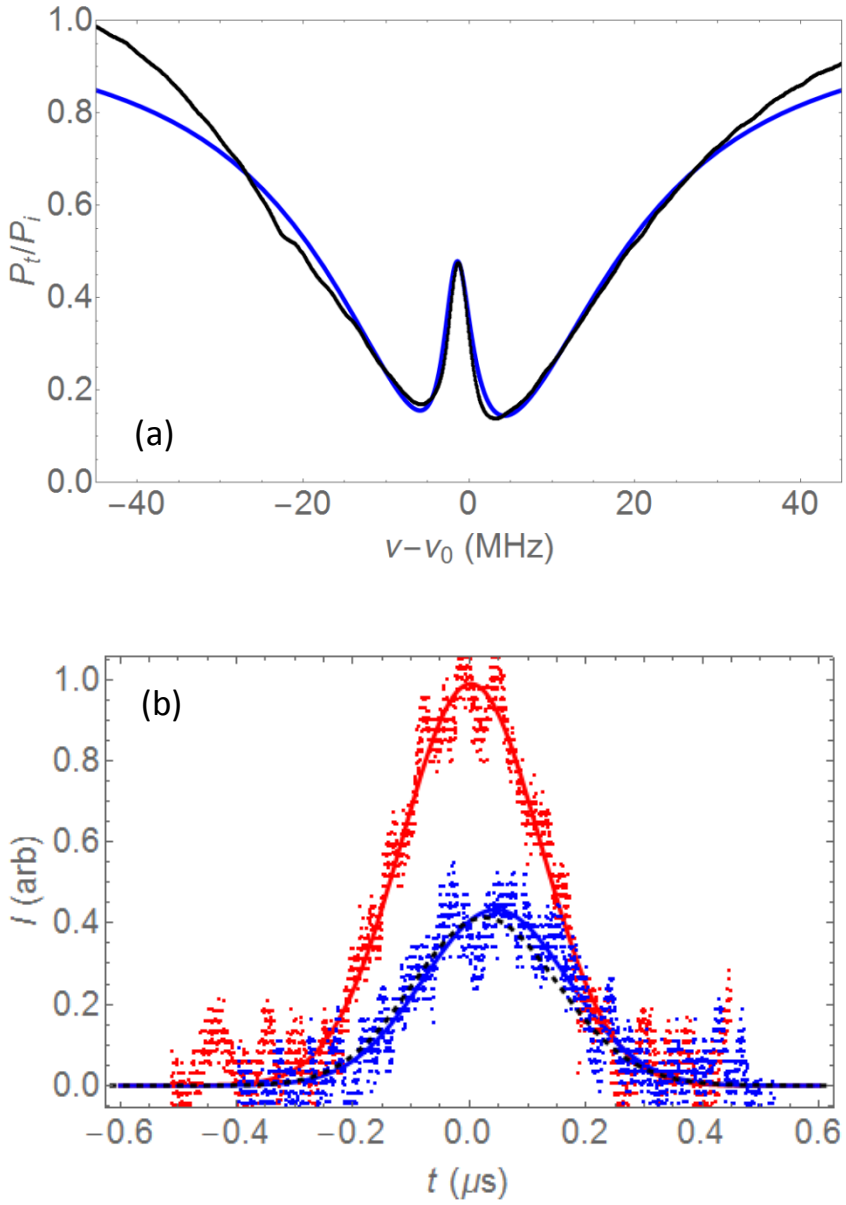

Figure 63. CMIT with 172-μm-radius HBR [42]. (a) Experimental (black) and model (blue) throughput spectra. (b) Experimental input (red) and throughput (blue) pulses, with an input pulse width of 275 ns and a delay of 42 ns, and model throughput pulse (dashed black), with a delay of 40 ns. Parameter values: M_1 = 0.87 (undercoupled), M_2 = 0.3 (undercoupled), Q_1 = 4.75×10^6, Q_2 = 1×10^8; offset = -1.5 MHz, T_s = 2.24×10^{-8}, pulse detuning = -1.5 MHz.

In Fig. 63, the fitting is quite reasonable. The width of the transparency window is somewhat greater than the width of mode 2 in this case. $T_s < T_{critical} = 9.9\times10^{-8}$ indicates that the throughput signal has CMIT shape. This is accounted for by the destructive interference between the direct and indirect excitation paths of TE modes. Although both modes are not strongly overcoupled as assumed in Eq. (36), but the conditions $T_s > \frac{T_1 T_2}{4}$ and $\frac{T_1 T_2}{4} > \frac{T_2^2}{4}$ hold, the dispersion slope is positive and there will be pulse delay. The relatively clean throughput trace indicates little interference with other WGMs, and as a result the predicted delay is nearly the same as the measured delay. The experimental delay-bandwidth product value is calculated to be 0.067 in this case.

When the quality factors of TE and TM modes are not hugely different and the cross coupling probability is approximately equal to the critical value, the Fano interference between the direct and indirect excitation paths of TE modes and coupling between TE and TM modes produces the CMIT signal, and the splitting is not much greater than the linewidths of the split modes as in Fig. 64 below. For this experiment, the HBR diameter is measured to be equal to 350 μm and the scattering model is used.

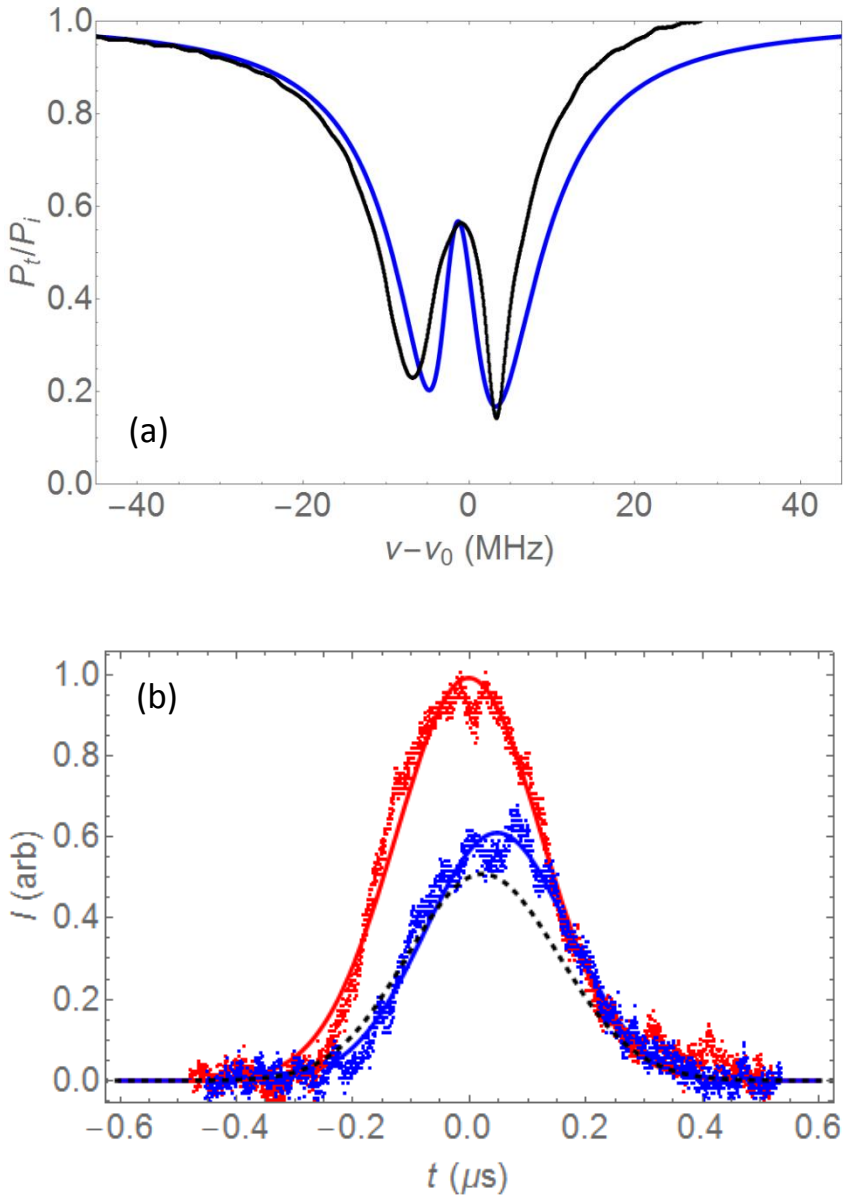

Figure 64. CMIT with 175-μm-radius HBR [42]. (a) Experimental (black) and model (blue) throughput spectra. (b) Experimental input (red) and throughput (blue) pulses, with an input pulse width of 290 ns and a delay of 50 ns, and model throughput pulse (dashed black), with a delay of 25 ns. Parameter values: M_1 = 0.865 (undercoupled), M_2 = 0.42 (overcoupled), Q_1 = 1.1×10^7, Q_2 = 9.5×10^7; offset = -1.5 MHz, T_s = 1.51×10^{-8}, pulse detuning = -1.3 MHz.

In part (a) of Fig. 64, the experimental data is different from the theoretical model for the throughput power fitting showing that there is some overlap of the nearby modes that lead to a disagreement between the theoretical calculation and experimental data for the pulse response picture in part (b). Since the experimental resonant throughput pulse is somewhat higher than the theoretical resonant throughput pulse, the off resonant pulse might not be truly far off resonant. That the cross polarization coupling strength $T_s < T_{critical} = 1.66 \times 10^{-8}$ indicates that the throughput signal has CMIT shape. Although both modes are not strongly overcoupled as assumed by Eq. (36), but the conditions $T_s > \frac{T_1 T_2}{4}$ and $\frac{T_1 T_2}{4} > \frac{T_2^2}{4}$ hold, the dispersion slope is positive and pulse delay is expected. The experimental delay-bandwidth product value is calculated to be 0.076.

IV.5.2. ATS and pulse delay with HBR

When the quality factors of two modes are comparable and the intermode coupling between TE and TM modes is greater than the critical value, the throughput signal is clearly split into two dips. The splitting between the mode components is proportional to the intermodal coupling strength. For this experiment, the HBR diameter is measured to be equal to 340 μm and the scattering model is used.

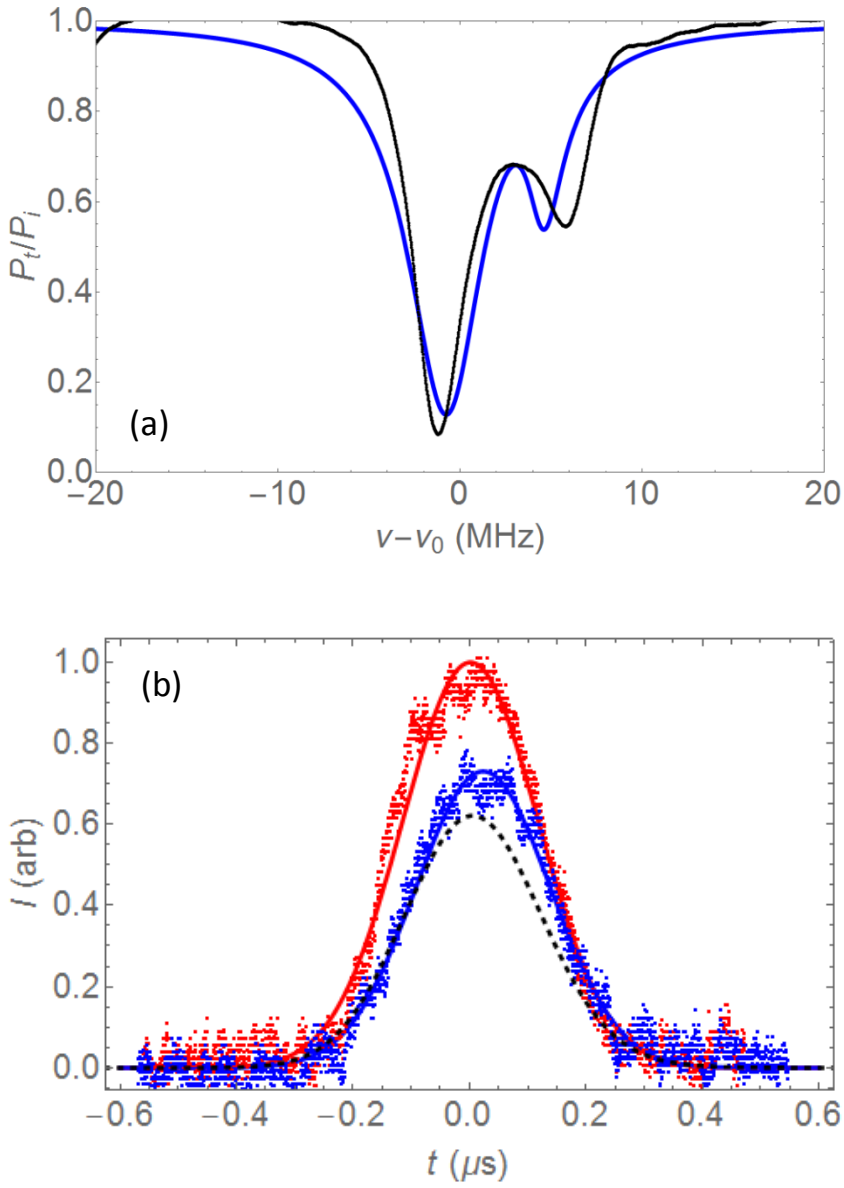

Figure 65. ATS with 170-μm-radius HBR [42]. (a) Experimental (black) and model (blue) throughput spectra. (b) Experimental input (red) and throughput (blue) pulses, with an input pulse width of 270 ns and a delay of 22 ns, and model throughput pulse (dashed black), with a delay of 10 ns. Parameter values: M_1 = 0.896 (undercoupled), M_2 = 0.62 (undercoupled), Q_1 = 3.5×10^7, Q_2 = 1×10^8; offset = 3.8 MHz, T_s = 3.55×10^{-9}, pulse detuning = 3.4 MHz.

In part (a) of Fig. 65, the experimental data is somewhat different from the theoretical model showing that there is some overlap of the nearby modes and that leads to a little disagreement between the theoretical calculation and experimental data for the throughput pulse response picture in part (b). Since the experimental resonant throughput pulse is somewhat higher than the theoretical resonant throughput pulse, the off resonant pulse might not be truly far off resonant. That the cross polarization coupling strength $T_s > T_{critical} = 8.56 \times 10^{-10}$ indicates that the throughput signal has ATS shape. Although both modes are not strongly overcoupled as assumed in Eq. (36), but the conditions $T_s > \frac{T_1 T_2}{4}$ and $\frac{T_1 T_2}{4} > \frac{T_2^2}{4}$ hold, the dispersion slope is positive and there will be pulse delay. The experimental delay-bandwidth product value is calculated to be 0.036.

IV.5.3. CMIA and pulse advancement with HBR

Analogous to CMIA with microsphere, when the coupling between TE and TM modes produces a deep dip in the throughput power, we have coupled mode induced absorption with HBR. The throughput shape and the pulse response pictures are shown in Fig. 66 below. For this experiment, the HBR diameter is measured to be equal to 350 μm and the scattering model is used.

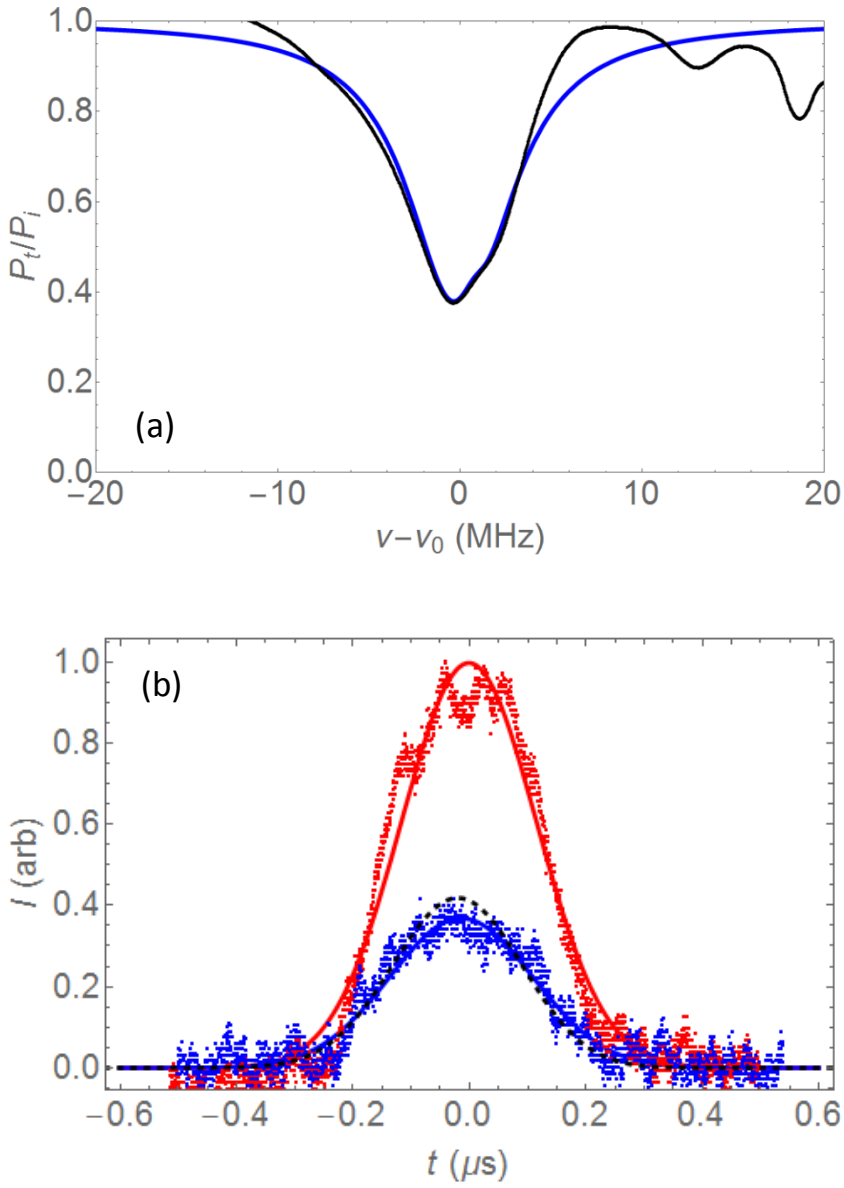

Figure 66. CMIA with 175-μm-radius HBR. (a) Experimental (black) and model (blue) throughput spectra. (b) Experimental input (red) and throughput (blue) pulses, with an input pulse width of 270 ns and an advancement of 13 ns, and model throughput pulse (dashed black), with an advancement of 12 ns. Parameter values: M_1 = 0.642 (undercoupled), M_2 = 0.97 (overcoupled), Q_1 = 2.9×10^7, Q_2 = 9.3×10^7; offset = 0.9 MHz, T_s = 3.98×10^{-10}, pulse detuning = -0.2 MHz.

In part (a) of Fig. 66, the throughput fitting is reasonable. Although both modes are not strongly overcoupled, but condition $\frac{T_2^2}{4} < T_s < \frac{T_1 T_2}{4}$ holds, the dispersion slope is negative and there will be pulse advancement as seen in part (b). As a result, the predicted advancement is nearly the same as the measured advancement. The experimental advancement-bandwidth product value is calculated to be 0.021.

In some cases, although with the CMIA throughput we can produce the pulse advancement, but both modes are not strongly overcoupled, as assumed in Eq. (36), so T_s is out of the negative group delay range. This phenomenon is again repeated in the experiment with the HBR whose diameter is measured to be equal to 340 μm as in Fig. 67 below and the scattering model is used to fit the data.

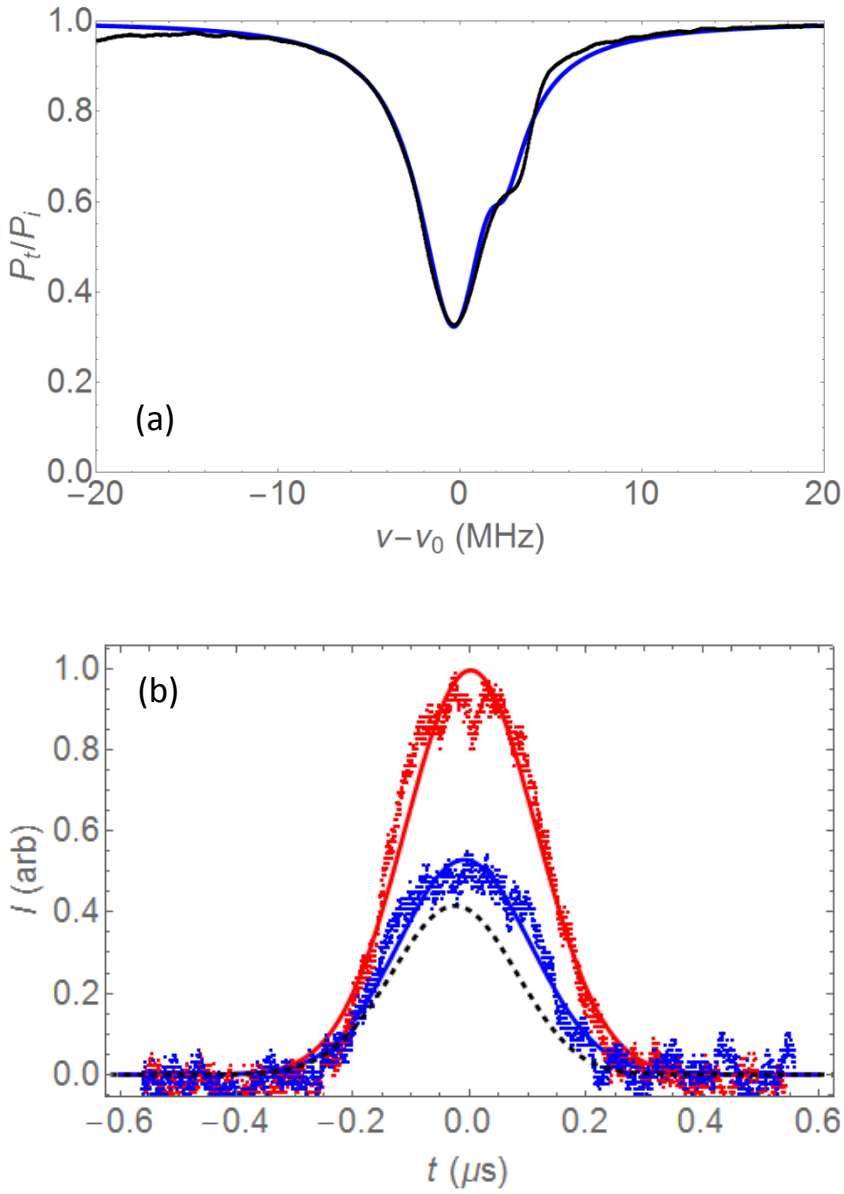

Figure 67. CMIA with 170-μm-radius HBR. (a) Experimental (black) and model (blue) throughput spectra. (b) Experimental input (red) and throughput (blue) pulses, with an input pulse width of 265 ns and an advancement of 11 ns, and model throughput pulse (dashed black), with an advancement of 20 ns. Parameter values: M_1 = 0.7 (undercoupled), M_2 = 0.68 (overcoupled), Q_1 = 4×10^7, Q_2 = 1×10^8; offset = 2 MHz, T_s = 7.94×10^{-10}, pulse detuning = -0.8 MHz.

In this case, the experimental advancement-bandwidth product is calculated to be 0.018.

IV.5.4. CMIA and pulse delay with HBR

Again, we can produce pulse delay with CMIA when working with HBR. For this experiment, the HBR diameter is measured to be equal to 345 μm and the scattering model is used. The throughput spectrum and pulse responses are shown in Fig. 68.

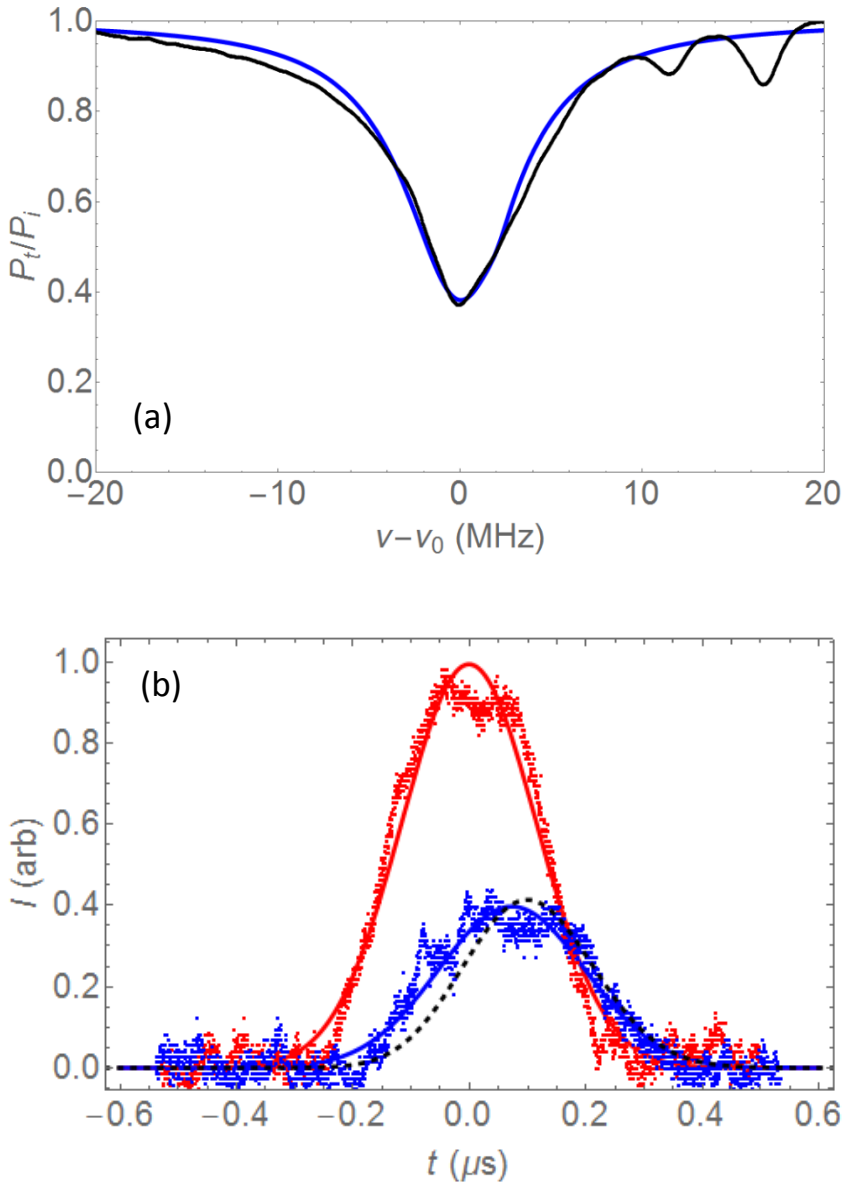

Figure 68. CMIA with 172-μm-radius HBR. (a) Experimental (black) and model (blue) throughput spectra. (b) Experimental input (red) and throughput (blue) pulses, with an input pulse width of 265 ns and a delay of 73 ns, and model throughput pulse (dashed black), with a delay of 80 ns. Parameter values: M_1 = 0.61 (overcoupled), M_2 = 0.83 (overcoupled), Q_1 = 2.6×10^7, Q_2 = 1×10^8; offset = 2 MHz, T_s = 7.94×10^{-11}, pulse detuning = 0.3 MHz.

In Fig. 68, the throughput fitting is reasonable. Because $T_s < \frac{T_2^2}{4}$ and $\frac{T_2^2}{4} < \frac{T_1 T_2}{4}$, we have a positive dispersion slope and pulse delay is expected. The experimental delay time is in good agreement with the theoretical calculation. The experimental delay-bandwidth product is calculated to be 0.12.

In some cases, we can produce a much larger pulse delay with CMIA when working with HBR, and the results are shown in Fig. 69 for an experiment with the HBR whose diameter is measured again to be equal to 345 μm; the scattering model is used again in this case.

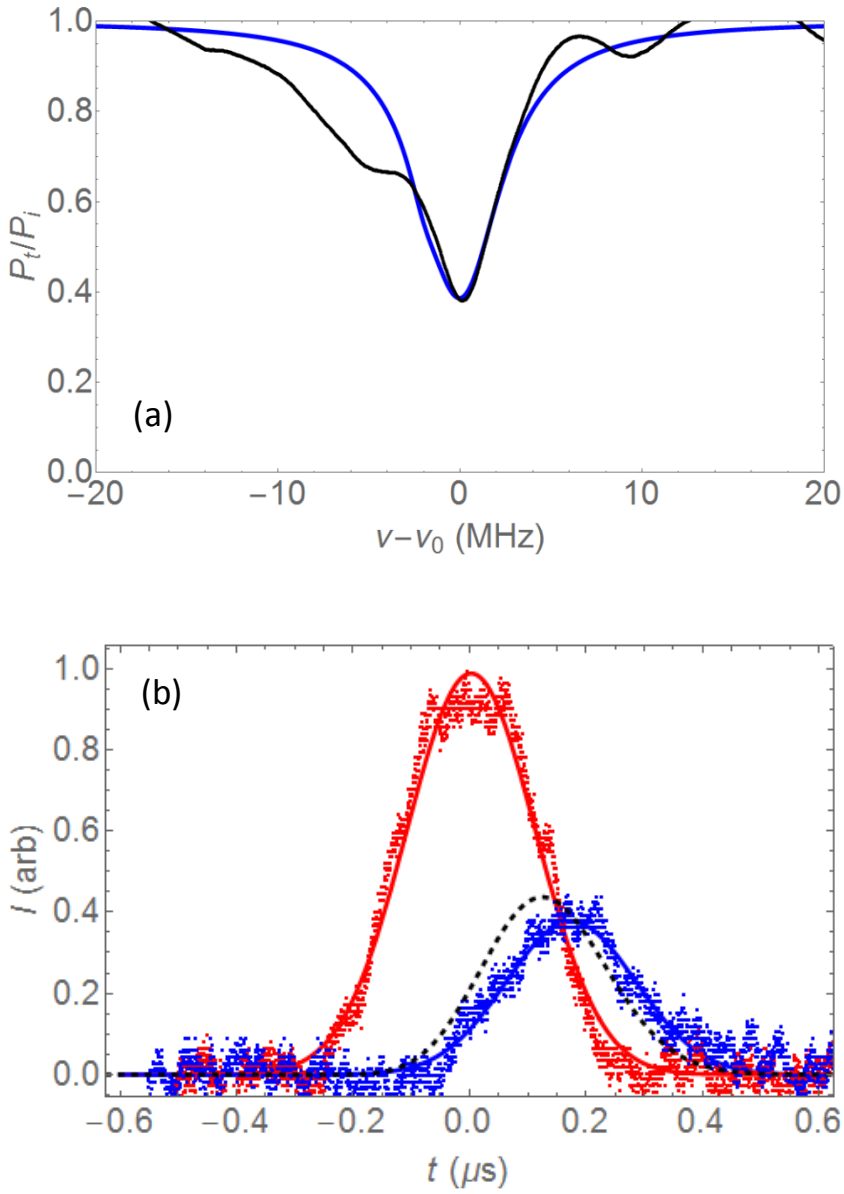

Figure 69. CMIA with 172-μm-radius HBR. (a) Experimental (black) and model (blue) throughput spectra. (b) Experimental input (red) and throughput (blue) pulses, with an input pulse width of 260 ns and a delay of 170 ns, and model throughput pulse (dashed black), with a delay of 140 ns. Parameter values: M_1 = 0.6 (overcoupled), M_2 = 0.9 (overcoupled), Q_1 = 3.5×10^7, Q_2 = 1×10^8; offset = -2 MHz, T_s = 10^{-10}, pulse detuning = 0 MHz.

In Fig. 69, there is some disagreement between the experimental throughput spectrum and the model meaning that there is some overlap of the nearby modes that affects the mode of interest and the pulse response. Because $T_s < \frac{T_2^2}{4}$ and $\frac{T_2^2}{4} < \frac{T_1 T_2}{4}$, we have a positive dispersion slope and pulse delay is expected. The experimental delay time is a little greater than the theoretical calculation. The experimental delay-bandwidth product is calculated to be 0.29, which is a really good value compared with the former delay-bandwidth products of CRIT experiments [41].

CHAPTER V

CORESONANT POLARIZATION INDUCED TRANSPARENCY AND ABSORPTION

In this chapter, a new experimental method to produce induced transparency plus pulse delay and induced absorption plus pulse delay or advancement with either microsphere or HBR is presented, along with experimental results fitted with our model. Instead of driving one polarization (either TE or TM) at the input of an optical system as for the case of CMIT/CMIA, now we can excite the two simultaneously by having the input light linearly polarized at 45^{o} with respect to the TE-TM basis of the microresonator. When the detected throughput has the same polarization as the input, the superposition between the coresonant TE and TM modes can create the desired effects even in the absence of cross polarization coupling. These phenomena are referred to as coresonant polarization induced transparency and absorption (CPIT, CPIA).

V.1. Introduction to CPIT and CPIA

From the previous sections we have already seen that the CMIT feature in the throughput power results from the cross-polarization coupling of TE and TM modes. However, in the CPIT process, what we see results from the superposition of two uncoupled coresonant TE and TM modes with very different quality factors and detecting only the throughput component polarized parallel to the input polarization.

If the polarization of the input E_f is linear at 45^o in the TE-TM basis, the components of the input in that basis are given by:

$$E_{f1} = \frac{E_f}{\sqrt{2}}, \tag{44}$$

$$E_{f2} = \frac{E_f}{\sqrt{2}}. \tag{45}$$

The intracavity fields for the case $r_s \to 1$ and $t_s \to 0$ (no cross polarization coupling) are given by:

$$E_{s1} = \frac{it_1 \exp\{-\frac{\alpha_1 L}{2} + i\delta_1\} E_{f1}}{1 - r_1 \exp\{-\frac{\alpha_1 L}{2} + i\delta_1\}}, \tag{46}$$

$$E_{s2} = \frac{it_2 \exp\{-\frac{\alpha_2 L}{2} + i\delta_2\} E_{f2}}{1 - r_2 \exp\{-\frac{\alpha_2 L}{2} + i\delta_2\}}. \tag{47}$$

The throughput components in the TE-TM basis are given by Eqs. (10) and (11), so the component of the throughput polarized at 45° would be given by:

$$E_{a1} = \frac{1}{\sqrt{2}}(E_{r1} + E_{r2}) = \frac{E_f}{2}\left[\frac{r_1 - \exp(-\alpha_1 L/2 + i\delta_1)}{1 - r_1 \exp(-\alpha_1 L/2 + i\delta_1)} + \frac{r_2 - \exp(-\alpha_2 L/2 + i\delta_2)}{1 - r_2 \exp(-\alpha_2 L/2 + i\delta_2)}\right]. \quad (48)$$

When $1 - r_k \approx \frac{T_k}{2} << 1$, $\alpha_k L << 1$, $\delta_k << 1$, giving $\exp(-\frac{\alpha_k L}{2}) \approx 1 - \frac{\alpha_k L}{2}$, and $\exp(i\delta_k) \approx 1 + i\delta_k$, $k = 1,2$, the 45° throughput field is written as:

$$E_{a1} = \frac{E_f}{2}\left[\frac{\frac{-T_1}{2} + \frac{\alpha_1 L}{2} - i\delta_1}{\frac{T_1}{2} + \frac{\alpha_1 L}{2} - i\delta_1} + \frac{\frac{-T_2}{2} + \frac{\alpha_2 L}{2} - i\delta_2}{\frac{T_2}{2} + \frac{\alpha_2 L}{2} - i\delta_2}\right]. \quad (49)$$

If the modes are coresonant and both are strongly overcoupled, so $T_k >> \alpha_k L$ and the difference in effective indices of refraction of two modes is small, i.e., $n_{1eff} \cong n_{2eff}$, so that $\delta_1 \approx \delta_2 = \delta$, Eq. (49) becomes:

$$E_{a1} = \frac{E_f}{2}\left[\frac{\frac{-T_1}{2} - i\delta}{\frac{T_1}{2} - i\delta} + \frac{\frac{-T_2}{2} - i\delta}{\frac{T_2}{2} - i\delta}\right]. \quad (50)$$

On resonance (δ = 0), we have E_{a1} = - E_f , so $|E_{a1}|^2 = |E_f|^2$ and we get 100% throughput. Far off resonance ($\delta >> T_1, T_2$), we have $E_{a1} = E_f$ and 100% throughput. Since $Q_2 >> Q_1$, it follows that $T_2 << T_1$. The TM (2) mode goes off resonance faster as δ increases since its resonance is sharper. Thus, the second term in square brackets in equation (50) goes from -1 to 1 while the first term is still ~ -1 and E_{a1} drops nearly to zero; therefore,

we have the coresonant polarization induced transparency throughput spectrum with the ideal calculated form shown in Fig. 25, or an actual example for the experiment with a microsphere, as shown in Fig. 70.

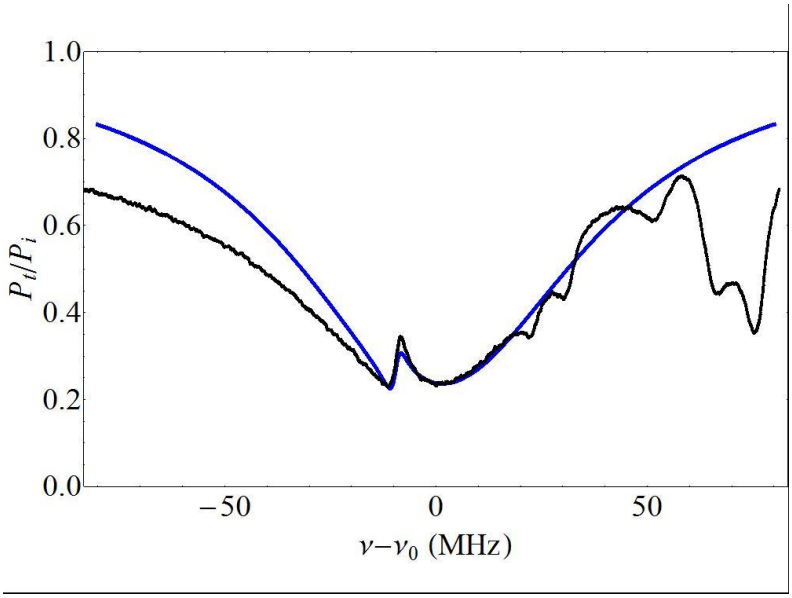

Figure 70. Data-model fitting of CPIT throughput spectrum; black dots: experimental data, blue curve: model fitting.

The data of Fig. 70 can then be overlaid by the model for fitting. Here, the blue curve is the computer model and the black curve is the experimental data trace. In order to fit the experimental data by the computer model, the quantities such as quality factors Q_1, Q_2, dip depths M_1, M_2, and coupling regimes of TE and TM modes, respectively are measured directly from the experiment and used as the inputs of the computer model. The CPC probability T_s, offset $\nu_2 - \nu_1$, and pulse center frequency detuning are used as fitting parameters. The offset and pulse detuning are known approximately from the experimental results, and their values are refined by the fitting process; T_s is a completely free parameter. After getting a good fit, the values of T_s, offset, and pulse detuning are determined from the computer model. In Fig. 70, agreement between the experimental

data and scattering computer model is shown for the case of -9.5 MHz offset of the TM resonance from the TE resonance. Both nearly coresonant modes are overcoupled and have the following parameters: TE has the quality factor Q_1 = 2.4×10^6 and fractional resonant dip depth M_1 = 0.982, and TM has the quality factor Q_2 = 6.5×10^7 and resonant dip depth M_2 = 0.235. The CPC probability T_s is determined from the fit to be equal to 1.26×10^{-8}.

In Fig. 70, we realized that on resonance the throughput is much less than 100%. This results from the fact that our modes are not strongly overcoupled, i.e., intrinsic loss can't be neglected. The right side of the throughput is not clean meaning that there is still some overlap of nearby modes, which needs to be cleaned by reducing spectral mode density.

From the theory and the preliminary result with CPIT above, both CPIT and CPIA production methods with the pulse responses are developed and presented in the next section for both microsphere and hollow bottle resonator.

V.2. Production of CPIT and CPIA with microsphere

For this experiment, all the initial setup for the equipment is the same as described in Chapter IV. The difference is the experimental procedure below.

To start the experiment, firstly the analyzer is rotated 45^o with respect to the vertical (~TE) axis. In this orientation, each detector (fast detector and slow detector) will display dips corresponding to both TE and TM modes. By rotating the polarization controller (PC) to make one type of mode disappear, the remaining mode is determined.

After that, the analyzer is rotated back to the direction of initial position. If the throughput power is rising on the fast detector channel and lowering on the slow detector channel on the oscilloscope screen, the excited modes are TE and on the contrary if the throughput power is lowering on the fast detector channel and rising on the slow detector channel, the excited modes are TM. For the case of excitation of modes of TE polarization, the 0^o position (corresponding to alignment of the analyzer basis with the microsphere basis) of the polarization analyzer is determined when the resonant throughput power measured from the fast detector is maximized and the resonant throughput power measured from the slow detector is minimized.

Next, the fiber is removed away until the resonant dips disappear. The analyzer is rotated again 45^o with respect to the vertical axis and the input polarization is changed to linear at 45^o by using the combination of the half-wave and quarter-wave plates. At this stage, the off resonant throughput power detected by the perpendicular detector (slow detector) is minimized (corresponding to 0.08 μW on channel A of the power meter) and the off resonant throughput power detected by the parallel detector (fast detector) is maximized on the oscilloscope screen. Next, the analyzer is rotated back to 0^o position, at this point the throughput powers measured from the fast detector and the slow detector are equal and the tapered fiber is placed back in contact with the microsphere for the subsequent steps. By searching for a coresonant TE and TM pair of modes of very different quality factors (the yellow and blue traces whose widths have been measured using the slow detector), we have the required modes for the experiment. The coupling regimes of the two coresonant modes are determined by putting a segment of another tapered fiber in contact with the microsphere on the opposite side of the working tapered

fiber. If the depth of the resonant dip becomes deeper, we have an overcoupled mode and if the depth of the resonant dip becomes shallower, we have an undercoupled mode. For this experiment, the quality factor *Q*, coupling regime and dip depth *M* of a coresonant mode (TM) were measured when the PA is at 0^o and that of the other coresonant mode (TE) are measured when the PA is rotated 90^o with respect to the vertical axis in order to ensure that both TE and TM mode parameters are measured by the slow detector. The CPIT feature of the throughput power can be recorded by the slow detector too by rotating the analyzer to the -45^o position.

To do the pulse experiment, the PA is then rotated back to the 45^o position with respect to the vertical axis so as to ensure that the CPIT feature is now recorded by the fast detector. Next, the connector from channel A of the power meter to the oscilloscope is unplugged and a BNC cable is then used instead to connect the oscilloscope with the second function generator FG2 in order to display the reference electrical Gaussian pulse directly from FG2. By switching the waveform to **Sequence** and varying the time scale down to 400 ns/div, the pulse picture of CPIT can be recorded for both resonance and off resonance cases. The FWHM of the electrical Gaussian pulses can be adjusted from FG2 according to the linewidth of the higher-*Q* mode (nominally 230 ns). In order to have the correct comparison between the theoretical calculation and the experimental data for the pulses, the width of the input pulse in the model has been chosen to be equal to the FWHM of the off resonant throughput optical Gaussian pulse (normally from 265 ns to 285 ns). Since the throughput optical pulses are noisy, we have to do a Gaussian fit for both off resonant and resonant throughput optical Gaussian pulses in order to determine the pulse width and delay exactly. By comparing the relative positions of the optical

resonant Gaussian pulse with respect to the optical off resonant Gaussian pulse on the fast detector channel, the experimental delay time is determined (27 ns in the first example shown below in Fig. 71). During this CPIT experiment process, the laser frequency is increasing from left to right on the oscilloscope screen (and in the figures). The TE mode has dip depth M_1 = 0.47 and quality factor Q_1 = 6.56×10^6, and the TM mode has dip depth M_2 = 0.92 and quality factor Q_2 = 8.8×10^7. Both TE and TM modes are overcoupled.

V.2.1. CPIT and pulse delay with microsphere

Here are some experimental results and the scattering model fitting from the CPIT experiment with microsphere described above, including throughput signal and pulse response. In this case, the microsphere radius is equal to 280 μm and the cross polarization coupling T_s has some nonzero value leading to a kind of hybrid result between CMIT and CPIT for the throughput signal. This hybridization is discussed in more detail in Chapter VI in the context of the two models, scattering and rotation.

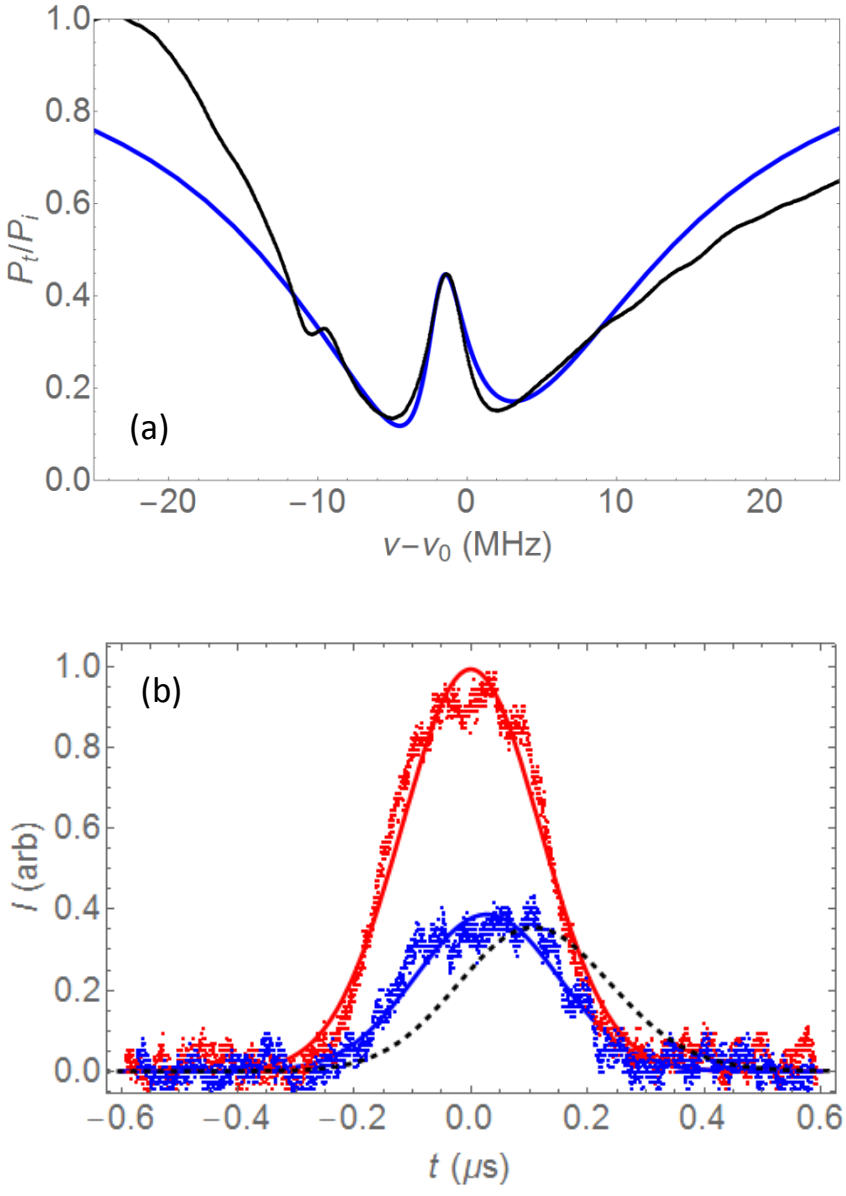

Figure 71. CPIT with 280-μm-radius microsphere. (a) Experimental (black) and model (blue) throughput spectra. (b) Experimental input (red) and throughput (blue) pulses, with an input pulse width of 280 ns and a delay of 27 ns, and model throughput pulse (dashed black), with a delay of 80 ns. Parameter values: M_1 = 0.47 (overcoupled), M_2 = 0.92 (overcoupled), Q_1 = 6.56×10^6, Q_2 = 8.8×10^7; offset = -1.8 MHz, T_s = 2×10^{-8}, pulse detuning = -1.6 MHz.

In part (a) of Fig. 71, the experimental data is a little different from the theoretical model in the throughput fitting, showing that there is some overlap of the nearby modes and that leads to a disagreement between the theoretical calculation and experimental data for the pulse response picture in part (b). Because $x_1 x_2 > 1$, pulse delay is expected. The experimental delay-bandwidth product value is calculated to be 0.043.

V.2.2. CPIA and pulse advancement with microsphere

Similar to CMIA, when the throughput has the shape of a deep dip, we have coresonant polarization induced absorption (CPIA), and this phenomenon results in the advancement of the incident resonant pulse. In this experiment, the microsphere radius is again equal to 280 μm and the scattering model is again used to fit the data.

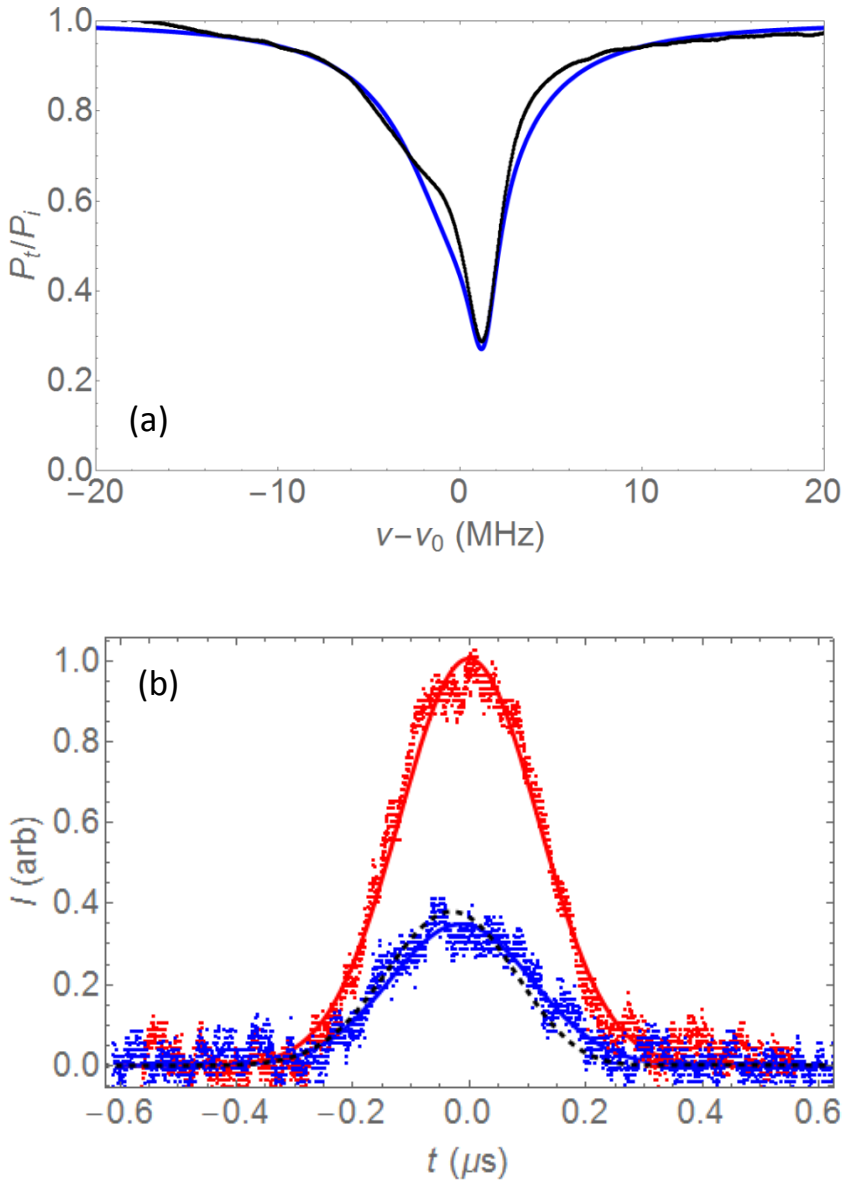

Figure 72. CPIA with 280-μm-radius microsphere. (a) Experimental (black) and model (blue) throughput spectra. (b) Experimental input (red) and throughput (blue) pulses, with an input pulse width of 280 ns and an advancement of 13 ns, and model throughput pulse (dashed black), with an advancement of 30 ns. Parameter values: M_1 = 0.78 (undercoupled), M_2 = 0.738 (undercoupled), Q_1 = 2.6×10^7, Q_2 = 1×10^8; offset = 1.3 MHz, T_s = 5×10^{-16}, pulse detuning = 0.9 MHz.

In part (a) of Fig. 72, the throughput fitting is reasonable. Because $x_1 x_2 < 1$, pulse advancement is expected. The value $T_s = 5 \times 10^{-16}$ means that cross polarization coupling is negligible. That the measured advancement is a little less than the predicted advancement in part (b) implies that the throughput pulse is not quite on resonance or the off-resonant pulse is not really off resonance. The experimental advancement-bandwidth product value is calculated to be 0.02 in this case.

V.2.3. CPIA and pulse delay with microsphere

Analogous to CMIA with microsphere, we can produce the pulse delay with CPIA when working with microsphere. All the experimental results and model calculation are shown in Fig. 73 below. In this case, the microsphere radius is equal to 290 μm and the rotational model is used to fit the experimental data.

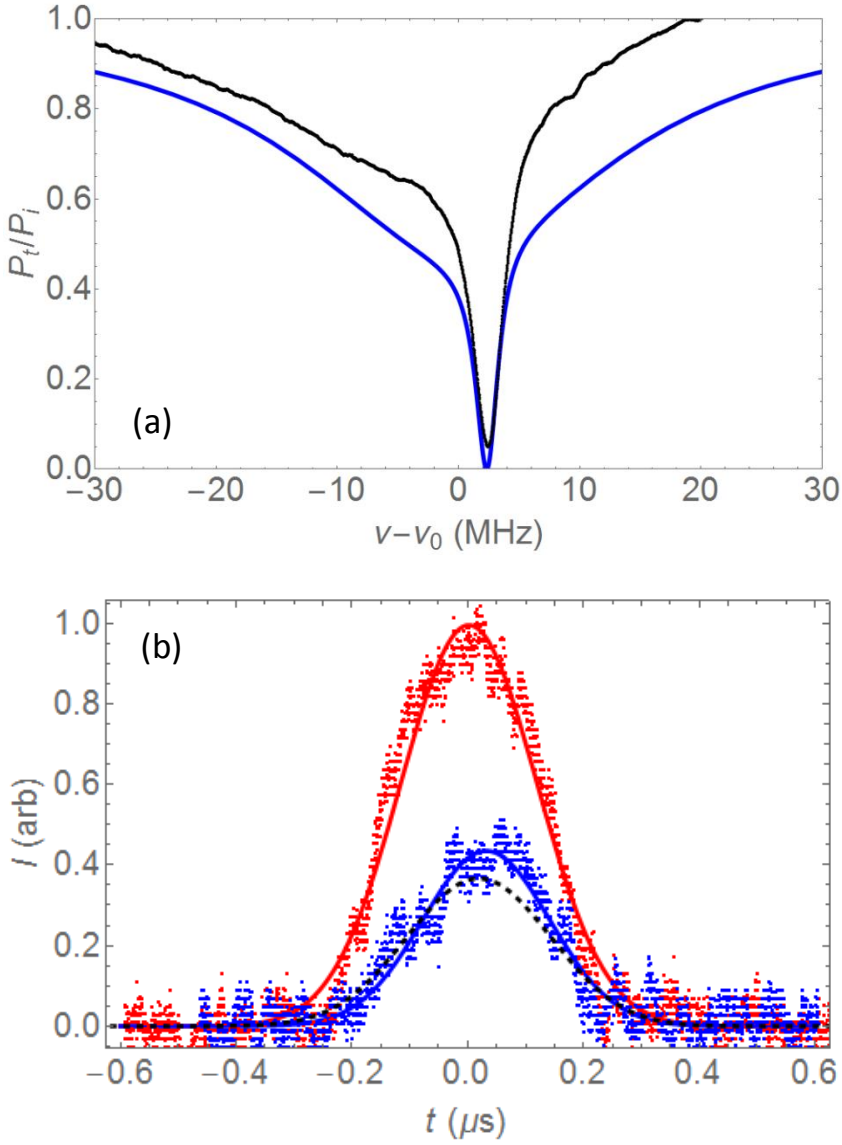

Figure 73. CPIA with 290-µm-radius microsphere. (a) Experimental (black) and model (blue) throughput spectra. (b) Experimental input (red) and throughput (blue) pulses, with an input pulse width of 275 ns and a delay of 30 ns, and model throughput pulse (dashed black), with a delay of 20 ns. Parameter values: M_1 = 0.87 (undercoupled), M_2 = 0.85 (overcoupled), Q_1 = 5.9×10^6, Q_2 = 8.6×10^7; offset = 2.4 MHz, T_s = 5×10^{-16}, pulse detuning = -0.3 MHz.

In Fig. 73, the experimental data is slightly different from the model calculation because mode overlap makes it difficult to determine the off resonance throughput level. Because $x_1 x_2 > 1$, we have positive group delay and pulse delay is expected. The experimental delay time agrees well with the theoretical calculation when the center frequency of the throughput pulse is detuned -0.3 MHz from the resonant frequency of the TE mode. If the center frequency of the throughput pulse is right below the bottom of the CPIA dip, the throughput pulse will be split. This phenomenon requires more time to do the experiment to get the desired observation, and this can be done in the near future. The value $T_s = 5 \times 10^{-16}$ means that cross polarization coupling is negligible. The experimental delay-bandwidth product is calculated to be 0.048.

When doing the CPIT/CPIA experiment with a microsphere, we again have the same problem as with the CMIT/CMIA experiment before, i.e., some overlap of the nearby modes that affect the mode of interest. As a result, it is hard to find two strongly over/undercoupled modes with very different quality factors for the experiment. So switching from the microsphere to the hollow bottle resonator is also necessary for the CPIT/CPIA experiment.

V.3. Production of CPIT and CPIA with hollow bottle resonator

The experimental setup to produce the CPIT/CPIA throughput signal and the pulse response with HBR is almost the same as CPIT/CPIA procedure used with microsphere. The difference is that, the diameter of the HBR is now approximately 340 μm, and the alignment of the PA is now with the HBR basis. The process to measure the dip depths, quality factors, and coupling regimes of TE and TM modes is the same as the one used in the CMIT/CMIA experiment with HBR before.

V.3.1. CPIT and pulse delay with HBR

Since the cross polarization coupling effect depends on spatial mode overlap, we can reduce CPC for the CPIT/CPIA experiment by offsetting the tapered fiber along the axial direction of the HBR to a position with negligible CPC. Here are some experimental results from the CPIT experiment with HBR and fitting the results using the scattering model, and they are shown in Fig. 74.

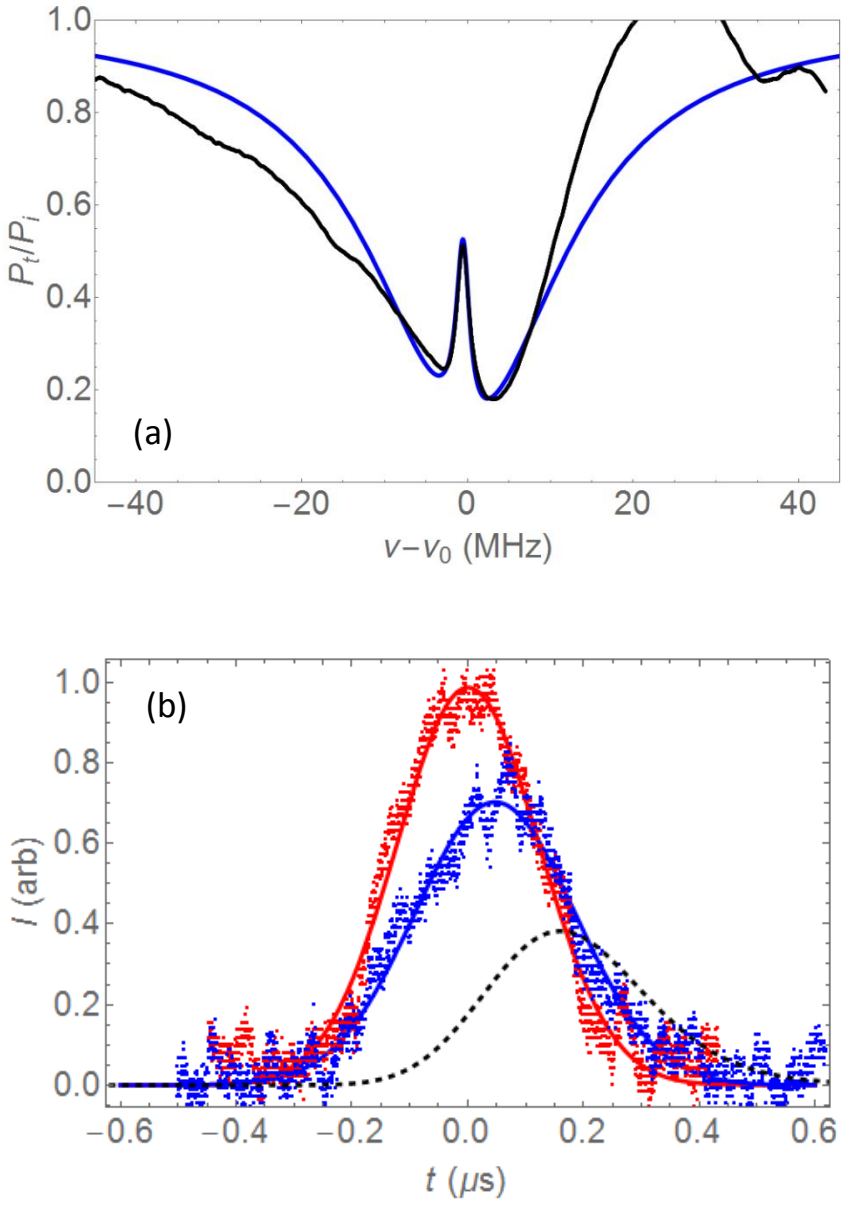

Figure 74. CPIT with 170-μm-radius HBR. (a) Experimental (black) and model (blue) throughput spectra. (b) Experimental input (red) and throughput (blue) pulses, with an input pulse width of 285 ns and a delay of 47 ns, and model throughput pulse (dashed black), with a delay of 150 ns. Parameter values: M_1 = 0.61 (overcoupled), M_2 = 0.32 (overcoupled), Q_1 = 6.9×10^6, Q_2 = 1×10^8; offset = -0.5 MHz, T_s = 5×10^{-16}, pulse detuning = -0.5 MHz.

In Fig. 74, the transparency window has approximately the same width as mode 2. Since both WGMs in Fig. 74 are overcoupled, $x_1 x_2 > 1$, so there is pulse delay. The measured delay is 47 ns, but the model delay is 150 ns. The experimental delay-bandwidth product is calculated to be 0.073. The disagreement probably comes from the fact that the off resonant throughput pulse (in red) is not far off resonant and experiences some delay. So the measured value is much less than the calculated value. Furthermore, the overlap of the nearby modes can affect the properties of the mode of interest.

V.3.2. CPIA and pulse advancement with HBR

Similar to microsphere, we can produce the pulse advancement when the throughput signal has the shape of a deep dip. All the results are shown in Fig. 75 below.

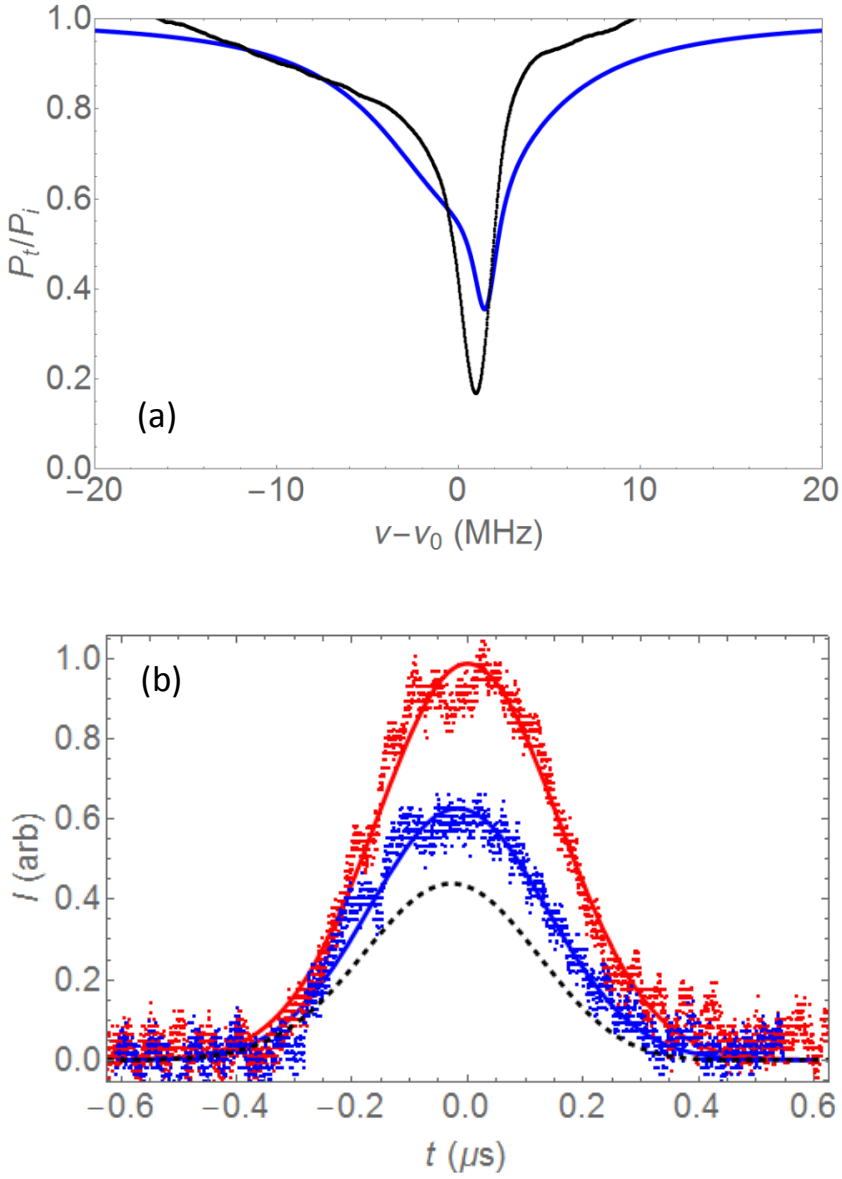

Figure 75. CPIA with 170-µm-radius HBR. (a) Experimental (black) and model (blue) throughput spectra. (b) Experimental input (red) and throughput (blue) pulses, with an input pulse width of 370 ns and an advancement of 17 ns, and model throughput pulse (dashed black), with an advancement of 25 ns. Parameter values: M_1 = 0.69 (undercoupled), M_2 = 0.64 (undercoupled), Q_1 = 1.8×10^7, Q_2 = 1.19×10^8; offset = 1.5 MHz, T_s = 5×10^{-16}, pulse detuning = 1.3 MHz.

In Fig. 75, both WGMs are undercoupled, $x_1 x_2 < 1$, so there is pulse advancement. That the experimental throughput pulse (in blue) is somewhat higher than the theoretical calculation (in dashed) means that the resonant pulse is not really on resonance or the off resonant pulse (in red) is not truly far off resonance. Since the higher-Q mode has $Q_2 = 1.19\times10^8$, we have to widen the pulse width Δt_o as in Section IV.2.1.3 in order to ensure that the whole pulse experiences the same steep dispersion for advancement. The experimental advancement-bandwidth product is calculated to be 0.02. The minor disagreement in the advancement time probably results from the presence of another WGM in the experimental throughput trace. In this experiment, the scattering model was used to fit the experimental data.

V.3.3. CPIA and pulse delay with HBR

Analogous to CPIA with microsphere, we can produce the pulse delay with CPIA when working with HBR. The experimental results and scattering model calculations are shown in Fig. 76.

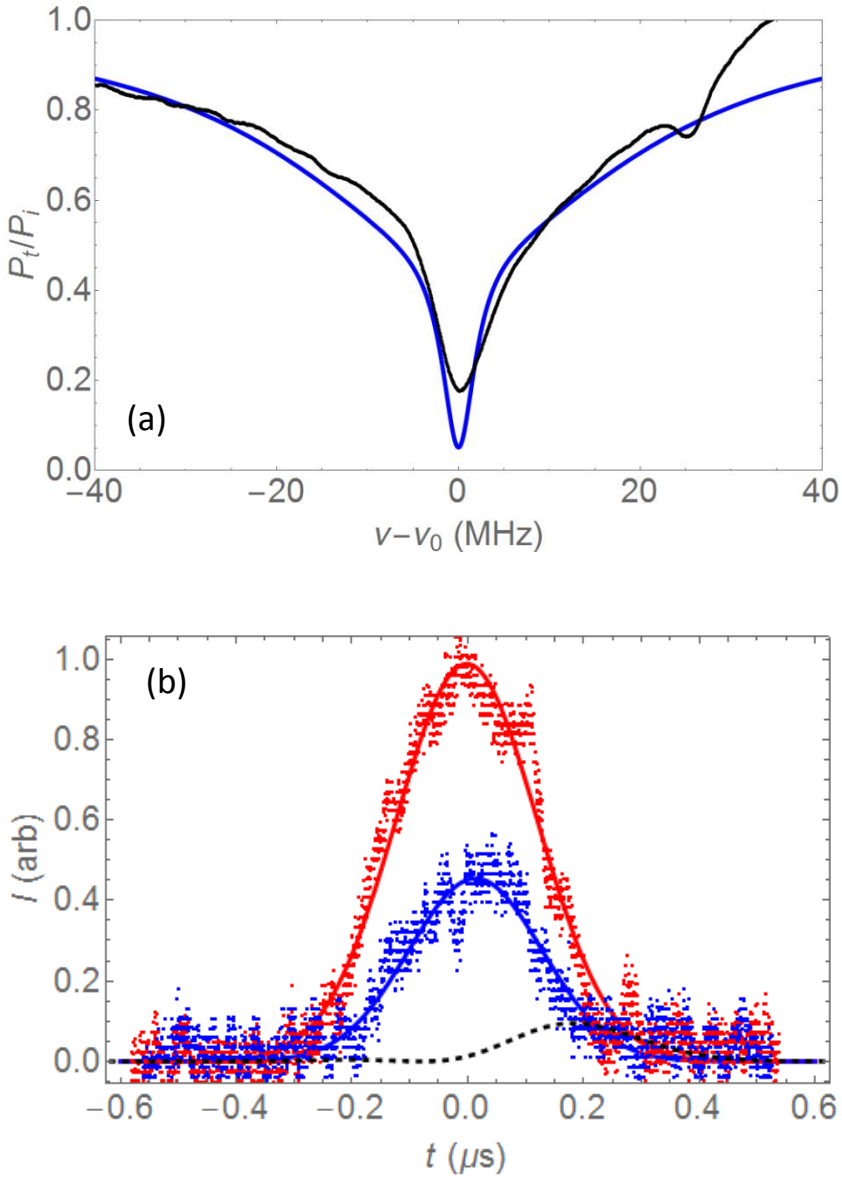

Figure 76. CPIA with 170-μm-radius HBR. (a) Experimental (black) and model (blue) throughput spectra. (b) Experimental input (red) and throughput (blue) pulses, with an input pulse width of 285 ns and a delay of 16 ns, and model throughput pulse (dashed black), with a delay of 160 ns. Parameter values: M_1 = 0.36 (overcoupled), M_2 = 0.88 (undercoupled), Q_1 = 4.4×10^7, Q_2 = 4.1×10^6; offset = 0 MHz, T_s = 5×10^{-16}, pulse detuning = 0 MHz.

In Fig. 76, the throughput fitting is rather good but there is still some overlap of the nearby modes with respect to the mode of interest, resulting in the offset of the resonant throughput pulse or the off-resonant throughput pulse not being truly off resonance, leading to the disagreement between the measured and theoretically calculated pulse response. The coupling regime product $x_1 x_2 > 1$, so there is pulse delay. The experimental delay-bandwidth product is calculated to be 0.025.

In another case, we can have a better agreement between the measured and theoretically calculated pulse delays when fitting with the rotational model (when there is no CPC and T_s = 0, the two models are equivalent, as described in detail in chapter VI). All the results are shown in Fig. 77.

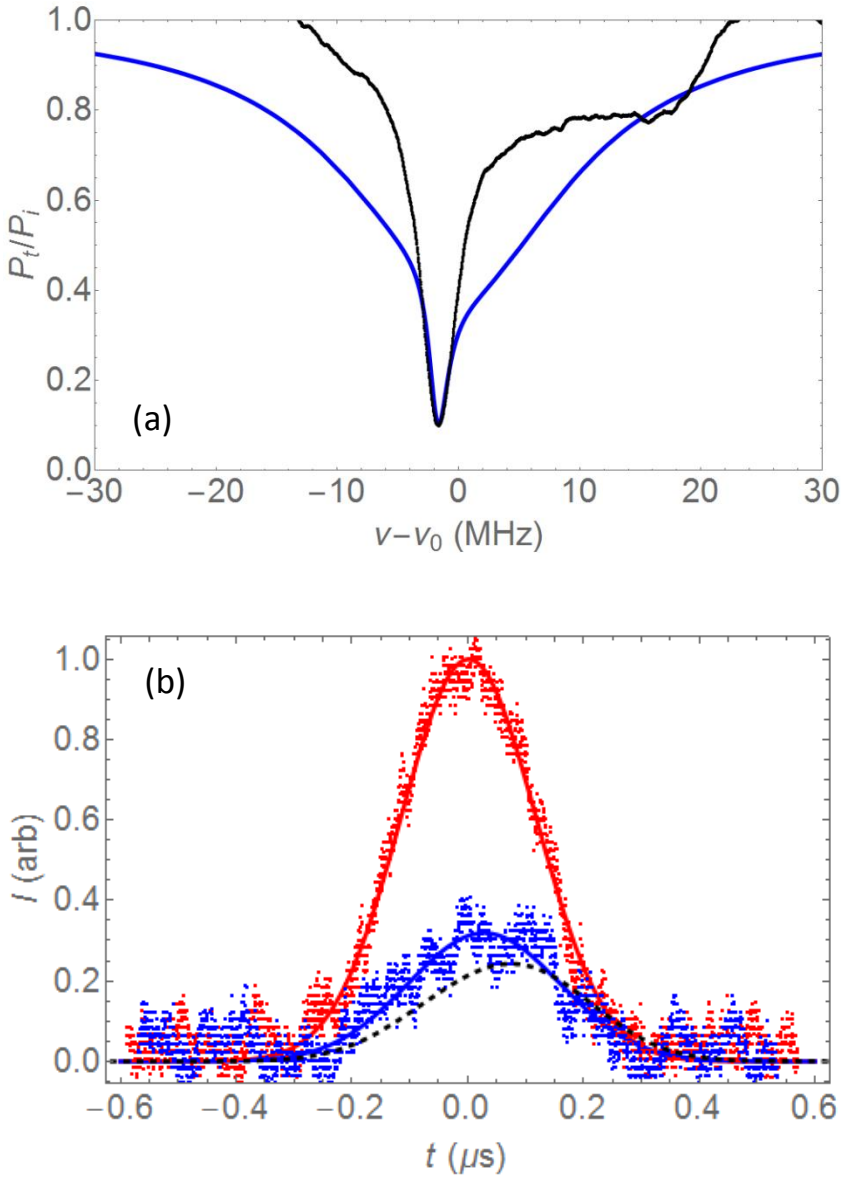

Figure 77. CPIA with 170-μm-radius HBR. (a) Experimental (black) and model (blue) throughput spectra. (b) Experimental input (red) and throughput (blue) pulses, with an input pulse width of 275 ns and a delay of 27 ns, and model throughput pulse (dashed black), with a delay of 70 ns. Parameter values: M_1 = 0.96 (undercoupled), M_2 = 0.23 (overcoupled), Q_1 = 8.4×10^6, Q_2 = 1×10^8; offset = -1.8 MHz, T_s = 5×10^{-16}, pulse detuning = 0 MHz.

In Fig. 77, $x_1 x_2 > 1$, so there is pulse delay. The experimental delay-bandwidth product is calculated to be 0.043.

CHAPTER VI

COMPARISON BETWEEN SCATTERING AND ROTATIONAL MODELS

In this chapter, we introduce a new model in which the cross polarization coupling effect is treated as polarization rotation, not scattering. The equivalence of the rotational and scattering models when used to explain the CPIT effect for the case of no coupling and the CMIT effect for the case of nonzero coupling is specified. The difference between the scattering model and the rotational model (for both forward and reverse orders of the input data in the rotational model, since it assumes a particular sense of rotation) when used to explain the CPIT effect for the case of nonzero cross polarization coupling is also mentioned. Comparison between experiment and model might allow us to determine which model better represents the physical CPC process; this is a first quantitative comparison of the two models. The rotational model is expected to be more realistic, because scattering would have to take place at a single point on the circumference and have a probability two orders of magnitude larger than backscattering. Also, previous experimental investigations [38, 39] seem to be more qualitatively consistent with the rotational model.

VI.1. Rotational model

The details for the scattering model were treated in Chapter III. Now we introduce the new model in which the cross polarization coupling is treated as polarization rotation. In the rotation model, the coupling matrix implicit in Eqs. (5) and (6) goes from $\begin{pmatrix} r_s & it_s \\ it_s & r_s \end{pmatrix}$ to $\begin{pmatrix} r_s & -t_s \\ t_s & r_s \end{pmatrix}$, as in Eqs. (51) and (52) below. As illustrated in Fig. 77, we assume that the polarization rotates clockwise in the TE-TM basis as the light propagates in the microresonator. Thus after a round trip, a TE field component generates a small positive TM component and a TM component generates a small negative TE component.

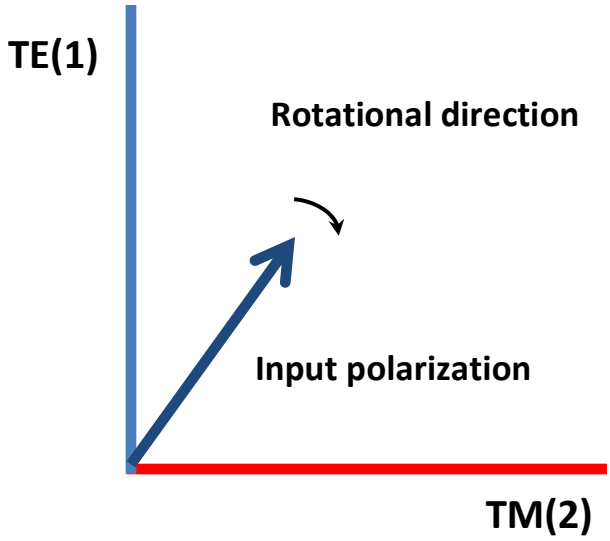

Figure 78. Polarization rotation in the TE-TM basis.

As before:

$$E_{r1} = r_1 E_{f1} + it_1 E_{s1},$$

$$E_{r2} = r_2 E_{f2} + it_2 E_{s2},$$

$$E_{c1} = it_1 E_{f1} + r_1 E_{s1},$$

$$E_{c2} = it_2 E_{f2} + r_2 E_{s2}.$$

Analogous to Eqs. (5) and (6), the intracavity fields can be calculated as:

$$E_{s1} = \exp\{-\frac{\alpha_1 L}{2} + i\delta_1\}(r_s E_{c1} - t_s E_{c2}), \tag{51}$$

$$E_{s2} = \exp\{-\frac{\alpha_2 L}{2} + i\delta_2\}(r_s E_{c2} + t_s E_{c1}). \tag{52}$$

Or:

$$E_{s1} = e_1(r_s E_{c1} - t_s E_{c2}),$$

$$E_{s2} = e_2(r_s E_{c2} + t_s E_{c1}).$$

Now:

$$E_{s1} = e_1\left[(it_1 r_s E_{f1} + r_1 r_s E_{s1}) - (it_2 t_s E_{f2} + r_2 t_s E_{s2})\right], \tag{53}$$

$$E_{s2} = e_2\left[(it_2 r_s E_{f2} + r_2 r_s E_{s2}) + (it_1 t_s E_{f1} + r_1 t_s E_{s1})\right]. \tag{54}$$

After a simple analysis, we end up with the intracavity TE and TM fields:

$$E_{s1} = \frac{E_{f1}}{D}\left[it_1 e_1(r_s - r_2 e_2)\right] - \frac{E_{f2}}{D}\left[it_2 t_s e_1\right], \tag{55}$$

$$E_{s2} = \frac{E_{f2}}{D}\left[it_2 e_2(r_s - r_1 e_1)\right] + \frac{E_{f1}}{D}\left[it_1 t_s e_2\right], \tag{56}$$

where:

$$D = 1 - r_1 r_s e_1 - r_2 r_s e_2 + r_1 r_2 e_1 e_2. \tag{57}$$

Similar to Eqs. (18) and (19), the intracavity fields can be written in terms of the input fields and intracavity fields one round trip earlier:

$$E_{s1} = a_1 E'_{f1} + b_1 E'_{f2} + c_1 E'_{s1} + d_1 E'_{s2},$$

$$E_{s2} = a_2 E'_{f2} + b_2 E'_{f1} + c_2 E'_{s2} + d_2 E'_{s1}.$$

Where: $a_1 = it_1 r_s e_1$, $b_1 = -it_2 t_s e_1$, $c_1 = r_1 r_s e_1$, $d_1 = -r_2 t_s e_1$, $a_2 = it_2 r_s e_2$, $b_2 = it_1 t_s e_2$, $c_2 = r_2 r_s e_2$, $d_2 = r_1 t_s e_2$.

Analogous to Eqs. (24) and (25), we have two differential equations for the intracavity fields:

$$\dot{E}_{s1} = -\gamma_1 E_{s1} - \frac{t_s}{\tau_{rt1}} E_{s2} + \frac{it_1}{\tau_{rt1}} E_{f1} - \frac{it_2 t_s}{\tau_{rt1}} E_{f2}, \tag{58}$$

$$\dot{E}_{s2} = -\gamma_2 E_{s2} + \frac{t_s}{\tau_{rt2}} E_{s1} + \frac{it_2}{\tau_{rt2}} E_{f2} + \frac{it_1 t_s}{\tau_{rt2}} E_{f1}. \tag{59}$$

Similarly, we have the first order differential equations for the throughput fields:

$$\dot{E}_{r1} = \dot{E}_{f1} - \gamma_1 (E_{r1} - r_1 E_{f1}) - \frac{t_s t_1}{t_2 \tau_{rt1}} (E_{r2} - r_2 E_{f2}) - \frac{t_1^2}{\tau_{rt1}} E_{f1} + \frac{t_1 t_2 t_s}{\tau_{rt1}} E_{f2}, \tag{60}$$

$$\dot{E}_{r2} = \dot{E}_{f2} - \gamma_2 (E_{r2} - r_2 E_{f2}) + \frac{t_s t_2}{t_1 \tau_{rt2}} (E_{r1} - r_1 E_{f1}) - \frac{t_2^2}{\tau_{rt2}} E_{f2} - \frac{t_1 t_2 t_s}{\tau_{rt2}} E_{f1}. \tag{61}$$

For constant E_j, $\ddot{E}_{rj} = it_j \ddot{E}_{sj}$, so from Eq. (58) we have:

$$\ddot{E}_{s1} = -\gamma_1 \dot{E}_{s1} - \frac{t_s}{\tau_{rt1}} \dot{E}_{s2}. \tag{62}$$

From (58) and (59), we have:

$$\ddot{E}_{s1} = -\gamma_1 \dot{E}_{s1} - \frac{t_s}{\tau_{rt1}} \left\{ -\gamma_2 E_{s2} + \frac{t_s}{\tau_{rt2}} E_{s1} + \frac{it_2}{\tau_{rt2}} E_{f2} + \frac{it_1 t_s}{\tau_{rt2}} E_{f1} \right\}, \tag{63}$$

so,

$$\ddot{E}_{s1} = -\gamma_1 \dot{E}_{s1} - \frac{t_s}{\tau_{rt1}} \left\{ \begin{array}{l} \gamma_2 \dfrac{\left(\dot{E}_{s1} + \gamma_1 E_{s1} - \dfrac{it_1}{\tau_{rt1}} E_{f1} + \dfrac{it_2 t_s}{\tau_{rt1}} E_{f2} \right)}{\dfrac{t_s}{\tau_{rt1}}} \\ + \dfrac{t_s}{\tau_{rt2}} E_{s1} + \dfrac{it_2}{\tau_{rt2}} E_{f2} + \dfrac{it_1 t_s}{\tau_{rt2}} E_{f1} \end{array} \right\}. \quad (64)$$

Or,

$$\ddot{E}_{s1} = -(\gamma_1 + \gamma_2)\dot{E}_{s1} - \left(\frac{T_s}{\tau_{rt1}\tau_{rt2}} + \gamma_1\gamma_2 \right) E_{s1} + \left(\frac{it_1\gamma_2}{\tau_{rt1}} - \frac{it_1 T_s}{\tau_{rt1}\tau_{rt2}} \right) E_{f1} \quad (65)$$
$$- \left(\frac{it_2 t_s}{\tau_{rt1}\tau_{rt2}} + \frac{i\gamma_2 t_2 t_s}{\tau_{rt1}} \right) E_{f2}.$$

Finally, we have:

$$\ddot{E}_{s1} + (\gamma_1 + \gamma_2)\dot{E}_{s1} + \left(\frac{T_s}{\tau_{rt1}\tau_{rt2}} + \gamma_1\gamma_2 \right) E_{s1} = \frac{it_1\gamma_2}{\tau_{rt1}} E_{f1} - \frac{it_2 t_s}{\tau_{rt1}\tau_{rt2}} E_{f2}. \quad (66)$$

This equation has the form of a driven damped oscillator; with $E_{s1} \propto e^{\lambda t}$ and $E_{f1} = E_{f2} = 0$, just as in Eq. (33) we have the characteristic equation:

$$\lambda^2 + (\gamma_1 + \gamma_2)\lambda + \left(\gamma_1\gamma_2 + \frac{T_s}{\tau_{rt1}\tau_{rt2}} \right) = 0. \quad (67)$$

Similar to Eq. (35), we have the roots:

$$\lambda_{1,2} = -\frac{\gamma_1 + \gamma_2}{2} \pm \sqrt{\left(\frac{\gamma_1 - \gamma_2}{2} \right)^2 - \frac{T_s}{\tau_{rt1}\tau_{rt2}}}. \quad (68)$$

For $T_s \to 0$, we have $E_{s1} \approx e^{-\gamma_1 t}$ and $E_{s2} \approx e^{-y_2 t}$. But when $\gamma_1 = \gamma_2$, we have $E_{s1} \approx e^{-\gamma_1 t} e^{\pm i\omega t}$, where $\omega = \sqrt{\frac{T_s}{\tau_{rt1}\tau_{rt2}}} \approx \frac{t_s}{\tau_{rt}}$. At this point, the mode splitting starts to occur, and the splitting is proportional to t_s.

Both the scattering model and the rotational model will be examined in detail in the following sections.

VI.2. Comparison in the case of no CPC

For the scattering model, Eqs. (55) and (56) become Eqs. (7) and (8):

$$E_{s1} = \frac{E_{f1}}{D}[it_1 e_1 (r_s - r_2 e_2)] - \frac{E_{f2}}{D}[t_2 t_s e_1],$$

$$E_{s2} = \frac{E_{f2}}{D}[it_2 e_2 (r_s - r_1 e_1)] - \frac{E_{f1}}{D}[t_1 t_s e_2].$$

Here, D is also given by Eq. (57), and the only difference between the two sets of equations is in their second right-hand terms, involving t_s.

For the ***scattering model:*** when $T_s = 0$, we have $it_s = 0$, and $r_s = 1$.

The intracavity fields are given accordingly:

$$E_{s1} = \frac{it_1 e_1}{1 - r_1 e_1} E_{f1}, \tag{69}$$

$$E_{s2} = \frac{it_2 e_2}{1 - r_2 e_2} E_{f2}. \tag{70}$$

The throughput fields are calculated as:

$$E_{r1} = \frac{r_1 - e_1}{1 - r_1 e_1} E_{f1}, \tag{71}$$

$$E_{r2} = \frac{r_2 - e_2}{1 - r_2 e_2} E_{f2}. \tag{72}$$

The detected field components are given by:

$$E_{a1} = \cos\psi E_{r1} + \sin\psi E_{r2}, \tag{73}$$

$$E_{a2} = -\sin\psi E_{r1} + \cos\psi E_{r2}. \tag{74}$$

For the ***rotational model:*** when $T_s = 0$, we have $t_s = 0$, and $r_s = 1$. As a result, we get the same intracavity and throughput fields and detected field components as in Eqs. (69) through (74) above. In particular, for CPIT/CPIA experiments: $\theta = 45^o$, we have $E_{f1} = E_{f2} = \frac{1}{\sqrt{2}}$, and $\psi = 45^o$, we have $\cos\psi = \sin\psi = \frac{1}{\sqrt{2}}$, so:

$$E_{a1} = \frac{1}{\sqrt{2}}(E_{r1} + E_{r2}) = \frac{1}{2}(\frac{r_1 - e_1}{1 - r_1 e_1} + \frac{r_2 - e_2}{1 - r_2 e_2}), \tag{75}$$

$$E_{a2} = \frac{1}{\sqrt{2}}(-E_{r1} + E_{r2}) = \frac{1}{2}(-\frac{r_1 - e_1}{1 - r_1 e_1} + \frac{r_2 - e_2}{1 - r_2 e_2}). \tag{76}$$

VI.3. Comparison in the case of CPC

For the ***scattering model:*** when $T_s \neq 0$, we again have Eqs. (7) and (8):

$$E_{s1} = \frac{E_{f1}}{D}[it_1 e_1 (r_s - r_2 e_2)] - \frac{E_{f2}}{D}[t_2 t_s e_1],$$

$$E_{s2} = \frac{E_{f2}}{D}[it_2 e_2 (r_s - r_1 e_1)] - \frac{E_{f1}}{D}[t_1 t_s e_2].$$

The throughput fields are calculated as in Eqs. (10) and (11) and the detected field components are calculated as in Eqs. (73) and (74), respectively.

For CMIT/CMIA experiments: $\theta = 0$, $E_{f2} = 0$, $E_{f1} = 1$, and $\psi = 0$, so according to Eqs. (7) and (8) we have:

$$E_{s1} = \frac{1}{D}[it_1 e_1 (r_s - r_2 e_2)], \tag{77}$$

$$E_{s2} = \frac{1}{D}[-t_1 t_s e_2]. \tag{78}$$

The throughput fields are calculated as:

$$E_{r1} = r_1 + \frac{1}{D}[-t_1^2 e_1 (r_s - r_2 e_2)], \tag{79}$$

$$E_{r2} = \frac{1}{D}[-it_1 t_2 t_s e_2]. \tag{80}$$

Finally, we end up with the detected field components:

$$E_{a1} = E_{r1}, \tag{81}$$

$$E_{a2} = E_{r2}. \tag{82}$$

For CPIT/CPIA experiments: θ = 45°, $E_{f1} = E_{f2} = 1/\sqrt{2}$, and ψ = 45°, so we have:

$$E_{s1} = \frac{1}{\sqrt{2}D}[it_1 e_1 (r_s - r_2 e_2) - t_2 t_s e_1], \tag{83}$$

$$E_{s2} = \frac{1}{\sqrt{2}D}[it_2 e_2 (r_s - r_1 e_1) - t_1 t_s e_2]. \tag{84}$$

The throughput fields are calculated as:

$$E_{r1} = \frac{1}{\sqrt{2}}\left\{r_1 + \frac{it_1}{D}[it_1 e_1 (r_s - r_2 e_2) - t_2 t_s e_1]\right\}, \tag{85}$$

$$E_{r2} = \frac{1}{\sqrt{2}}\left\{r_2 + \frac{it_2}{D}[it_2 e_2 (r_s - r_1 e_1) - t_1 t_s e_2]\right\}. \tag{86}$$

Again, the detected field components:

$$E_{a1} = \frac{1}{2}\begin{Bmatrix} r_1 + \frac{it_1}{D}[it_1 e_1 (r_s - r_2 e_2) - t_2 t_s e_1] \\ + r_2 + \frac{it_2}{D}[it_2 e_2 (r_s - r_1 e_1) - t_1 t_s e_2] \end{Bmatrix}, \tag{87}$$

$$E_{a2} = \frac{1}{2}\begin{Bmatrix} -r_1 - \dfrac{it_1}{D}[it_1 e_1 (r_s - r_2 e_2) - t_2 t_s e_1] \\ +r_2 + \dfrac{it_2}{D}[it_2 e_2 (r_s - r_1 e_1) - t_1 t_s e_2] \end{Bmatrix}. \tag{88}$$

For the ***rotational model:*** when $T_s \neq 0$, we again have Eqs. (55) and (56):

$$E_{s1} = \frac{E_{f1}}{D}[it_1 e_1 (r_s - r_2 e_2)] - \frac{E_{f2}}{D}[it_2 t_s e_1],$$

$$E_{s2} = \frac{E_{f2}}{D}[it_2 e_2 (r_s - r_1 e_1)] + \frac{E_{f1}}{D}[it_1 t_s e_2].$$

The throughput fields are calculated as in Eqs. (10) and (11) and the detected field components are calculated as in Eqs. (73) and (74), respectively.

For CMIT/CMIA experiments: $\theta = 0$, $E_{f2} = 0$, $E_{f1} = 1$, and $\psi = 0$, so according to Eqs. (55) and (56) we have:

$$E_{s1} = \frac{1}{D}[it_1 e_1 (r_s - r_2 e_2)], \tag{89}$$

$$E_{s2} = \frac{1}{D}[it_1 t_s e_2]. \tag{90}$$

The throughput fields are calculated as:

$$E_{r1} = r_1 + \frac{1}{D}[-t_1^2 e_1 (r_s - r_2 e_2)], \tag{91}$$

$$E_{r2} = \frac{1}{D}[-t_1 t_2 t_s e_2]. \tag{92}$$

And, the detected field components are again given:

$$E_{a1} = E_{r1}, \tag{93}$$

$$E_{a2} = E_{r2}. \tag{94}$$

For CPIT/CPIA experiments: $\theta = 45^{\circ}$, $E_{f1} = E_{f2} = 1/\sqrt{2}$, and $\psi = 45^{\circ}$, so we

have:

$$E_{s1} = \frac{1}{\sqrt{2}D}[it_1 e_1 (r_s - r_2 e_2) - it_2 t_s e_1], \tag{95}$$

$$E_{s2} = \frac{1}{\sqrt{2}D}[it_2 e_2 (r_s - r_1 e_1) + it_1 t_s e_2]. \tag{96}$$

The throughput fields are calculated as:

$$E_{r1} = \frac{1}{\sqrt{2}}\left\{r_1 + \frac{it_1}{D}[it_1 e_1 (r_s - r_2 e_2) - it_2 t_s e_1]\right\}, \tag{97}$$

$$E_{r2} = \frac{1}{\sqrt{2}}\left\{r_2 + \frac{it_2}{D}[it_2 e_2 (r_s - r_1 e_1) + it_1 t_s e_2]\right\}. \tag{98}$$

Finally, we end up with the detected field components:

$$E_{a1} = \frac{1}{2}\left\{\begin{array}{l} r_1 + \frac{it_1}{D}[it_1 e_1 (r_s - r_2 e_2) - it_2 t_s e_1] \\ + r_2 + \frac{it_2}{D}[it_2 e_2 (r_s - r_1 e_1) + it_1 t_s e_2] \end{array}\right\}, \tag{99}$$

$$E_{a2} = \frac{1}{2}\left\{\begin{array}{l} -r_1 - \frac{it_1}{D}[it_1 e_1 (r_s - r_2 e_2) - it_2 t_s e_1] \\ + r_2 + \frac{it_2}{D}[it_2 e_2 (r_s - r_1 e_1) + it_1 t_s e_2] \end{array}\right\}. \tag{100}$$

From the above analytical results for CMIT/CMIA and CPIT/CPIA, we give some remarks in the next section.

VI.4. Comments and examples

For the CMIT/CMIA experiment:

When $T_s = 0$, we do not have CMIT/CMIA.

When $T_s \neq 0$, we have the CMIT/CMIA throughput signal. Since we have only one component input, and we are looking at the parallel polarized throughput for E_{a1}, the

throughput shapes for CMIT/CMIA for both scattering and rotational models are the same no matter what the value of T_s is. This can be seen in Eqs. (79), (81) and (91), (93) which are identical.

For the CPIT/CPIA experiment:

When $T_s = 0$, Eqs. (87) and (99) are identical, so the CPIT/CPIA throughput shape is independent of which model is used. Furthermore, the intracavity fields for the scattering model and the rotational model are given, respectively, according to Eqs. (7), (8) and Eqs. (55), (56) as:

$$E_{s1} = \frac{E_{f1}}{D}[it_1 e_1 (1 - r_2 e_2)], \tag{101}$$

$$E_{s2} = \frac{E_{f2}}{D}[it_2 e_2 (1 - r_1 e_1)]. \tag{102}$$

We see that E_{s1} and E_{s2} have the same form so switching $1 \leftrightarrow 2$ for TE and TM modes does not affect the throughput shape.

When $T_s \neq 0$, the intracavity fields for the scattering model given in Eqs. (7) and (8) have the same form, so switching $1 \leftrightarrow 2$ for TE and TM modes does not affect the throughput shape. The intracavity fields for the rotational model given in Eqs. (55) and (56) are different because a particular sense of polarization rotation has been assumed, so switching $1 \leftrightarrow 2$ for TE and TM modes affects the throughput shape, and they are different from the intracavity fields for the scattering model as well. Those differences are illustrated in Fig. 71 (scattering model) previously and Figs. 79 and 80 (rotational model, forward and reverse) below.

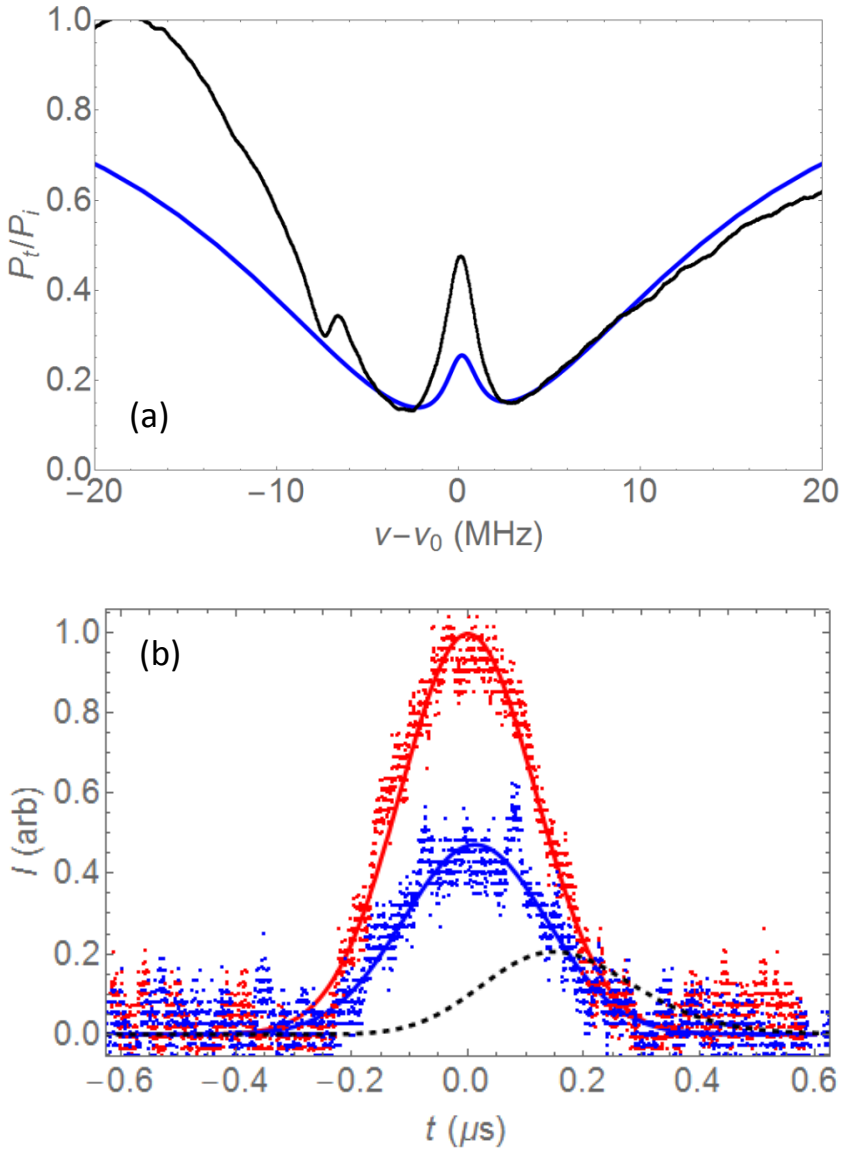

Figure 79. CPIT with 280-μm-radius microsphere. (a) Experimental (black) and model (blue) throughput spectra. (b) Experimental input (red) and throughput (blue) pulses, with an input pulse width of 280 ns and a delay of 24 ns, and model throughput pulse (dashed black), with a delay of 150 ns. Parameter values: M_1 = 0.47 (overcoupled), M_2 = 0.92 (overcoupled), Q_1 = 6.56×10^6, Q_2 = 8.8×10^7; offset = 0.15 MHz, T_s = 5×10^{-16}, pulse detuning = 0.1 MHz.

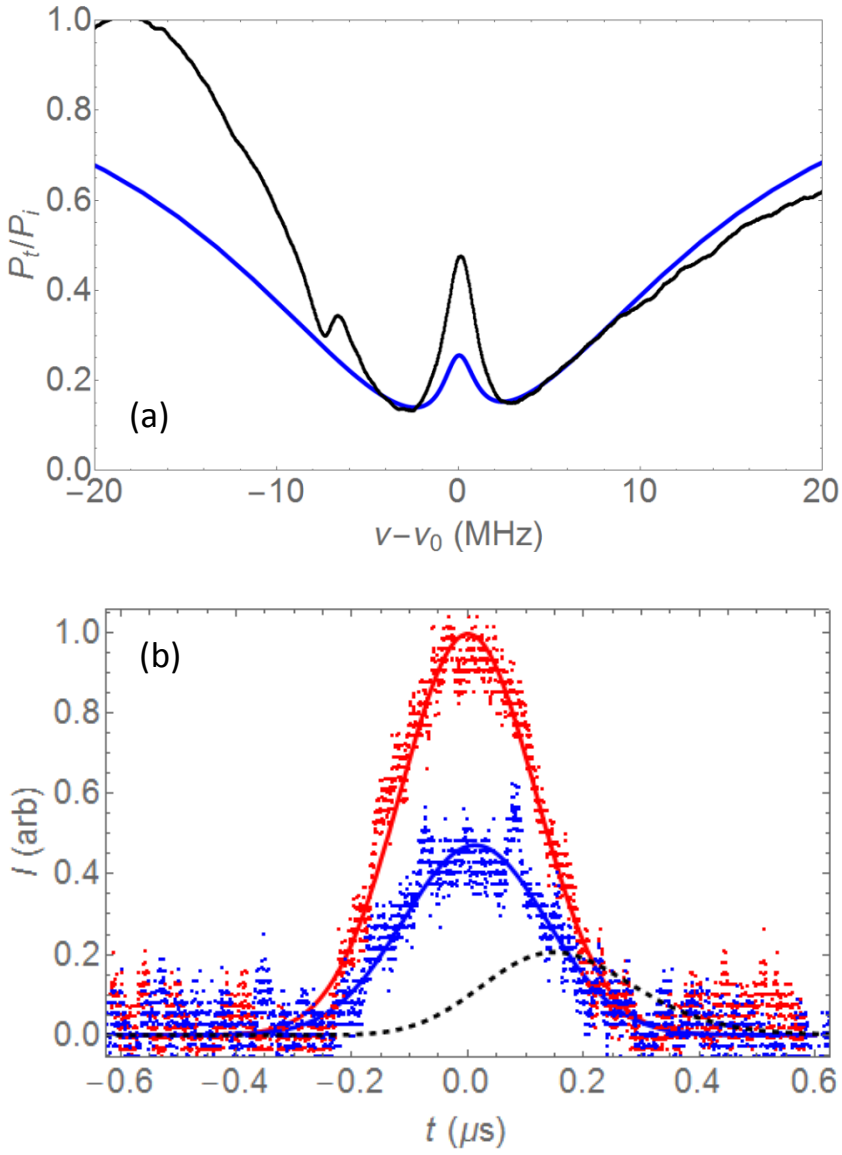

Figure 80. CPIT with 280-μm-radius microsphere. (a) Experimental (black) and model (blue) throughput spectra. (b) Experimental input (red) and throughput (blue) pulses, with an input pulse width of 280 ns and a delay of 24 ns, and model throughput pulse (dashed black), with a delay of 150 ns. Parameter values: M_1 = 0.92 (overcoupled), M_2 = 0.47 (overcoupled), Q_1 = 8.8×10^7, Q_2 = 6.56×10^6; offset = -0.15 MHz, T_s = 5×10^{-16}, pulse detuning = 0 MHz.

In Fig. 71, the hybrid CPIT and CMIT throughput signal for the CPIT and pulse delay experiment with microsphere has been fitted successfully with $T_s = 2\times10^{-8}$ by using the scattering model but it was not fitted well when using the rotational model either in the forward order (as in Fig. 79) or in the reverse order (as in Fig. 80) of the input data such as quality factors *Q*, dip depths *M*, and coupling regimes of the modes. These differences are accounted for by the dissimilar intracavity fields between the scattering model and the rotational model in both forward and reverse orders. Those differences lead to the unlike responses of the resonant throughput pulses, respectively. Using the rotational model, to get the transparency feature to be as high as possible, the CPC (T_s) has to be minimized, and thus there is not really any difference between Figs. 79 and 80.

This problem happens again for the CPIT and pulse delay experiment with HBR in Figs. 81 (scattering), 82 (rotational, forward), and 83 (rotational, reverse) below. Again, for the rotational model, maximum transparency means minimum T_s, so Figs. 82 and 83 are identical except for the chosen offsets and pulse detunings.

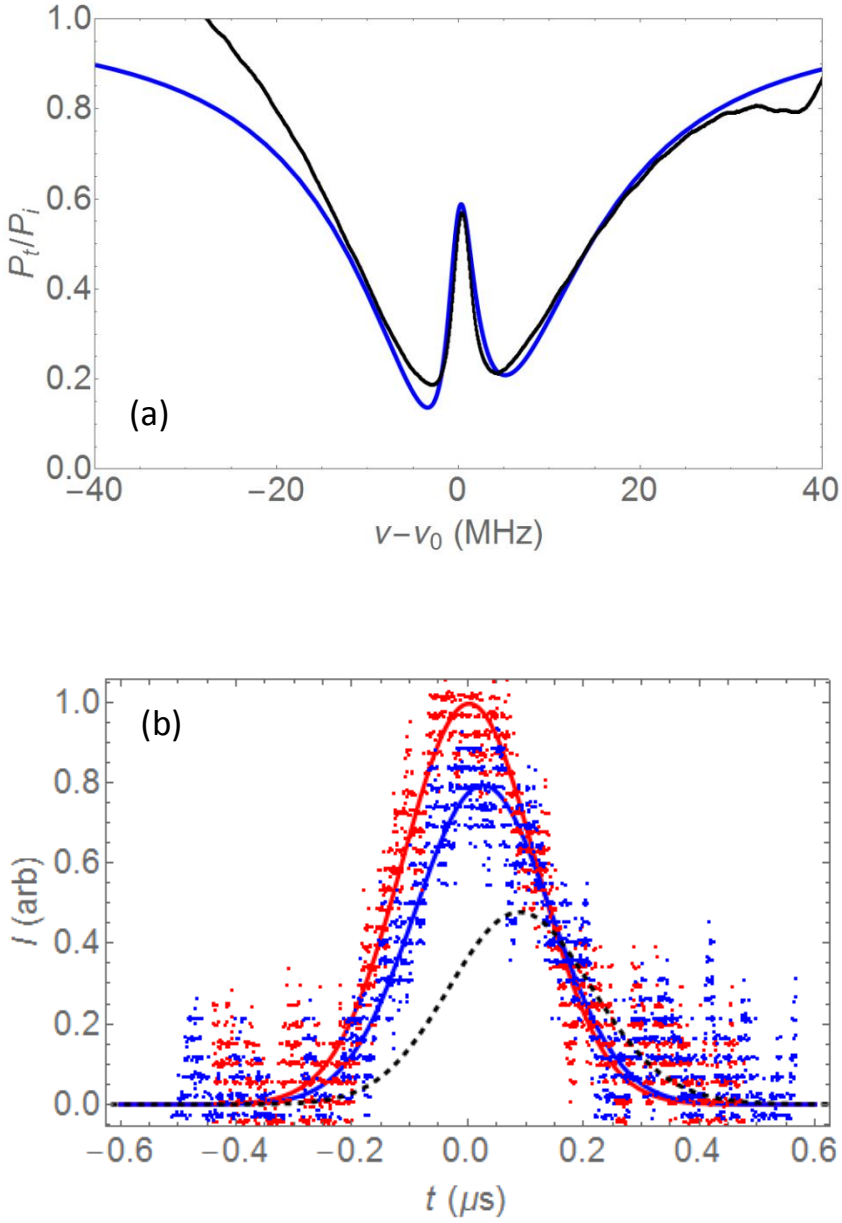

Figure 81. CPIT with 175-μm-radius HBR. (a) Experimental (black) and model (blue) throughput spectra. (b) Experimental input (red) and throughput (blue) pulses, with an input pulse width of 265 ns and a delay of 24 ns, and model throughput pulse (dashed black), with a delay of 80 ns. Parameter values: M_1 = 0.78 (overcoupled), M_2 = 0.42 (overcoupled), Q_1 = 8.7×10^7, Q_2 = 6.6×10^6; offset = 1.2 MHz, T_s = 10^{-8}, pulse detuning = 0.3 MHz.

In Fig. 81, the experimental hybrid CPIT and CMIT throughput spectrum (in black) was fitted by using the scattering computer model (in blue). The experimental data can be fitted by the scattering model with the value of cross polarization coupling strength $T_s = 10^{-8}$, but not quite as well with the rotational model in the forward order with $T_s = 5 \times 10^{-16}$ as in Fig. 82 and in the reverse order with $T_s = 5 \times 10^{-16}$ as in Fig. 83 due to the difference in intracavity fields between the models. The experimental time delay is smaller than all model calculations, meaning that the experimental off resonant throughput pulse is not far enough off and still experiences some delay. For this experiment, the HBR diameter is measured to be equal to 350 μm, and the experimental delay-bandwidth product is calculated to be equal to 0.04.

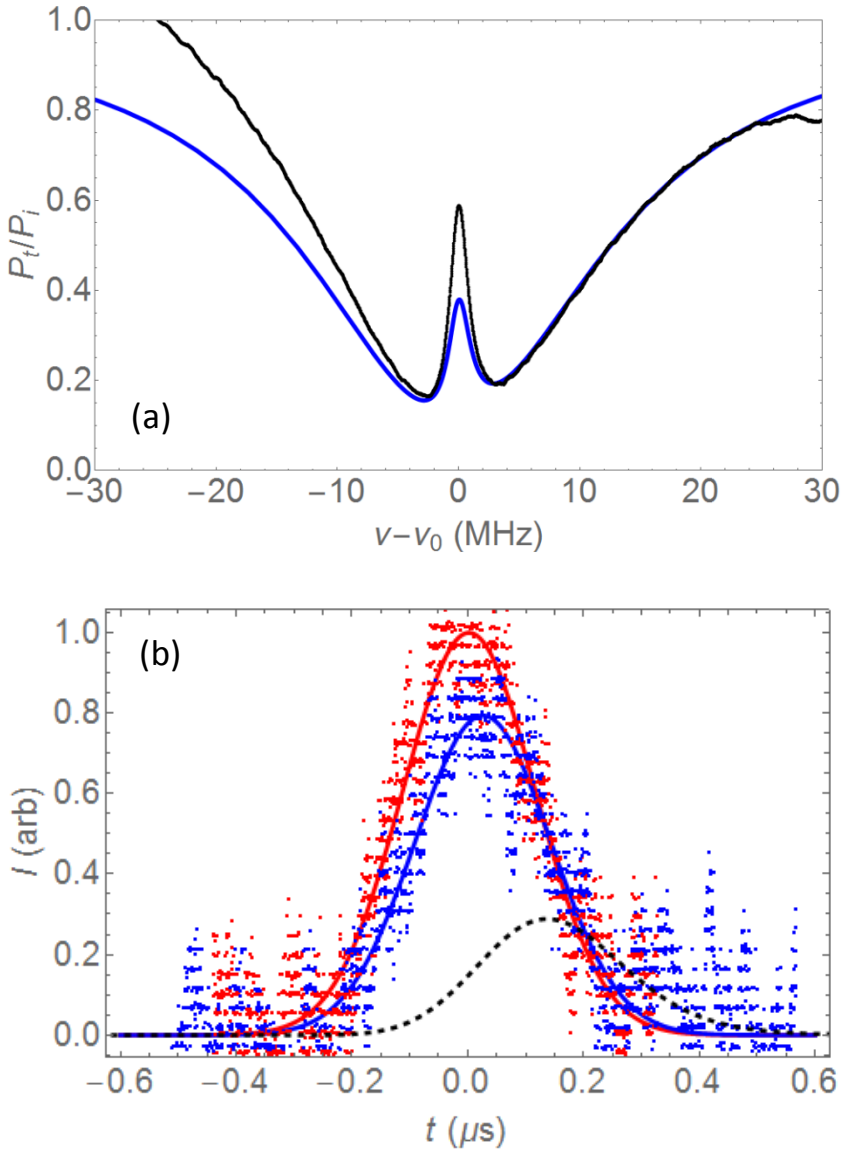

Figure 82. CPIT with 175-μm-radius HBR. (a) Experimental (black) and model (blue) throughput spectra. (b) Experimental input (red) and throughput (blue) pulses, with an input pulse width of 265 ns and a delay of 24 ns, and model throughput pulse (dashed black), with a delay of 120 ns. Parameter values: M_1 = 0.78 (overcoupled), M_2 = 0.42 (overcoupled), Q_1 = 8.7×10^7, Q_2 = 6.6×10^6; offset = -0.4 MHz, T_s = 5×10^{-16}, pulse detuning = 0 MHz.

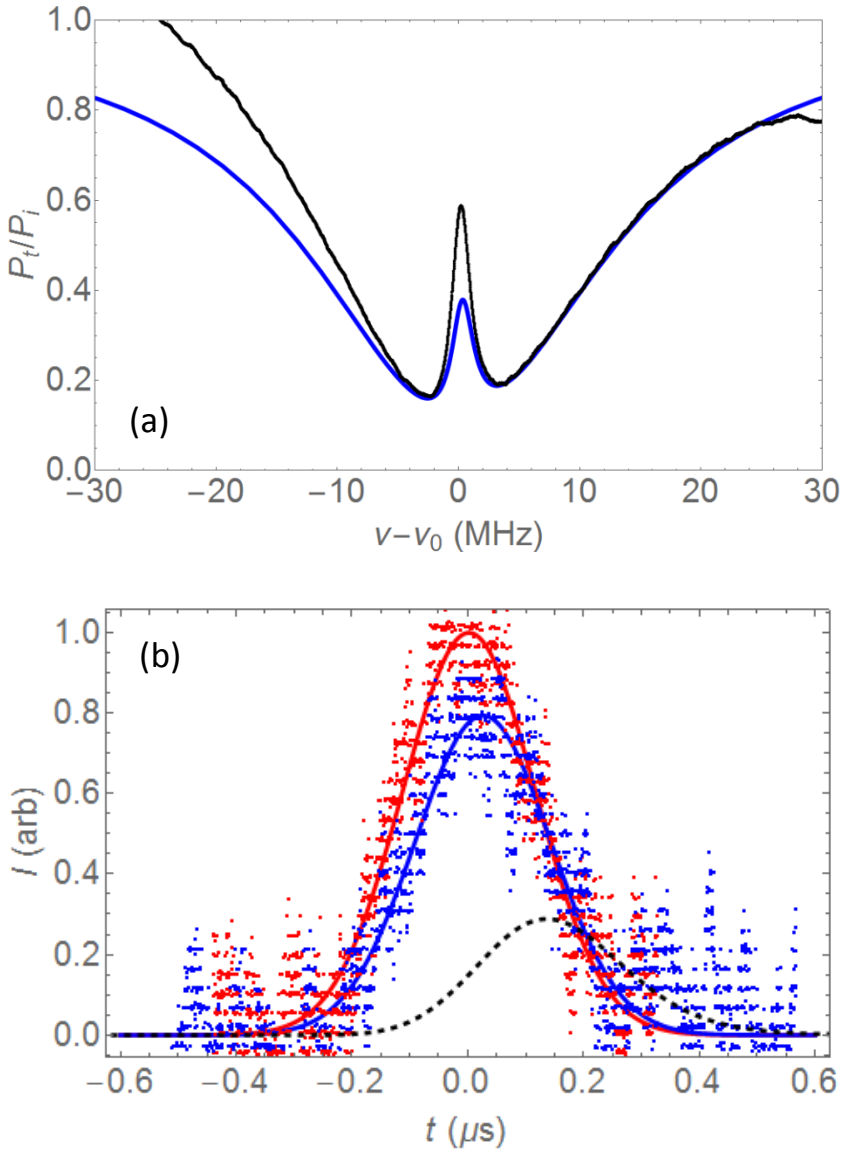

Figure 83. CPIT with 175-μm-radius HBR. (a) Experimental (black) and model (blue) throughput spectra. (b) Experimental input (red) and throughput (blue) pulses, with an input pulse width of 265 ns and a delay of 24 ns, and model throughput pulse (dashed black), with a delay of 130 ns. Parameter values: M_1 = 0.42 (overcoupled), M_2 = 0.78 (overcoupled), Q_1 = 6.6×10^6, Q_2 = 8.7×10^7; offset = 0.3 MHz, T_s = 5×10^{-16}, pulse detuning = 0.4 MHz.

In some cases, the throughput spectrum can be fitted well with both models; rotational model with forward order of input data as in Fig. 84 or rotational model with reverse order of input data as in Fig. 85 or scattering model as in Fig. 86 below.

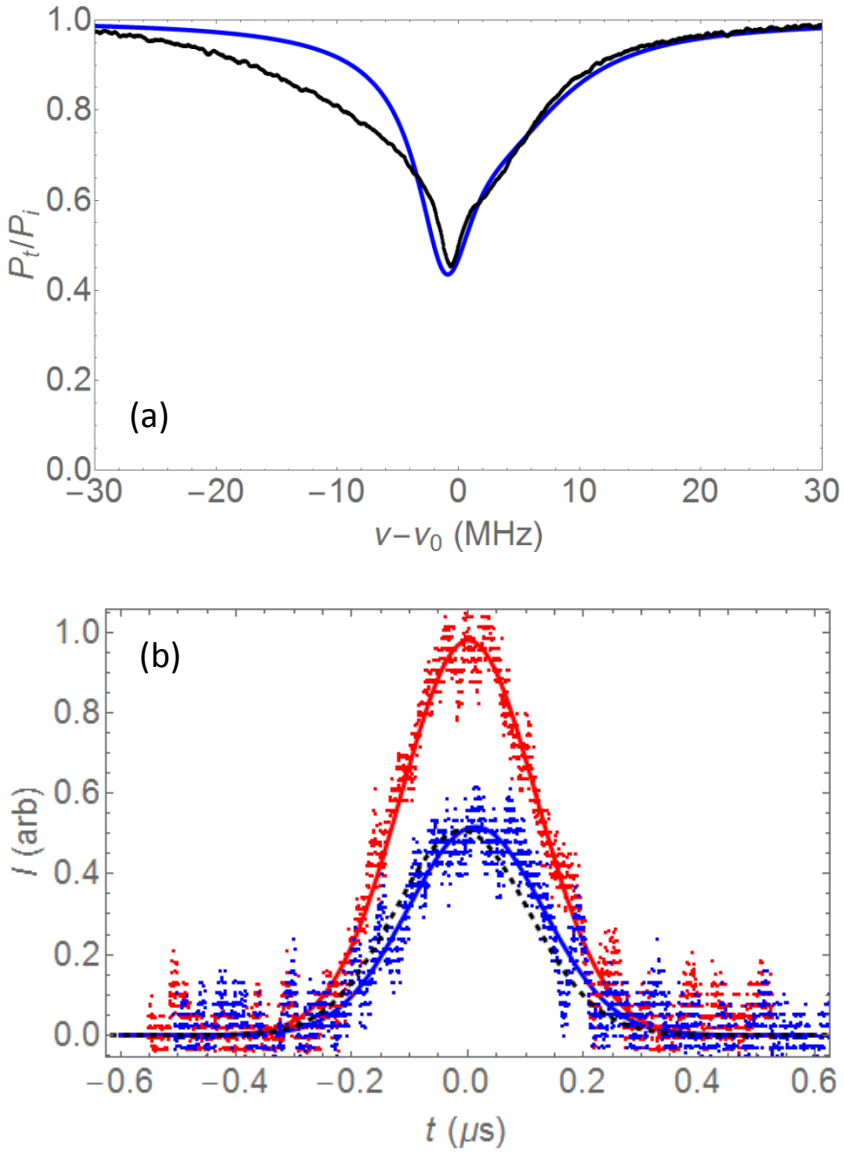

Figure 84. CPIA with 175-µm-radius HBR. (a) Experimental (black) and model (blue) throughput spectra. (b) Experimental input (red) and throughput (blue) pulses, with an input pulse width of 275 ns and a delay of 12 ns, and model throughput pulse (dashed black), with an advancement of 25 ns. Parameter values: M_1 = 0.77 (overcoupled), M_2 = 0.35 (undercoupled), Q_1 = 1×10^8, Q_2 = 1.1×10^7; offset = 2.5 MHz, T_s = 1.6×10^{-8}, pulse detuning = 0.4 MHz.

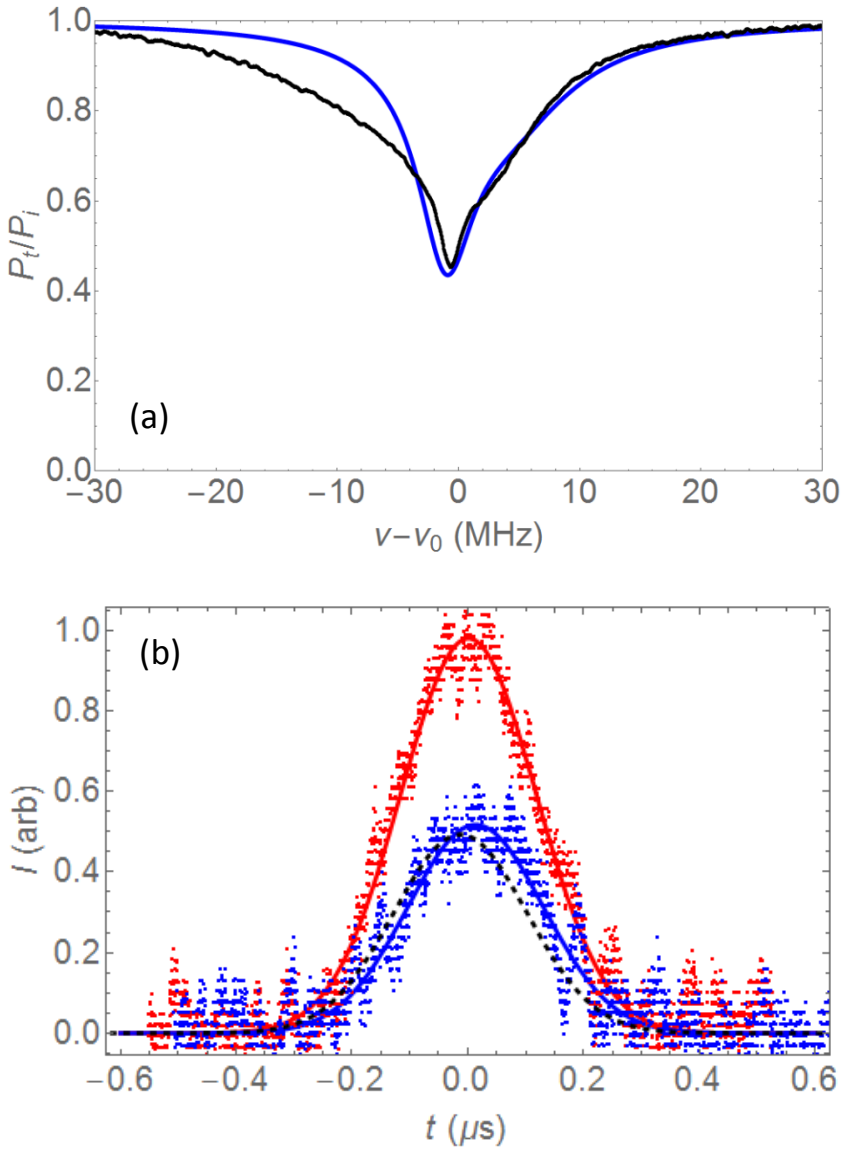

Figure 85. CPIA with 175-µm-radius HBR. (a) Experimental (black) and model (blue) throughput spectra. (b) Experimental input (red) and throughput (blue) pulses, with an input pulse width of 275 ns and a delay of 12 ns, and model throughput pulse (dashed black), with an advancement of 25 ns. Parameter values: M_1 = 0.35 (undercoupled), M_2 = 077 (overcoupled), Q_1 = 1.1×10^7, Q_2 = 1×10^8; offset = -2.5 MHz, T_s = 1.6×10^{-8}, pulse detuning = -2.4 MHz.

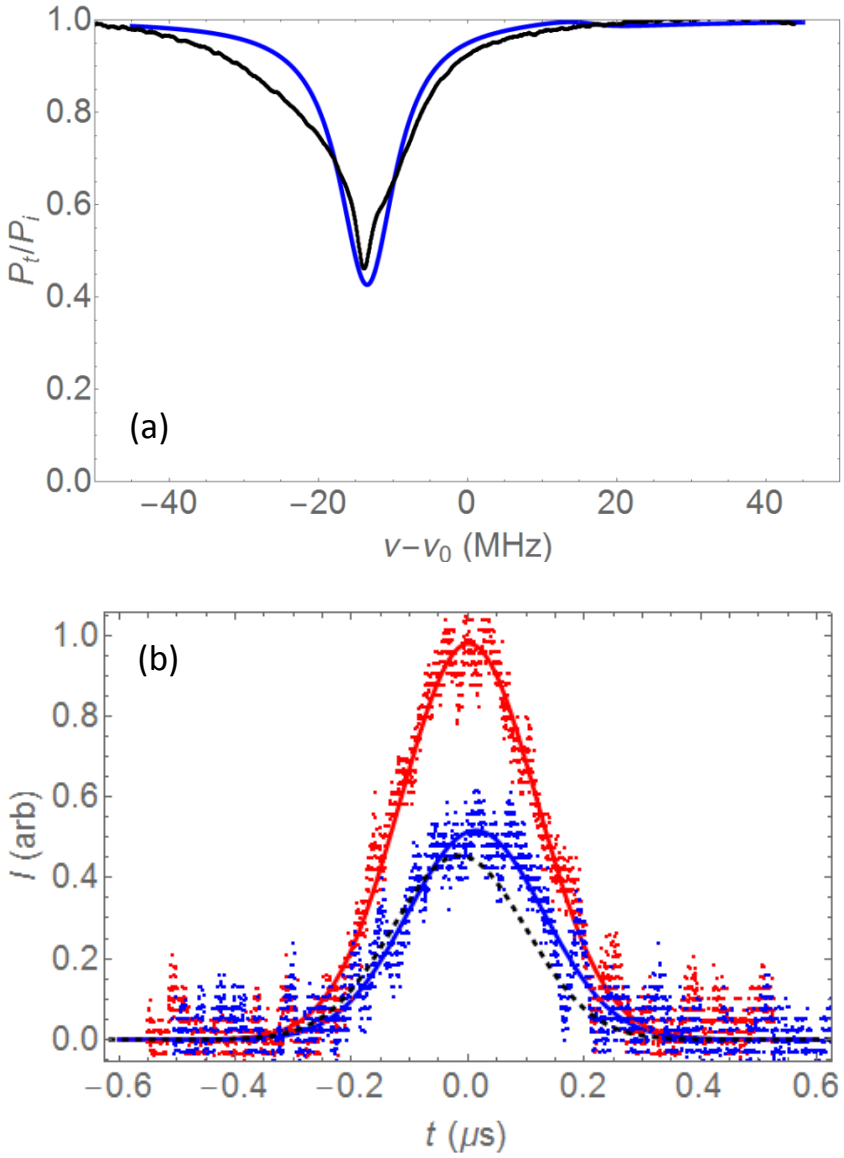

Figure 86. CPIA with 175-µm-radius HBR. (a) Experimental (black) and model (blue) throughput spectra. (b) Experimental input (red) and throughput (blue) pulses, with an input pulse width of 275 ns and a delay of 12 ns, and model throughput pulse (dashed black), with an advancement of 25 ns. Parameter values: M_1 = 0.77 (overcoupled), M_2 = 0.35 (undercoupled), Q_1 = 1×10^8, Q_2 = 1.1×10^7; offset = 2.5 MHz, T_s = 2.5×10^{-7}, pulse detuning = -14 MHz.

In Figs. 84 and 85, the experimental CPIA throughput spectrum (in black) was fitted by using the rotational computer model (in blue) with the value of cross polarization coupling strength $T_s = 1.6 \times 10^{-8}$ and in Fig. 86, the experimental data (in black) was fitted by using the scattering model (in blue) with the value of cross polarization coupling strength $T_s = 2.5 \times 10^{-7}$. The fittings in Figs. 84, 85 and 86 are almost the same, the main differences between those cases are offsets and pulse detunings. For this experiment, the HBR diameter is measured to be equal to 350 μm and the responses of the experimental throughput pulses are different from the model calculations meaning that the experimental resonant throughput pulses are not truly on resonance or the off resonant throughput pulses are not really off resonance.

It seems that there is too much variability in the experimental results to decide whether one model is better than the other. This means that we cannot confirm which mechanism is responsible for cross-polarization coupling. However, for our CMIT/CMIA and CPIT/CPIA results, the models are equivalent, so for most of the work presented here, it doesn't matter.

CHAPTER VII

CONCLUSIONS

In this chapter, a summary of this dissertation will be given. The topics include EIT/ATS and EIA fundamental concepts, scattering and rotational numerical models used to predict the experimental processes, two new experimental methods – CMIT/CMIA and CPIT/CPIA – to produce the EIT-like/ATS and EIA-like features of the throughput power spectrum with microsphere and hollow bottle resonator, the relations between EIT-like/ATS throughput shape to slow light and EIA-like throughput shape to either fast light or slow light, and the roles of the scattering and rotational models for fitting the experimental data. Moreover, the achievements of this research project will be evaluated and the problems remaining to affect the experimental CMIT/ATS/CMIA and CPIT/CPIA processes will be discussed. The solutions for those problems in the future and potential new applications of this project will also be mentioned.

Since EIT was first proposed theoretically by a professor and a graduate student in Gorky State University, Russia [44], people have been using many different methods such as sweeping the resonances with tunable lasers [45], microresonator coupling [46], or changing the excitation conditions [47], etc., with many types of materials such as metamaterials [48], ultracold atomic gas [49], microcavities [50], and so on, to produce the EIT-like effect of the throughput power.

EIT is defined as the destructive interference of two optical transition paths of an atomic system resulting in the reduction of the probe absorption produced by a coupling field. When the coupling field is acting on the atomic system and is greater than a critical value, mode splitting occurs and EIT gradually switches into Autler-Townes splitting (ATS). EIA can be accounted for by the constructive interference between the transfer of population and transfer of coherence between two hyperfine ground and excited states of an atomic system in which $F_g \rightarrow F_e = F_g + 1$ with $F_g > 0$.

In our lab, EIT-like/ATS and EIA-like effects were studied both theoretically and experimentally by several methods including coupled resonator induced transparency, based on the evanescent coupling between two coresonant whispering gallery modes of the same polarization of the two microspheres; coupled mode induced transparency, based on CPC presumably arising from polarization rotation between orthogonally polarized TE and TM modes inside the resonator due to the asymmetry of the microresonator about its equator; and coresonant polarization induced transparency, based on the superposition of two coresonant orthogonally polarized TE and TM modes.

CMIT is a method which relies on the destructive interference between direct and indirect excitation paths due to intermode coupling between coresonant modes of orthogonal polarization, such as TE and TM, when one mode is driven at the input of an optical system. This method is a new approach; most previous single-resonator induced transparency observations involve coresonant modes of the same polarization but different radial orders [50]. When the coupling is strong enough, mode splitting occurs and CMIT becomes ATS. The split modes at lower and higher frequencies are symmetric and antisymmetric combinations of TE and TM modes.

CPIT is a new approach to get a similar result to the two above methods, CRIT and CMIT, but it was implemented in a different way. The input light is linearly polarized at 45^{o} with respect to the resonator's basis and the throughput component polarized parallel to the input is detected. The superposition of two coresonant orthogonally polarized TE and TM modes (obtained either by coincidental searching or by strain tuning the microresonator using the piezoelectric transducer) can produce the EIT-like feature of the throughput power. Cross polarization coupling is not required in this procedure as for CMIT/ATS but the coresonance between TE and TM modes is a prerequisite for both methods.

Using a computer model to simulate the actual physical processes is desirable before starting to do actual experiments in the lab. In this research project, we use two computer models: the scattering model, in which the cross polarization coupling effect between TE and TM modes is treated as scattering; and the rotational model, in which the cross polarization coupling effect is treated as polarization rotation. These are used to simulate the CMIT/ATS/CMIA and CPIT/CPIA processes. These plane-wave ring cavity

models are greatly simplified in comparison to the actual evanescent excitation of cross-polarization-coupled WGMs in a microresonator, but the models are realistic enough to provide good fits to experimental results in most cases.

The microsphere provides a simple experimental research tool for both CMIT/ATS and CPIT methods but it is hard to find two very different quality factor TE and TM modes. Moreover, bringing these two orthogonally polarized modes into the state of coresonance by compressing the microsphere is truly a challenge. Due to the strong axial curvature of the microsphere, we can excite many axial order modes. This makes the mode density denser and the overlap among the modes affects the mode of interest and reduces the quality of the experimental results.

Switching from the microsphere to the hollow bottle resonator can partially solve this problem. By thinning the HBR wall, we can easily find the higher-Q and lower-Q modes needed for our experiment because the higher radial order modes will experience more loss due to scattering with the internal surface of the HBR. More loss will result in lower Q modes. Coresonance between these two orthogonally polarized modes now becomes easier to achieve; by stretching the HBR, these TE and TM modes will be shifted at different rates and that is enough to bring them into coresonance. Since the cross polarization coupling between TE and TM modes depends on spatial mode overlap, by relocating the tapered fiber along the HBR axis, we can select the position of the most CPC for CMIT/ATS and the least CPC for CPIT experiments. Due to the gentle axial curvature of the HBR, the axial order modes are spread along the HBR axis, so fewer will be simultaneously excited. This makes the mode density cleaner compared to that using the microsphere. Furthermore, reducing the capillary diameter will help us to increase

the free spectral range between the modes; the greater the free spectral range, the rarer the mode density.

Pulse delay or pulse advancement, referring to the peak time of the pulse at resonance relative to its off-resonant peak time, are forms of "slow light" or "fast light" respectively. The amount of delay or advancement could be controlled by varying the cross polarization coupling strength T_s between the orthogonally polarized TE and TM modes for CMIT/ATS/CMIA, but doing so is very difficult. However, the amount of delay or advancement can be controlled by changing the polarization angle of the input light with respect to the resonator's basis and orienting the throughput detectors as for CPIT/CPIA. These are used to calculate the delay-bandwidth or advancement-bandwidth products, which are fundamental parameters of capacity of an optical buffer [41]. In the near future, the delay or advancement of the throughput pulse can be enhanced by changing the polarization angle of the input light for CPIT/CPIA (proved by the numerical model) or increasing the pulse width (proved by the numerical model) since increasing the pulse width means reducing the bandwidth of the pulse. As a result, the whole pulse will be centered more closely to the resonance frequency and experience a larger dispersion slope. Larger steep dispersion means larger time delay or advancement. However, this method has some drawbacks since we cannot increase the pulse width indefinitely, and the relative (to pulse width) delay or advancement will be reduced.

For any method to produce slow light, large time delay and low loss are required. For our CMIT/ATS and CPIT experiments, the transparency of the throughput spectrum is still low and needs to be improved. The transparency seems to be hard to manage by changing the cross polarization coupling for CMIT/ATS but it can be controlled by

increasing the difference in the quality factors of the two orthogonally polarized TE and TM modes in the case of CPIT, especially when working with the hollow bottle resonator.

A larger pulse delay (τ_d ~210 ns) can be produced with a single high quality factor and strongly overcoupled mode (Q = 1×10^8, M = 0.05) and a larger pulse advancement (τ_d = -40 ns) can be produced with a single high quality factor and undercoupled mode (Q = 1×10^8, M = 0.75) when working with a 175-μm-radius hollow bottle resonator since the single mode can produce the larger dispersion (proved by the numerical model), but for that kind of experiment the throughput spectrum does not have the frequency filtering effect (high and low levels of the throughput power between on and off resonance) as in the case of CMIT/ATS or CPIT for optical switching applications.

In order to determine the true value of cross polarization coupling strength T_s, we have to do the computer model fitting for the throughput power spectrum. The offset and pulse detuning are known approximately from the experimental results, and they are refined by the fitting process. After getting a good fit, the values of T_s, offset, and pulse detuning are determined from the computer model. In this work, scattering and rotational models have been used alternatively to fit the data. These two models are equivalent for most of the experiment-fitting, except for the case of CPIT with nonzero T_s, due to the difference in the intracavity fields of the two models. Since the throughput optical pulses are noisy, we have to do a Gaussian fit for both off resonant and resonant throughput optical Gaussian pulses so as to measure the pulse width and delay/advancement exactly. The width of the input pulse in the model has been chosen to be equal to FWHM of the

off resonant throughput optical Gaussian pulse. By comparing the relative positions of the optical resonant Gaussian pulse with respect to the optical off resonant Gaussian pulse, the delay or advancement time is determined. Below is a table summarizing the results for most of our experiments with both microsphere and hollow bottle resonator. The scattering model is a default, unless otherwise noted.

Table 1. Summary of the experiment/model pulse delay agreement

Figure	Effect	Resonator	Expt. delay (ns ± 5 ns)	Model delay (ns)	T_s (± 25%)
48	CMIT	Microsphere	8	10	2.82×10^{-8}
49	ATS	Microsphere	32	13	1.4×10^{-8}
50	CMIA	Microsphere	-9	-25[b]	5×10^{-8}
51	CMIA	Microsphere	27[a]	60	2×10^{-8}
63	CMIT	HBR	42	40	2.24×10^{-8}
64	CMIT	HBR	50	25	1.51×10^{-8}
65	ATS	HBR	22	10	3.55×10^{-9}
66	CMIA	HBR	-13	-12	3.98×10^{-10}
67	CMIA	HBR	-11	-20	7.94×10^{-10}
68	CMIA	HBR	73	80	7.94×10^{-11}
69	CMIA	HBR	170	140	10^{-10}
71	CPIT	Microsphere	27[a]	80	2×10^{-8}
72	CPIA	Microsphere	-13	-30	0
73	CPIA	Microsphere	30	20[c]	0
74	CPIT	HBR	47[a]	150	0
75	CPIA	HBR	-17	-25	0
76	CPIA	HBR	16[a]	160	0
77	CPIA	HBR	27[a]	70[c]	0
79	CPIT	Microsphere	24[a]	150[c]	0
80	CPIT	Microsphere	24[a]	150[d]	0
81	CPIT	HBR	24[a]	80	10^{-8}
82	CPIT	HBR	24[a]	120[c]	0
83	CPIT	HBR	24[a]	130[d]	0
84	CPIA	HBR	12	15[b,c]	1.6×10^{-8}
85	CPIA	HBR	12	15[d]	1.6×10^{-8}
86	CPIA	HBR	12	0	2.5×10^{-7}

[a] Mode overlap affects off-resonant pulse.

[b] Nonzero T_s; rotational model.

[c] Rotational model.

[d] Rotational model, reverse order.

From Table 1 we realize that the major limitation of our experiments is not getting the off- resonant pulse truly off resonance because of mode overlap. This leads to the disagreement between the experimental pulse delay/advancement and model calculation, in addition to distorting the throughput spectrum. For future work, we are trying to get a cleaner throughput spectrum for CMIT/ATS/CMIA and CPIT/CPIA by using the smaller diameter capillary, and to do more experiments with CMIA/ATS in order to produce fast light at the critical point for the switching from CMIA to ATS. This effect helps to increase the separation between resonant frequencies for the clockwise and counterclockwise propagating light when a resonator based optical gyroscope is rotating. Moreover, CMIT/CPIT can be used for chemical sensing, e.g., when the resonator is put in contact with surrounding media with different analyte concentrations, the two WGMs will be frequency-shifted by different amounts from their equilibrium positions. By measuring the output intensity of the throughput spectrum at a fixed wavelength (normally the resonant wavelength for IT when the resonator is not in contact with the surrounding medium) and noting its variation under different conditions, the change in output intensity can be determined. That change can help us to determine the concentration of the analyte in the solution with high accuracy. In the near future, in our lab, we will try to produce stopped light [51] by using the coupled resonator method in which the separation between the resonators is controlled by a precise actuator and the pulse response is observed, and also consider developing research toward observing negative group velocity [52,53] by using a series of resonators in which each of them can produce the pulse advancement.

In general, this dissertation has brought to us fundamental concepts of EIT/ATS and EIA, two new methods to produce the EIT/ATS-like and EIA-like features of the throughput power enabling slow and fast light; CMIT/ATS/CMIA and CPIT/CPIA for both microsphere and hollow bottle resonator, and two scattering and rotational computer models used to fit the experimental data for both throughput power and the pulses. Although the experimental data still have some disagreement with the model calculation, the fitting was performed pretty well for both throughput spectrum and the pulses. The fitting helps us to determine the cross polarization coupling strength T_s, off resonant throughput pulse width and pulse delay/advancement directly from the model, and from that point we have the new methods to improve the quality of the experimental data and come up with the new research ideas.

REFERENCES

[1] R. W. Boyd, "TOPICAL REVIEW Slow and fast light: fundamentals and applications," J. Mod. Opt. **56**, 1908-1915 (2009).

[2] M. S. Shahriar, G. S. Pati, R. Tripathi, V. Gopal, M. Messall, and K. Salit, "Ultrahigh enhancement in absolute and relative rotationa sensing using fast and slow light," Phys. Rev. A **75**, 053807 (2007).

[3] D. D. Smith, H Chang, K. Myneni, and A. T. Rosenberger, "Fast light enhancement of an optical cavity by polarization mode coupling," Phys. Rev. A **89**, 053804 (2014).

[4] C. Y. Chao, and L. J. Guo, "Biochemical sensors based on polymer microrings with sharp asymmetrical resonance," Appl. Phys. Lett. **30**, 1527-1529 (2003).

[5] X. Zhou, L. Zhang, A. M. Armani, J. Liu, X. Duan, D. Zhang, H. Zhang, and W. Pang, "An Integrated Photonic Gas Sensor Enhanced by Optimized Fano Effects in Coupled Microring Resonators With an Athermal Waveguide," J. Lightwave Technol. **33**, 4521-4530 (2015).

[6] M. Li, X. Wu, L. Liu, X. Fan, and L. Xu, "Self-Referencing Optofluidic Ring Resonator Sensor for Highly Sensitive Biomolecular Detection," Anal. Chem, **85**, 9328-9332 (2013).

[7] S. Fan, "Sharp asymmetric line shapes in side-coupled waveguide-cavity systems," Appl. Phys. Lett. **80**, 908-910 (2002).

[8] S. F. Mingaleev, A. E. Miroshnichenko, and Y. S. Kivshar, "Coupled-resonator-induced reflection in photonic-crystal waveguide structures," Opt. Express **16**, 11647-11657 (2008).

[9] L. Y. Mario, S. Darmawan, and M. K. Chin, "Asymmetric Fano resonance and bistability for high extinction ratio, large modulation depth, and low power switching," Opt. Express **14**, 12770-12781 (2006).

[10] A. T. Rosenberger, "EIT analogs using orthogonally polarized modes of a single whispering-gallery microresonator," in *Advances in Slow and Fast Light VI,* S. Shahriar and F. A. Narducci, eds., Proc. SPIE **8636**, 863602 (2013).

[11] M. Fleischhauer, A. Imamoglu, and J. P. Marangos, "Electromagnetically induced transparency: Optics in Coherent Media," Rev. Mod. Phys. **77**, 633-673 (2005).

[12] A. Lezama, S. Barreiro, and A. M. Akulshin, "Electromagnetically induced absorption," Phys. Rev. A **59**, 4732-4735 (1999).

[13] D. D. Smith, H. Chang, K. A. Fuller, A. T. Rosenberger, and R. W. Boyd, "Coupled resonator induced transparency," Phys. Rev. A **69**, 063804 (2004).

[14] A. Naweed, G. Farca, S. I. Shopova, and A. T. Rosenberger, "Induced transparency and absorption in coupled whispering-gallery microresonators," Phys. Rev. A **71**, 043804 (2005).

[15] E. B. Dale, *Coupling Effects in Dielectric Microcavities*, PhD dissertation, Oklahoma State University, 2010.

[16] B. Peng, S. K. Ozdemir, W. Chen, F. Nori, and L. Yang, "What is and what is not electromagnetically induced transparency in whispering-gallery microcavities," Nat. Commun. **5**, 1-9 (2014).

[17] T. Oishi, R. Suzuki, A. I. Talukder, and M. Tomita, "Transition from an optical precursor in coupled-resonator-induced transparency to coherent energy exchange in Autler-Townes splitting," Phys. Rev. A **88**, 023847 (2013).

[18] R. W. Boyd, *Nonlinear Optics* (AP, New York, 2008), pp.185-192.

[19] C. Goren, A. D. Wilson-Gordon, M. Rosenbluh, and H. Friedmann, "Electromagnetically induced transparency due to transfer of coherence and to transfer of population," Phys. Rev. A **67**, 033807 (2003).

[20] C. Goren, A. D. Wilson-Gordon, M. Rosenbluh, and H. Friedmann, "Electromagnetically induced absorption due to transfer of population in degenerate two-level systems," Phys. Rev. A **70**, 043814 (2004).

[21] A. M. Akulshin, S. Barreiro, and A. Lezama, "Electromagnetically induced absorption and transparency due to resonant two-field excitation of quasidegenerate levels in Rb vapor," Phys. Rev. A **57**, 2996-3002 (1998).

[22] Y. Q. Li, S. Z. Jin, and M. Xiao, "Observation of an electromagnetically induced change of absorption in multilevel rubidium atoms," Phys. Rev. A **51**, R1754-R1757 (1995).

[23] P. Tassin, L. Zhang, R. Zhao, A. Jain, T. Koschny, and C. M. Soukoulis, "Electromagnetically induced Transparency and Absorption in Metamaterials: The Radiating Two-Oscillator Model and Its Experimental Confirmation," Phys. Rev. Lett. **109**, 187401 (2012).

[24] C. L. Garrido Alzar, M. A. G. Martinez, "Classical analog of electromagnetically induced transparency," Am. J. Phys. **70**, 37-41 (2002).

[25] X. Yang, M. Yu, D. L. Kwong, and C. W. Wong, "All-Optical Analog to Electromagnetically Induced Transparency in Multiple Coupled Photonic Crystal Cavities," Phys. Rev. Lett. **102**, 173902 (2009).

[26] Q. Xu, S. Sandhu, M. L. Povinelli, J. Shakya, and S. Fan, "Experimental Realization of an On-Chip All-Optical Analogue to Electromagnetically Induced Transparency," Phys. Rev. Lett. **96**, 123901 (2006).

[27] L. Maleki, A. B. Matsko, A. A. Savchenkov, and V. S. Ilchenko, "Tunable delay line with interacting whispering-gallery-mode resonators," Opt. Lett. **29**, 626-628 (2004).

[28] J. P. Rezac, *Properties and Applications of Whispering Gallery Mode Resonances in Fused Silica Microspheres*, PhD dissertation, Oklahoma State University, 2002.

[29] R.-I. Stoian, *Developments in Near Infrared Lasing and Chemical Sensing Using Novel Photonic Structures*, PhD dissertation, Oklahoma State University, 2013.

[30] Y. F. Xiao, L. He, J. Zhu, and L. Yang, "Electromagnetically induced transparency-like effect in a single polydimethylsiloxane-coated silica microtoroid," Appl. Phys. Lett. **94**, 231115 (2009).

[31] B. B. Li, Y. F. Xiao, C. L. Zou, Y. C. Liu, X. F. Jiang, Y. L. Chen, Y. Li, and Q. Gong, "Experimental observation of Fano resonance in a single whispering-gallery microresonator," Appl. Phys. Lett. **98**, 021116 (2011).

[32] C. H. Dong, C.-L. Zou, Y.-F. Xiao, J.-M. Cui, Z.-F. Han, and G.-C. Guo, "Modified transmission spectrum induced by two-mode interference in a single silica microsphere," J. Phys. B: At. Mol. Opt. Phys. **42**, 215401 (2009).

[33] Q. Huang, Z. Shu, G. Song, J. Chen, J. Xia, and J. Yu, "Electromagnetically induced transparency-like effect in a two-bus waveguides coupled microdisk resonator," Opt. Express **22**, 3219-3227 (2014).

[34] T. J. Kippenberg, S. M. Spillane, and K. J. Vahala, "Modal coupling in traveling-wave resonators," Opt. Lett. **27**, 1669-1671 (2002).

[35] Y. Yang, S. Saurabh, J. Ward, and S. Nic Chormaic, "Coupled-mode-induced transparency in aerostatically tuned microbubble whispering-gallery resonators," Opt. Lett. **40**, 1834-1837 (2015).

[36] S. Ramelow, A. Farsi, S. Clemmen, J. S. Levy, A. R. Johnson, Y. Okawachi, M. R. E. Lamont, M. Lipson, and A. L. Gaeta, "Strong polarization mode coupling in microresonators," Opt. Lett. **39**, 5134-5137 (2014).

[37] J. P. Rezac and A. T. Rosenberger, "Locking a microsphere whispering- gallery mode to a laser," Opt. Express **8**, 605-610 (2001).

[38] E. K. Gonzales, *An Investigation of Intermodal Coupling Effects in Optical Microresonators*, MS thesis, Oklahoma State University, 2011.

[39] K. Bui, E. Gonzales, and A. T. Rosenberger, "Modeling Cross Polarization Coupling in a Whispering-Gallery-Mode Microresonator": *23rd Annual Research Symposium*, Oklahoma State University, Stillwater, OK, 2012.

[40] A. T. Rosenberger, "Comparison of methods for achieving induced transparency or absorption with pulse delay or advancement in a single microresonator," in *Slow Light, Fast Light, and Opto-Atomic Precision Metrology IX***,** S. M. Shahriar and J. Scheuer, eds., Proc. SPIE **9763**, 97631E (2016).

[41] L. Y. Mario, M. K. Chin, "Optical buffer with higher delay-bandwidth product in a two-ring system," Opt. Express **16**, 1796-1807 (2008).

[42] K. V. Bui and A. T. Rosenberger, "Experimental study of induced transparency or absorption and slow or fast light using orthogonally polarized whispering-gallery modes of a single microresonator," in *Slow Light, Fast Light, and Opto-Atomic Precision Metrology IX,* S. M. Shahriar and J. Scheuer, eds., Proc. SPIE **9763**, 97630W (2016).

[43] G. S. Murugan, M. N. Petrovich, Y. Jung, J. S. Wilkinson, and M. N. Zervas, "Hollow-bottle optical microresonators," Opt. Express **19**, 20773-20784 (2011).

[44] O. Kocharovskaya and Ya. I. Khanin, "Population trapping and coherent bleaching of a three-level medium by a periodic train of ultrashort pulses," Sov. Phys. JETP **63**, 945-950 (1986).

[45] L. He, Y.-F. Xiao, J. Zhu, S. K. Ozdemir, and L. Yang, "Oscillatory thermal dynamics in high-*Q* PDMS-coated silica toroidal microresonators," Opt. Express **17**, 9571-9581 (2009).

[46] Q. Li, T. Wang, Y. Su, M. Yan, and M. Qiu, "Coupled mode theory analysis of mode-splitting in coupled cavity system," Opt. Express **18**, 8367-8382 (2010).

[47] M. Galli, S. L. Portalupi, M. Belotti, L. C. Andreani, L. O'Faolain, and T. F. Krauss, "Light scattering and Fano resonances in high-*Q* photonic crystal nanocavities," Appl. Phys. Lett. **94**, 071101 (2009).

[48] P. Tassin, L. Zhang, T. Koschny, E. N. Economou, and C. M. Soukoulis, "Planar designs for electromagnetically induced transparency in metamaterials," Opt. Express **17**, 5595-5605 (2009).

[49] L. V. Hau, S. E. Harris, Z. Dutton, and C. H. Behroozi, "Light speed reduction to 17 metres per second in an ultracold atomic gas," Nature **397**, 594-598 (1999).

[50] Y. Wang, K. Zhang, S. Zhou, Y.-H. Wu, M.-B. Chi, and P. Hao, "Coupled-mode induced transparency in a bottle whispering-gallery-mode resonator," Opt. Lett. **41**, 1825-1828 (2016).

[51] A. A. Savchenkov, A. B. Matsko, V. S. Ilchenko, D. Strekalov, and L. Maleki, "Direct observation of stopped light in whispering-gallery-mode microresonator," Phys. Rev. A **76**, 023816 (2007).

[52] W. G. A. Brown, R. Mc Lean, A. Sidorov, P. Hannaford, and A. Akulshin, "Anomalous dispersion and negative group velocity in a coherence-free cold atomic medium," J. Opt. Soc. Am. B **25**, C82-C86 (2008).

[53] U. Vogl, R. T. Glasser, and P. D. Lett, "Advanced detection of information in optical pulses with negative group velocity," Phys. Rev. A **86**, 031806(R) (2012).

VITA

Khoa Viet Bui

Candidate for the Degree of

Doctor of Philosophy

Thesis: INDUCED TRANSPARENCY AND PULSE DELAY PLUS INDUCED ABSORPTION AND PULSE ADVANCEMENT USING THE ORTHOGONALLY POLARIZED WHISPERING GALLERY MODES OF A SINGLE MICRORESONATOR

Major Field: Photonics

Biographical:

Personal Data: Born in Yen Bai, Vietnam on 16 January 1981.

Education:

Completed the requirements for the Doctor of Philosophy in Photonics at Oklahoma State University, Stillwater, Oklahoma in July, 2016.

Completed the requirements for the Bachelor of Science in Engineering Physics at Hanoi University of Science and Technology, Hanoi, Vietnam in 2003.

Experience:
Production of silica microspheres, hollow bottle resonators, evanescent wave.
Coupled mode induced transparency and absorption.
Coresonant polarization induced transparency and absorption.
Pulse delay and pulse advancement.